Time-ordered modelling of Zodiacal Emission in BeyondPlanck

Metin San

Thesis submitted for the degree of
Master of Science in Astronomy

Institute of Theoretical Astrophysics
University of Oslo

14th June 2020

Abstract

Precise modelling of foreground emission is crucial to extract the Cosmic microwave background (CMB) signal. Recent developments in the hunt for primordial B-modes in the polarized CMB favor component separation to be done directly in the time-ordered domain to minimize foreground contamination and systematic effects. This would require all aspects of component separation to become more efficient due to an unavoidable increase in data volume.

In this thesis, we implement an efficient and accurate method of performing Zodiacal corrections to high-frequency cosmological data, directly in the time-ordered domain. We adopt the Kelsall et al. (1998) interplanetary dust (IPD) model consisting of six Zodiacal components - a Diffuse Cloud, three Dust Bands, a Circumsolar Ring, and the Earth-trailing Feature. We compute the Zodiacal emission by integrating the dust density along a line-of-sight from an observer to 5.2 AU, pixel-by-pixel at the time of observation, similar to the approach used by the *Planck* collaboration.

Our model is tested using the BeyondPlanck LFI data processing pipeline from which we have obtained maps that accurately reproduce the Zodiacal emission templates used during the *Planck* Zodiacal corrections. The results obtained by our model suggests that the Zodiacal emission is slightly weaker than previously estimated by *Planck*, most notably for the Diffuse Cloud, which is found to differ by $\sim 8\%$ in overall signal amplitude, although further investigation is needed to fully understand the extent of this result along with a new fit of the Zodiacal emissivities. As a possible step towards a more precise IPD model, we test the significance of dust enhancements to the Circumsolar Ring at the Sun-Earth Lagrange points L4 and L5. We find that enhancements at the order of the Earth-trailing Feature show no significant increase to the overall signal. Future work to make the method more efficient and possible improvements to the K98 IPD model are also described here.

Acknowledgments

I would like to thank my brilliant supervisors Ingunn Wehus and Hans Kristian Eriksen, for taking me on as their student and welcoming me with open arms to the CMB group where I have been most fortunate to work with many great scientists. A special thanks to my co-supervisors Daniel Herman and Mathew Galloway, who gave unsparingly of their time and energy during this last year. Your careful supervision has significantly improved the quality of my studies. I would also like to thank my fellow Master's students for the many social activities, late-night work sessions, and chess matches that have taken place over these last years. A special thanks to Torbjørn Østmoe, who has been one of my closest friends throughout my studies. This journey would not have been the same without you. And lastly, I would like to thank my family and my loving girlfriend Ylva, for the support they have so generously given me throughout my scientific endeavors.

Metin San

Preamble

The *Planck* satellite was launched in 2009 and observed the sky in a wide range of frequencies over four years. The data obtained by the satellite has provided a wealth of results for the field of observational cosmology. *Planck* has allowed us to map the Cosmic Microwave Background (CMB) to the highest precision to date. Additionally, *Planck* has given us refined measurements of the age of the Universe, the rate at which it expands, and many other notable cosmological properties.

The next frontier in the field is the search for inflationary gravitational waves. According to theory, these waves should be detectable in perturbations of the CMB polarization field. However, the signal produced by the gravitational waves is expected to be minuscule, and measuring this with current CMB polarization data is unlikely. This is because the *Planck* data consists of more than just pure CMB signal. The sky is filled with radiation from various astrophysical sources referred to as foregrounds, which obscure our view of the CMB. To produce "clean" maps of the CMB, these foregrounds need to be accurately disentangled from the CMB signal in a process called component separation.

One of the most important challenges faced by the component separation community in current times regarding existing and future CMB data and the detection of the primordial gravitational waves is the instrumental systematics induced by the foregrounds. The BeyondPlanck collaboration, which is a successor of *Planck*, has proposed a solution to this problem that will allow for joint estimation of cosmological parameters, foreground components, and instrumental specifications. The critical step in their solution is to apply component separation to raw time-ordered observations as opposed to analysing pre-processed frequency maps. This will effectively close the loop between instrumental systematics, astrophysical component separation, and cosmological interpretation. The drawback of the transition to the time-ordered domain is that the data volume considered during the analysis becomes significantly larger, which seems to be a necessity if we are ever to discover the weak signal of the gravitational waves.

The objective of the BeyondPlanck collaboration requires their component separation software to be highly self-sufficient if it is to produce complete cosmological products from raw time-ordered data. This introduces the need for a module in the software which estimates the *Zodiacal Light Emission* (ZLE) as observed over the course of an observational survey. ZLE is the result of thermal radiation from dust grains distributed around the Solar System and contributes to a significant amount of the total sky brightness at the higher *Planck* frequencies. The Zodiacal Emission module will have to be able to accurately and efficiently estimate the ZLE captured in any time-ordered data set at the time of observation.

In this thesis, we investigate the Zodiacal correction methods used by the *Planck* and COBE/DIRBE collaborations and apply these to build and implement a Zodiacal Emission module to be used for current and future high-frequency CMB analysis. Integrating such a model to an end-to-end analysis framework will ensure pixel-accurate estimations only limited by the quality of the ZLE model, and will allow us to constrain any systematic problems related to the Zodiacal corrections.

In the first part of this thesis, we introduce the reader to the field of observational cosmology, focusing on the events leading to the discovery of the CMB. What follows is an introduction to the Zodiacal Light, both as a historical phenomenon and an important foreground to high-frequency CMB analysis. Other relevant foregrounds in the context of CMB analysis are presented in a chapter concerning the microwave sky. The second part of our thesis addresses the various methods employed in the BeyondPlanck framework to analyse and process cosmological data, with a particular focus on the aspect of interplanetary dust modelling and ZLE. In the last part of this thesis, we present our results obtained by applying the Zodiacal Emission module to the early BeyondPlanck LFI data set. Finally, we conclude our studies by outlining our main results and make recommendations for further research.

Contents

List of Figures

Abbreviations and Acronyms

CIB Cosmic Infrared Background. 6

CMB Cosmic Microwave Background. 5

COBE Cosmic Background Explorer. 6

DIRBE Diffuse Infrared Background Experiment. 6

IPD Interplanetary Dust. 13

SED Spectral Energy Density. 21

WMAP Wilkinson Microwave Anisotropy Probe. 7

ZL Zodiacal Light. 13

ZLE Zodiacal Light Emission. 16

Part I

Introduction

Chapter 1

A History of Cosmology

Humanity's understanding of the Universe is something that has evolved significantly over time. At the time of classical Greek astronomy, it was believed that the Earth was fixed at the center of the Universe and that the Sun, Moon, planets, and stars all orbited the Earth. This view, known as the geocentric system, was a model for the whole Universe because at this time the known universe consisted only of what was visible to the naked eye.

It was not until nearly two millennia later during the Copernican Revolution where the heliocentric system, a model where the Earth and the other planets all revolve around the Sun, would come to replace the geocentric description of the Universe. This new worldview was further strengthened with Newton's laws of motion and gravity [1], and Galileo's discovery of Jupiter's moons [2]. The transition from geocentrism to heliocentrism is one of many changes our cosmological model for the Universe has undergone.

Astronomers eventually came to understand that our Solar System is merely a substructure of something larger, namely the Milky Way, our galaxy. Our model of the Universe had to be extended to include countless of new star systems. In 1924, the famous astronomer Edwin Hubble estimated the distance to the Andromeda nebula [3]. His findings suggested that the nebula was external to the Milky way, which indicated the existence of other galaxies. Five years later, in 1929, Hubble showed that other galaxies were moving away from us with velocities proportional to their distance [4]. This result had a revolutionary explanation; the Universe was expanding.

This historical and somewhat philosophical introduction serves as a reminder that cosmology, the study of the origins and the evolution of the Universe has for a long time been in a state of constant change. Today we believe that the expansion of the Universe started about 14 billion years ago. We have models that describe its dynamics and evolution, and we are able to predict and explain a large range of physical phenomena to high precision. The coming sections aim to give a brief historical introduction to modern cosmology with a focus on the detection of the Cosmic Microwave Background and its importance to current cosmological models.

1.1 The cosmic egg

Despite the rate with which our cosmological models have evolved over the centuries, there is one specific addition which is often considered the roots of all modern cosmology: the theory of General Relativity (GR) developed by Albert Einstein in 1915 [5]. With the introduction of GR came the concept of spacetime; a way of parametrizing space and time. Gravity which had previously been thought of as a classical force was now described as a distortion to spacetime in the presence of matter or energy. GR was quickly solidified as a theory through experiments. From here on, new theorized universe models were based on finding solutions to Einstein's equations which satisfied GR. Many of these solutions were presented over the years, each describing a unique universe. In 1922, Alexander Friedmann, a Russian cosmologist, and mathematician discovered a set of solutions describing an isotropic, homogeneous, non-static, and expanding universe [6]. However, the consensus in the scientific community at this time was that the Universe had to be static. Accordingly, Einstein himself, along with the rest of the scientific community was initially skeptical of the idea of an expanding universe.

Five years later, in 1927, the Belgian cosmologist and priest Georges Lemaître independently discovered the same solution Friedmann had five years earlier. He suggested that the recently observed redshift of galaxies could be attributed to an expanding universe; a rather bold statement that would be proved by Hubble only two years later [4]. In 1931, Lemaître argued brilliantly that if matter everywhere was receding, at some point in time, the Universe must have been in an extremely compact and dense state. He called this hypothesis for the primeval atom or the cosmic egg. His proposal was initially met with skepticism from Einstein as he felt the hypothesis suggested the idea of creation. Ironically, Einstein would later come to say: "This is the most beautiful and satisfactory explanation of creation to which I have ever listened."[7], after listening to Lemaîtres lecture at California Institute of Technology about his theory in 1933.

Today the cosmic egg theory is more famously known as the Big Bang theory after a sarcastic remark from Fred Hoyle. Hoyle which at the time was an influential English astronomer would come to be one of the top personalities to support the rivaling steady-state universe model; a model proposed by H. Bondi and T. Gold in 1948 [8] which suggested that the matter density of the Universe remained constant despite its expansion through the continuous creation of new matter. This model didn't require the Universe to have a beginning nor an end; an idea which was repugnant to many at the time.

1.2 Discovering the background radiation

One of the early advocates of Lemaître's primeval atom theory was the Soviet-American physicist George Gamow. Gamow assumed that a universe in such a dense state would be radiation dominated. In 1949, Gamow, alongside his Ph.D. student Ralph Alpher and researcher Robert Herman, became the first astronomers to predict that there would be remnant left-over background radiation from this state, with energies corresponding to a temperature of ~ 5 K [9]. Observational radio astronomy had seen huge progress since World War II and was in the process of becoming its own field. Alpher and Herman wanted to perform radio experiments in hopes of detecting their predicted background radiation, but their proposals were denied as such a signal was believed by many to be too weak to measure with available technology at the time.

In the 1960s, the two astronomers, Arno Penzias, and Robert Wilson were working with a microwave horn antenna at Bell Laboratories, New Jersey. The telescope was originally intended to be used for radio astronomy and satellite communication, but when Penzias and Wilson first attempted to use it they discovered something unexpected. No matter where they pointed the telescope, an excess background signal was measured which they could not explain through systematic means. They scrubbed away all the pigeon droppings on the instrument and even wiped out the local pigeon population, but to no help; the background signal was still present. Penzias and Wilson had discovered what is today known as the Cosmic Microwave Background (CMB), one of the most important physical observable known to date.

Penzias was eventually informed of a pre-print by James Peebles on nucleosynthesis, in which a cosmic excess signal, matching the findings of Penzias and Wilson, was predicted. Penzias proceeded to share their observational findings with Robert Dicke, a colleague of Peebles at Princeton. Together, Dicke and Peebles visited Bell Laboratories to investigate the discovery. Shortly after the visit, Dicke and Peebles, along with P. G. Roll and D. T. Wilkinson published a paper titled "Cosmic Black-Body Radiation" [10] which not only connected the observed background signal to the theoretical predictions but also set some constraints on cosmological models based on their findings. The interpretation of the background radiation was a controversial topic in the 1960s as the radiation was neither predicted, nor accounted for, by the rivaling steady-state model. The discovery of the CMB turned out to be one of the most important discoveries in cosmology to date. Penzias and Wilson went on to win the Nobel prize in 1978 for the detection, and Peebles recently got his Nobel prize in 2019 for his work in the field.

1.3 The Cosmic Microwave Background

Astronomers quickly began studying the newly discovered radiation field in greater detail. One of the first tests was to see whether or not there was a *dipole* present in the background signal. A dipole is a form of anisotropy present the in observed signal where there is relative motion between the source and observer. Such a dipole was expected to be present in the background radiation due to the motion of Earth around the Milky Way. A dipole was eventually found, but with unexpected results; the dipole was not in the direction of the rotation of the galaxy, but rather in the direction of the constellation Leo [11]. This finding had remarkable implications; not only did our galaxy as a whole move in the direction of Leo but galaxies, in general, appeared to be gravitationally bound to one another.

The anisotropies exhibited by the field had strongly captured the interest of many cosmologists. If the background radiation truly was the remnants of an early radiation dominated universe, then it should contain information encoded in the anisotropies predictable by cosmological models. Peebles, along with Harrison, Yu, and Zel'dovich theorized that there must have existed inhomogeneities in the early universe which should not only be detectable in the CMB but also act as seeds for the large scale structures observed in the Universe today [12] [13]. However, the predicted anisotropies were too small to be detected in the CMB data available at the time. In order to obtain the resolution required to measure the anisotropies, one would have to get rid of the atmospheric contamination present in the data.

1.3.1 COBE

Following the discovery of the CMB, the National Aeronautics and Space Administration (NASA) decided that they would launch a satellite to further investigate the background radiation. They assembled a group of world-leading CMB experts, including famous names such as David Wilkinson and George Smoot. The group came to the decision that the satellite should consist of the following three instruments:

DIRBE The Diffuse Infrared Background Explorer, which would map the Cosmic Infrared Background (CIB), background radiation similar to the CMB believed to be the result of thermal dust emission from distant galaxies.

FIRAS The Far InfraRed Absolute Spectrometer built to precisely measure the CMB spectrum and to observe dust and line emission from the Milky Way.

DMR The Differential Microwave Radiometer designed to study the intrinsic anisotropies in the CMB.

The satellite was appropriately named Cosmic Background Explorer (COBE) as it was the first of its kind. When the mission launched in 1989 it had cost nearly 160 million dollars and had involved over a thousand people. The highly anticipated results were revealed a year later, in 1990. Through the FIRAS instrument, the team had found the most perfect black-body spectrum ever observed, with a temperature of $T_0 = 2.7255 \pm 0.0009$K. The observed spectrum can be seen in Figure 1.1.

The DMR instrument had scanned the full sky at 31.5, 53, and 90 GHz with an angular resolution of 7° which allowed researchers to study the intricacies of the anisotropies in the CMB power spectrum for the first time [14]. Additionally, the data collected by the DIRBE and FIRAS instruments were used to produce frequency maps of the sky, which highlighted the many *foregrounds* present in the data. Foregrounds are various physical phenomena within our galaxy which emit radiation over certain frequencies. They play an important role in CMB analysis where they act as contaminants to CMB data, obscuring our view of the background radiation. These maps would be used to clean the CMB data of foregrounds and was in many ways the introduction to the field of component separation.

The results from the COBE mission had solidified the Big Bang theory as the best cosmological model to date, and team members John C. Mather and George F. Smoot was awarded the Nobel prize based on the success of the mission. Despite the success

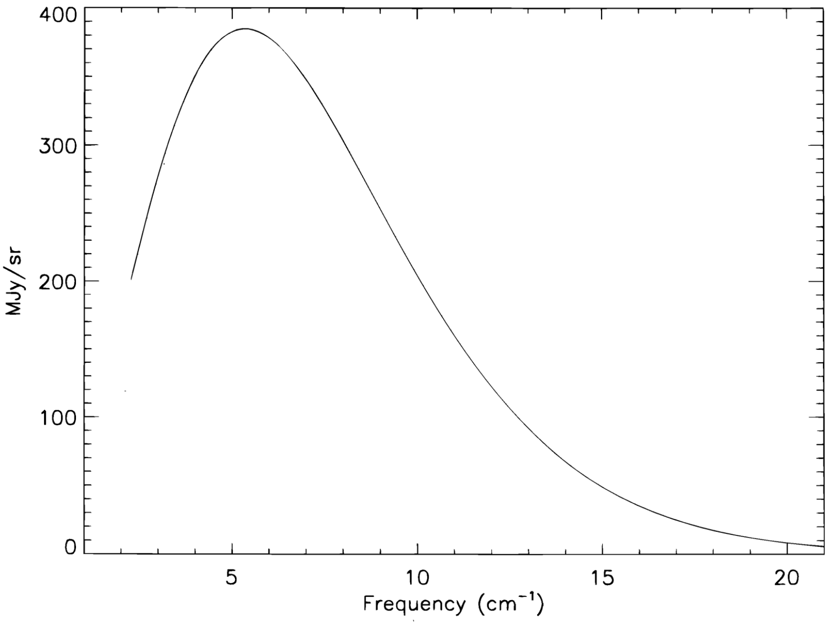

Figure 1.1: The observed FIRAS CMB spectrum. Uncertainties are smaller than the thickness of the line. Image taken from Fixen et al. 1996 [15]

of COBE, there were still plenty of unanswered questions surrounding the CMB which required measurements of the CMB anisotropies to a significantly higher resolution to be answered.

1.3.2 WMAP

In 2001, twelve years after the launch of the successful COBE mission, the next big CMB experiment began observing the sky; The Wilkinson Microwave Anisotropy Probe (WMAP). The satellite was proposed to NASA in 1995 to search the CMB for anisotropies at scales much smaller than 1°. WMAP would differ from COBE primarily in the two following ways: 1) WMAP would observe the sky over five frequency bands ranging from 23 to 94 GHz opposed COBE's three; and 2) WMAP would measure the difference in signal between two points on the sky through pairs of differential microwave radiometers, in contrast with COBE which measured sky signal from a zero-point.

The WMAP mission was stunningly successful, and its results are often said to have been the foundation of our current Standard Model of Cosmology. The team produced a detailed set of full-sky frequency maps and a new CMB power spectrum with an angular resolution of $l \sim 1200$. The combination of high-resolution frequency maps over a wider range of frequencies allowed WMAP to produce the first set of full-sky foreground component maps, which significantly improved the process of separating the CMB signal from the foregrounds. As such, the data provided by WMAP led to many new cosmological estimates, including amongst others: the age of the Universe estimated to be 13.74 billion years, and the Hubble constant (the parameter describing how fast the Universe is expanding at different distances from a particular point in space) estimated to 70km/s/Mpc. Additionally, the Universe was found to be composed of 72% energy density, 23% dark matter, and 4.6% baryonic matter [16].

1.3.3 *Planck*

The next big iteration of precision cosmology came in the form of the *Planck* satellite; a project by the European Space Agency (ESA). The satellite was appropriately named after the famous physicist Max Planck who was the first to explain the black-body spectrum. The main goal of *Planck* was to obtain definite measurements of the CMB temperature anisotropies with unprecedented resolution. The satellite was equipped with a broad array of highly sensitive detectors. These would observe the sky over a large range of frequencies (nine individual frequency bands compared to WMAPs five), with resolutions starting at 33 arc-minutes at 30 GHz, and going up to 5 arc-minutes at 857 GHz. The detectors were split over two instruments:

LFI The Low-Frequency-Instrument which would perform high-sensitivity measurements of the sky in the frequency range of 27 to 77 GHz, with band centers at 30, 44, and 70 GHz. The instrument consisted of 22 individual radio receivers.

HFI The High-Frequency-Instrument which would perform high-sensitivity measurements of the diffuse radiation contaminating the sky. The instrument consisted of 52 bolometric detectors which operated in a broad frequency range of 84 GHz to 1 THz, with band centers at 100, 143, 217, 353, 545, and 857 GHz.

Unlike previous space-based CMB missions, *Planck*'s instruments were able to measure both the intensity and the polarization of the observed signal. Polarization describes the orientation of the photons perpendicular to the direction of propagation. Polarization measurements would allow researchers to investigate the CMB for traces of *gravitational waves* (distortions of spacetime moving at the speed of light). These waves are predicted to have propagated through the Universe during *inflation*, a brief period during the earliest stages of the Universe ($t \approx 10^{-35}$s) where space expanded exponentially.

Planck operated from 2009 until 2013 during which it produced five sets of full-sky maps with the highest resolution to date. The differences in resolution between the three generations of space-based CMB missions are illustrated in Figure 1.2. The data obtained by *Planck* has resulted in exceptionally tight constraints to the CMB temperature anisotropies and cosmological parameters. A comparison between the best-fit parameters from WMAP and *Planck* can be seen in table 1.1. Accordingly, *Planck* will most likely remain the backbone of CMB temperature research for the foreseeable future.

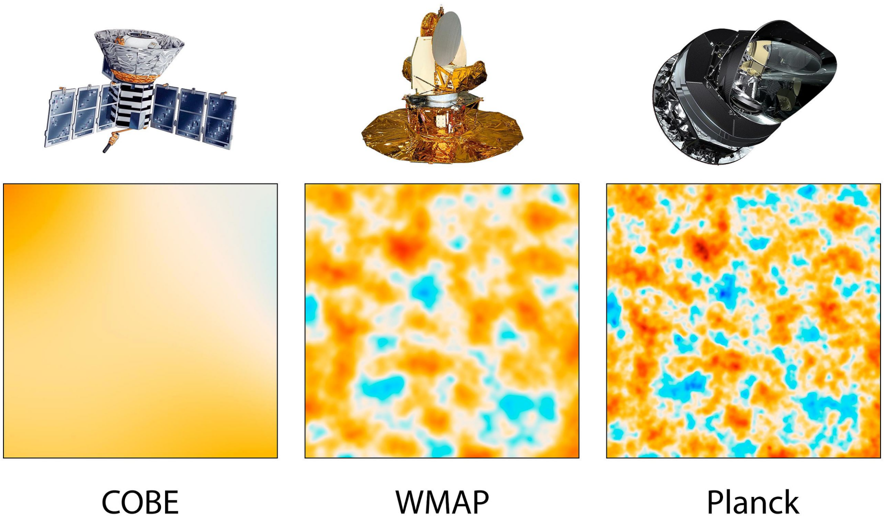

Figure 1.2: Resolution comparison of the three space-based CMB missions. Image credit NASA/JPL-Caltech/ESA [17]

1.4 The future of CMB research

Our understanding of the Universe has vastly improved following the COBE, WMAP, and *Planck* missions. Nevertheless, the information contained in the CMB is nowhere close to being exhausted. Obtaining more accurate constraints on the cosmological parameters are still crucial to fields such as theoretical physics. Although, our current precision of the CMB temperature anisotropies leaves little room for new fundamental discoveries. The statistical parameters of the background field are at this point unaffected by increases to resolution in temperature measurements. The initially exciting topic of temperature fluctuations is therefore today mostly about achieving more precise measurements in general, rather than discovery.

This has resulted in a recent shift in CMB research to another aspect of the microwave relic. We have briefly mentioned inflation during our introduction to *Planck*, as an epoch in time in which space expanded exponentially. This period in the early Universe is theorized to have existed as it explains some of the perplexing features of the Big Bang model, such as the *Horizon problem* in which two causally disconnected parts of the Universe exhibits homogeneity. If inflation occurred, it would have caused gravitational waves to propagate through the Universe, leaving imprints in the CMB detectable through the polarization of CMB photons. Such a detection would solidify cosmic inflation as a theory, and most certainly result in a Nobel prize.

Table 1.1: The derived cosmological parameters from the WMAP nine-year analysis [16] and *Planck* 2015 results [18].

Parameter	Description	WMAP value	*Planck* value
t_0	Age of the Universe [Gyr]	13.74 ± 0.11	13.799 ± 0.021
H_0	Hubble's constant [km\s\Mpc]	70.0 ± 2.2	67.74 ± 0.46
Ω_b	Baryon density	0.0463 ± 0.0024	0.0486 ± 0.0010
Ω_c	Cold dark matter density	0.233 ± 0.023	0.2589 ± 0.0057
Ω_Λ	Dark energy	0.721 ± 0.025	0.6911 ± 0.0062
n_s	Scalar Spectral index	0.972 ± 0.013	0.9667 ± 0.0040
τ	Reionization optical depth	0.089 ± 0.014	0.066 ± 0.012

1.4.1 The hunt for gravitational waves

CMB polarization is divided into two groups: E- and B-mode polarization. The two types of polarization leave distinct patterns on the CMB, as illustrated in Figure 1.3 (right). Inflationary gravitational waves are expected to produce both E- and B-mode polarization imprints on the CMB. Currently, no other sources are known to produce large-scale B-mode polarization in the CMB.

In 2014, the BICEP2 collaboration (Background Imaging of Cosmic Extragalactic Polarization 2) claimed that they had detected true B-modes in the CMB [19]. BICEP2 is a ground-based telescope, located at the South Pole. The telescope's main mission was to capture the aftershocks of cosmic inflation through their highly polarization-sensitive detectors. The swirly B-mode signal observed by BICEP2 is shown in Figure 1.3 (left). Naturally, the announcement caused an uproar in the community as cosmologists questioned the credibility of the discovery. The *Planck* collaboration, who at the time was seen as the competitors of BICEP2 was especially suspicious of their findings. It was true that BICEP2 had much more sensitive polarization data than what *Planck* had, but they were only observing at two frequency channels. *Planck*'s data was broader as it covered the same patch of the sky which BICEP2 had studied, over a wider range of frequencies. This frequency coverage turned out to be critical, as the *Planck* team later produced a map of the Milky Way's dust polarization which perfectly matched the pattern seen in the BICEP2 results. The B-mode pattern observed by BICEP2 was merely the result of improper foreground modelling.

Precise foreground modelling through component separation plays a significant role in our future understanding of the Universe, but ultimately, the field of cosmology is dependant on the acquisition of new and improved polarization data. Fortunately, there are several promising missions scheduled for the coming years that promises to provide us with just that.

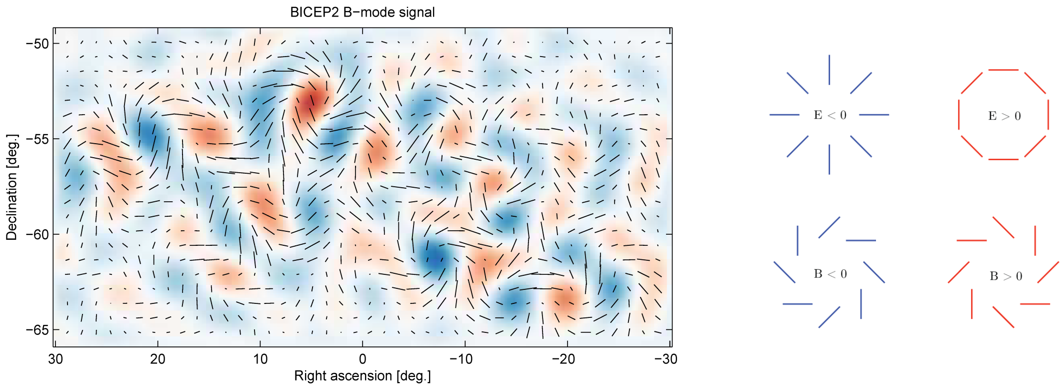

Figure 1.3: The B-mode pattern observed by BICEP2 [19] (left), and an illustration of the E and B-mode patterns [20] (right).

The Light satellite for the studies of B-mode polarization and Inflation from cosmic background Radiation Detection, or LiteBIRD, is the newest addition to the array of space-based CMB missions. LiteBIRD will attempt to measure the CMB polarization over the entire sky to an unprecedented resolution, which will allow researchers to test several inflationary models experimentally [21]. The current satellite design considers an array of over 2600 superconducting polarimetric detectors, with a focal plane cooled to a temperature of 100 mK. The mission is expected to launch in the middle of the 2020s.

The CMB-S4 mission is referred to as the next generation (Stage-4) ground-based CMB experiment [22]. The mission will consist of several telescopes equipped with highly sensitive superconducting detectors, spread out over locations including the South Pole, and the high Chilean Atacama plateau. The project aims to be the definite ground-based CMB project and will deliver highly constraining sets of data, to which any inflationary model must be consistent.

1.4.2 BeyondPlanck and component separation in the time-ordered domain

Improving the sensitivity of experiments alone will not be sufficient to make a robust detection of the elusive gravitational waves. That much is clear after the attempts of ultra-sensitive experiments, such as BICEP2 and *Planck*. At some point, CMB measurements become so precise that the majority of the uncertainties in the data results from instrumental characteristics. Foreground contamination, in combination with second-order interactions between the contamination and the instrument characterization, results in highly complicated non-linear problems. An example of such an issue is the problems encountered during gain estimation. Gain is the conversion factor between raw detector measurements and the actual sky signal amplitude. To properly estimate the instrumental gain in the presence of foregrounds requires a perfect sky model, but such a model can only be achieved through perfect gain estimates.

Cosmologists all over the world are currently working in a multitude of collaborations on this very matter. One such collaboration is BeyondPlanck, which has proposed a unique solution to these problems. BeyondPlanck is an international collaboration consisting of cosmologists and software engineers from the University of Oslo, University of Milano, INAF (Istituto Nazionale di Astrofisica), University of Helsinki, and Planetek Hellas. The collaboration builds directly on the experience gained from the *Planck* mission and aims to apply the same methodology using during the *Planck* analysis to both present, and future data sets. The main goal of the BeyondPlanck mission is best summarized in the following formulation, taken from BeyondPlanck Collaboration I (2020) [23]:

> "BeyondPlanck *aims to implement and apply a single statistically coherent analysis pipeline to Planck and other CMB data sets, processing raw uncalibrated time-ordered data into final astrophysical component maps, angular power spectra, and cosmological parameters within one single code, without the need for intermediate human intervention."*

BeyondPlanck's framework will be applied to raw time-ordered data observed directly by instruments, as opposed to pre-processed frequency maps and data sets. This will result in an end-to-end analysis where uncertainties can reliably be propagated to the final results, with minimal systematic errors. In the first stage of the BeyondPlanck program, the collaboration will perform end-to-end analysis of the *Planck* LFI data, with the main goal of producing new state-of-the-art frequency and foreground maps. These maps aim to be the world's cleanest and most sensitive full-sky estimates at the given frequencies and will be vital for future CMB B-mode research forming a new baseline.

Chapter 2

The Zodiacal Light

Before we dive deeper into the topic of cosmological component separation, the main subject of this thesis will have to be introduced, namely the *Zodiacal Light*. The Zodiacal Light is most commonly known as a celestial phenomenon to the average stargazer. To a cosmologist, on the other hand, the phenomenon plays the role of an important foreground in high-frequency CMB analysis. In contrast to most foregrounds that originate from Galactic physical processes, the Zodiacal Light emerges from within our Solar System as the only[1] local source of foreground contamination present in cosmological data. In this chapter, we will introduce Zodiacal Light as a physical phenomenon, and look at the historical, cultural, and scientific significance of the phenomenon. The following sections are based on the introductory chapter of the doctorate dissertation of B. H. May (2007)[24].

2.1 The physical phenomenon

The Zodiacal Light, which we will hereby refer to as ZL is the name given to a strange illumination that briefly appears on the sky during twilight in the western sky, and during dawn in the eastern sky. The illumination takes the shape of a diffuse cone, rising from the recently set, or emerging Sun. A typical view of the illumination is seen in Figure 2.1, where the ZL is imaged over the La Silla observatory in Chile. The phenomenon occurs when sunlight scatters off the surface of small grains of interplanetary dust (IPD) distributed around the Solar System. The IPD is believed to be the remains of asteroid collisions, cometary activity, and other artifacts from the Kuiper belt and planetary formation. The geometry of the IPD distribution resembles that of an ellipsoid aligned with the ecliptic, centered on the Sun, often referred to as the *Zodiacal Cloud*.

The phenomenon is short-lived when observed from Earth and disappears along with the Sun behind the horizon after some time. The light is then absent throughout the night until some time before dawn, where it is seen rising from the opposing horizon. Due to its faint nature, the ZL is often rendered invisible when viewing conditions are not

---

[1] One could argue that planets should be considered a foreground.

Figure 2.1: The Zodiacal Light seen in *Zodiacal light over La Silla* by ESO/Y. Beletsky [25]. The diffuse light takes the form of a cone aligned with the ecliptic in this image taken some minutes after the Sun had set in the La Silla observatory in Chile.

optimal. To properly observe the celestial spectacle from Earth, one needs a cloud-free night sky, with minimal amounts of light pollution and moonlight. Another advantage is to observe from within the tropics as the light cone becomes inclined at a higher angle, resulting in a longer up-time. Despite the dim nature of the phenomena, the maximum intensity of the ZL can rival the most luminous parts of the Milky Way. On some occasions during ideal viewing conditions, the twilight and dusk cones can appear to connect by a continuous faint band aligned with the ecliptic. This band, although faint can remain visible throughout the night and may even reveal a secondary brightening, directly opposite to the Sun, called *Gegenschein*, which is German for countershine. This bright spot is believed to be the result of *backscattering*, which is light that is diffusely reflected in the direction from which they came.

2.2 Early sightings and cultural significance

The Zodiacal Light is not mentioned by any of the early Greek or Arabian writers in astronomy though it seems unlikely to have escaped their notice. According to the article, The Zodiacal Light [26] by Arthur K. Bartlett published in the *Popular Astronomy* in 1902, the first written records which directly references the phenomenon may be credited to the ancient Aztecs. An Aztec manuscript preserved in the Bibliotheque du Roi, now the national library of France is said to contain a record of a mysterious light which was visible for forty consecutive nights in the year 1509, the same light which Montezuma II regarded as an omen of his downfall. This mysterious light might have been an unusually luminous appearance of the ZL as the observational details correctly match the structure and position of the IPD distribution.

Oral Muslim tradition suggests that the ZL played a significant role in the timing of the five daily prayers in Islam. Prophet Muhammad is said to have given an accurate description of the illumination, which he called the *False Dawn*, allowing practicing Muslims to differentiate between the False and True Dawn[2]. The phenomenon was later immortalized in the Rubaiyat of the great Persian astronomer and poet, Omar Khayyam. The following passage is taken from the 1859 English translation of the book:

> “*When False Dawn streaks the East with cold, gray line, Pour in your cups the pure Blood of the vine; The Truth, they say, tastes bitter in the mouth, This is a token that the "Truth" is wine.*” ,

which is a clear reference to the ZL.

2.3 Scientific discovery

In the late 16th century, the ZL was brought to the attention of the western world by J. Childrey. In his work, *Britannia Baconica* (1660) Childrey wrote the following:

> “*In February you shall see a plainly discernible way of the twilight striking up towards to the Pleiades... and I believe it... will be constantly visible at that time of the year. But what the cause of it in Nature should be I cannot yet imagine but leave it to further enquiry.*”

It was not until twenty-two years later, in 1685 when the famous French astronomer Giovanni Domenico Cassini presented a paper on the phenomenon [27] that we first began to understand the ZL. Cassini was the first to attribute a physical explanation to the phenomenon, and because of this, the ZL discovery is credited to him. He imagined that a lenticular cloud of dust centered on the Sun with its axis lying in the plane of the ecliptic could be responsible for the observed brightness pattern. The title of his paper (from which the name Zodiacal Light derives) *Découverte de la lumière celeste qui paroist dans le zodiaque* is translated to Discovery of the celestial light that appears in the Zodiac. The Zodiac is the name of an imaginary band aligned with the ecliptic containing all known constellations. The name itself is Ancient Greek and translates to a circle of little animals, which reflects the prominence of animals in the constellations.

---

[2] The True Dawn denotes the time at which the first of the five daily prayers is performed by practicing Muslims.

2.4 Developments in Zodiacal Light research

Our understanding of the ZL remained unchanged for nearly three centuries following Cassini's discovery. A slightly improved formulation was forwarded by the Soviet Russian astrophysicist Vasily Fesenkov in the early 1940s who suggested that the Zodiacal Cloud around the Sun was better represented by a prolate spheroid surrounded by a dust torus. Yet, it was not until we obtained data from space-based telescopes, most notably from the Infrared Astronomical Satellite (IRAS) and the DIRBE instrument from COBE that we understood the true complexity of the IPD distribution.

In 1983 the IRAS space telescope was launched to map the full sky at infrared wavelengths; the wavelengths at which thermal dust, including the Zodiacal Light Emission (ZLE), dominates the sky. A year after the launch, Hauser et al. (1984) [28] found a seasonal intensity dependence on the observed ZL due to asymmetries in the IPD distribution. The Zodiacal Cloud was found to exhibit both a tilt with respect to the ecliptic by some 2 degrees, and a small offset of 0.13 AU from the barycenter of the Solar System, likely dictated by planetary perturbations. The results from the IRAS survey further revealed previously unknown warm structures within the Solar System. In particular, three band pairs of dust were discovered by Low et al. (1984)[29] which were associated with the main asteroid belt due to their ecliptic latitudes and derived distances. Furthermore, Dermott et al. (1994) [30] found observational evidence of a circumsolar ring of dust, just outside of the orbit of Earth. Such orbital rings were predicted by T. Gold in 1975[31], who suggested that dust grains spiraling in towards the Sun from the outer Solar System may get trapped in resonant orbits around major bodies due to gravitational perturbations. Following the launch of COBE, Reach et al. (1995)[32] was able to confirm the existence of a circumsolar ring with a width of 0.4 AU. They also showed that the ring was asymmetric with an enhancement of dust in the region trailing the Earth.

The aforementioned discoveries painted a detailed picture of the IPD distribution compared to the traditional lenticular Zodiacal Cloud. The IPD distribution was now a complex structure consisting of multiple individual Zodiacal components, each symmetrically distributed about an inclined plane with respect to the ecliptic. The composition of these components is still debated, but they are mostly attributed to asteroidal and cometary origins. Reach et al. (2003) [33] found that the observed ZLE was consistent with thermal radiation emitted by particles of sizes in the 10-100 micrometers range. Particles smaller than this would have resulted in selectively scattered light according to wavelength, which was yet to be observed. The proximity of the IPD grains to the Sun imposes a constraint the lower limit of the particle radius; particles smaller than ~ 0.3 micrometers are ejected from the Solar System by the pressure of sunlight (Giese, R. H. 1963)[34]. The exact composition of the IPD is believed to consist of silicates, carbonaceous minerals, metals, sulfides, water ice, or a combination of these.

2.5 Zodiacal Light in modern observational cosmology

Developing a better understanding of the ZL was never the main objective of any space-based observational mission. These missions were mainly directed at evaluating the infrared emission from Galactic or extragalactic sources, such as the CIB. It was the necessity of removing foreground contamination emitted by the IPD that motivated the detailed analysis of the IPD distribution. In addition to reflecting sunlight, dust grains also emit thermal radiation from being heated by the Sun. This thermal emission is one of the dominating sources of diffuse sky brightness in the infrared regime and consequently had to be carefully understood and modeled if not to affect the IRAS and COBE results. The same is true for newer observational missions, such as the *Planck* satellite, and any future missions that plan to observe at higher frequencies where ZLE significantly contributes to the sky brightness. It was this requirement that motivated the first full IPD model, which was developed by the DIRBE team. The DIRBE model is described in detail in chapter 5, which considers IPD modelling.

When it comes to modern component separation, ZLE in CMB data is usually modeled and removed through stand-alone software. However, the inevitable transition to the time-domain in CMB analysis requires this to change. To produce end-to-end results that accurately represent the ZLE as seen at the time of observation, the IPD model has to be integrated into the main pipeline of component separation software.

Before we delve into models of the IPD and how these are used in component separation to remove ZLE from cosmological maps, we will take a more general look at what types of signals we can expect to find in observational data sets, in hopes of better understand the component separation process. After all, the IPD is only one in a magnitude of various signal sources observed when studying the microwave sky.

Chapter 3

The Microwave Sky

CMB experiments such as COBE, WMAP, and *Planck* do not observe a perfect CMB signal. The sky which they scan consists of considerable amounts of radiation that originate from sources besides the CMB. This is evident in the full-sky frequency maps produced by *Planck*, seen in Figure 3.1. These maps reveal the variation in the sky as a function of the frequencies in the microwave regime. The observed differences to the sky appearance are the outcome of physical phenomena operating within different frequency ranges. Most of the foreground signal seen in these maps are of Galactic origins, but some signal does arise from extra-galactic, and even local phenomena. In this chapter, we introduce all the sky components expected to be present in observational CMB data with a focus on the relevant signal sources for the BeyondPlanck data sets. The following discussion is based on BeyondPlanck Collaboration I (2020) [23].

In general, cosmological data can be modeled as

$$\boldsymbol{d}_\nu = \boldsymbol{s}_\nu + \boldsymbol{n}_\nu, \tag{3.1}$$

where $\boldsymbol{d}_\nu$ is a set of data observed at some frequency ν, $\boldsymbol{s}_\nu$ is the total signal of all observed sky components at that frequency, and $\boldsymbol{n}_{\boldsymbol{\nu}}$ the noise. Being able to differentiate sky components from one another is the essence of component separation and requires a good understanding of the composition, morphology, and origin of each component. Before we continue our discussion on the sky components and the aspect of modelling them, we need to be able to quantify their radiation in terms of a physical unit. There exist many different conventions depending on the particular application of interest. In the context of this thesis, we will only consider the three most common conventions.

The first measure is the *surface brightness per solid angle*, which is the measure of the energy emitted by some source per surface area, per frequency interval, and per solid angle on the sky. This measure typically quantifies the intensity, I_ν, of some radiation source as a function of frequency, and is often measured in units of MJy sr^{-1} $\equiv 10^{-20}$Wm^{-2}Hz^{-1}sr^{-1}.

Secondly, we have the *thermodynamic temperature* measure denoted by $\mathrm{K_{CMB}}$ or simply K. We can identify the intensity emitted by a blackbody source with temperature

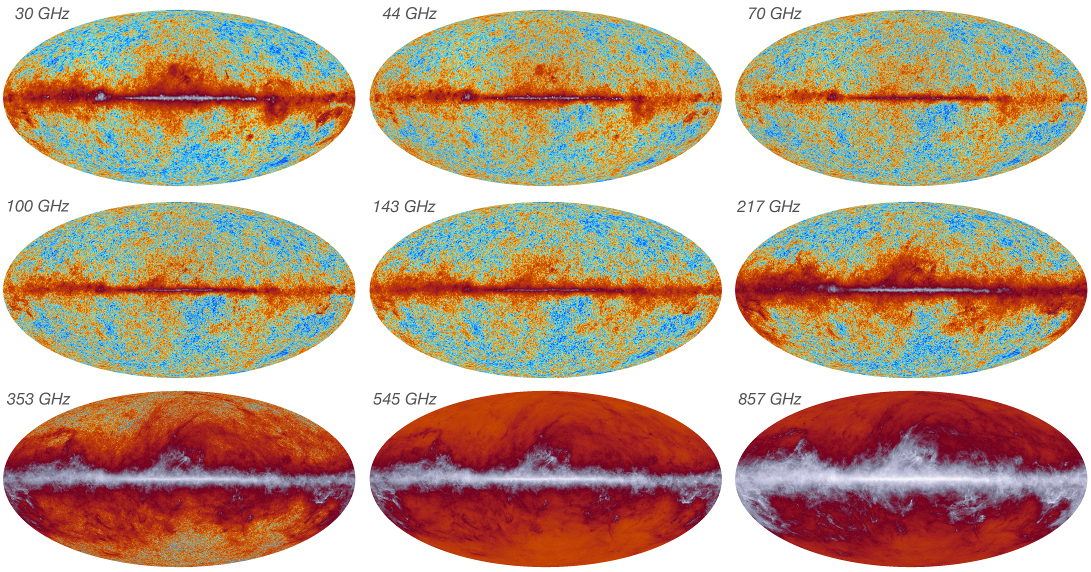

Figure 3.1: The *Planck* 2018 frequency maps, illustrating the difference in the observed sky signal at different frequencies (Image from the UK outreach site for the *Planck* mission [35]).

T as a function of frequency as

$$I_\nu = B_\nu(T) = \frac{2h\nu^3}{c^2}\frac{1}{e^{\frac{h\nu}{kT}} - 1}, \tag{3.2}$$

where h is Planck's constant, c is the speed of light, and k is Boltzmann's constant. This measure is useful for CMB analysis as the CMB itself is a near perfect blackbody, meaning that a single temperature $T(\hat{n})$ uniquely specifies its intensity at a given position at any frequency.

The final measure is the *brightness temperature*. Unlike the CMB, most foregrounds exhibit radiation of a non-thermal nature. Such components are more naturally quantified in terms of their brightness temperature, or Rayleigh-Jeans temperature T_{RJ}, denoted by $\mathrm{K_{RJ}}$. The brightness temperature is defined as the long-wavelength limit ($h\nu \gg kT$) of equation 3.2, such that the intensity is given as

$$I_\nu = \frac{2h\nu^2 kT_{\mathrm{RJ}}}{c^2}. \tag{3.3}$$

We can convert back and forth between these units. For a single frequency, equation 3.3 can be used to convert between MJy sr^{-1} and K_{RJ}. Similarly, we can convert between $\mathrm{K_{CMB}}$ and $\mathrm{K_{RJ}}$ through the following equation

$$\Delta T_{\mathrm{CMB}} = \frac{(e^x - 1)^2}{x^2 e^x} T_{\mathrm{RJ}}, \tag{3.4}$$

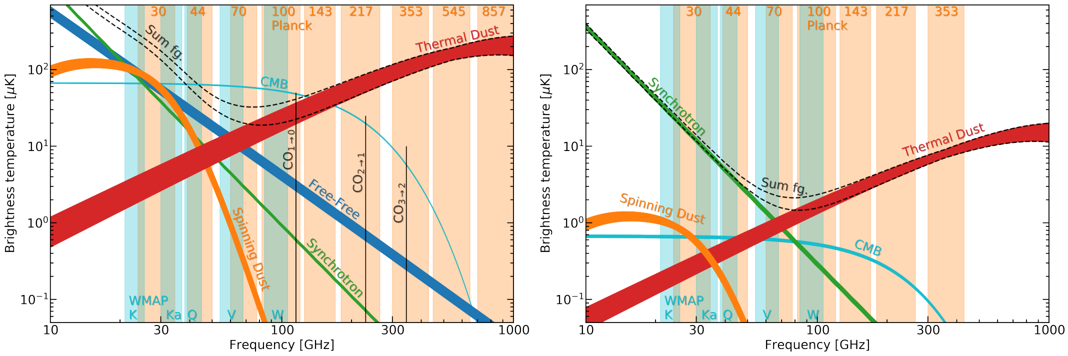

Figure 3.2: Foreground intensity in temperature (left) and polarization (right) as a function of frequency over the *Planck* frequencies. The red and blue bands represent the frequency bands observed by *Planck* and WMAP respectively (Images from the spectrum code of Trygve Leithe Svalheim [36]).

where $\Delta T \equiv T - T_0$, $x = h\nu/kT_0$, and T_0 is the mean CMB temperature today. Note that this conversion only applies to small temperature variations around the CMB mean value.

Another most important quantity related to a sky component is its spectral energy distribution (SED). It is given in units of brightness and acts as one of the primary quantities of interest in component modelling. The SED of a component describes how the energy of its sky signal is distributed with frequency. Figure 3.2 shows the SEDs of the various foregrounds present at the *Planck* frequencies, for both temperature (left) and polarization (right). With these definitions in place, we are ready to elaborate on the many sky components present in the data sets relevant to the BeyondPlanck project.

3.1 Cosmic microwave background

The first sky component we will discuss is the CMB. The CMB is left-over heat from the Big Bang and fills the entire universe with a near isotropic blackbody signal. The near-perfect blackbody nature of the signal means that its temperature uniquely specifies its intensity at any wavelength at a given position. Today the CMB signal is observed to have a temperature of $T_0 = 2.7255$ K. The CMB photons have not always been traveling freely throughout the Universe as they do today. In the time ensuing the Big Bang, the CMB photons were trapped locally within a dense electron-proton plasma through Thompson scattering. As the Universe expanded, the mean plasma temperature dropped below 3000 K which allowed electrons and protons to combine into neutral hydrogen atoms, turning the Universe transparent. The photons were no longer held captive by the dense plasma and could freely propagate throughout the entire universe with little to no further scattering. This event is referred to as the epoch of *recombination* and took place some 380 000 years after the Big Bang. When we observe CMB photons today, they appear to come from the *last-scattering surface* which is the

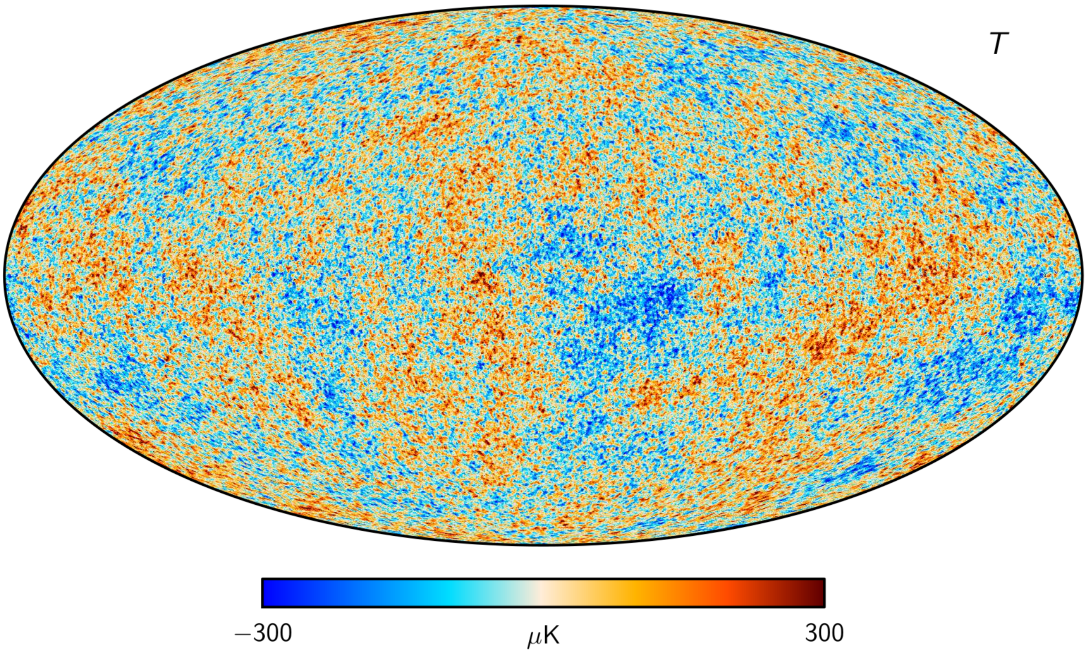

Figure 3.3: CMB temperature map produced by `Commander` for the *Planck* 2018 release [37].

surface of a sphere around the observer where the radius of the sphere is the distance each CMB photon has traveled since it was last scattered at recombination.

Despite the high levels of isotropy exhibited by the CMB, it does reveal small spatial variations at the order of 100 μK. These anisotropies are visible in Figure 3.3, which shows the state-of-art CMB map from *Planck* 2018. These fluctuations are the results of variations in the density, temperature, velocity, and gravitational potential at the last-scattering surface and they act as one of the most important sources of information in physics by being in some sense the "footprints" of the early universe. Extracting all of the cosmological information embedded in the CMB is, however, not easy. As we previously mentioned, the goal for next-generation CMB experiments and analysis is the detection of primordial gravitational waves through their polarization imprint on the CMB. The aforementioned B-modes vital for this discovery are likely to exhibit amplitudes no larger than 100 nK. To detect variations at this order of magnitude, we need to understand foregrounds and treat any systematic or instrumental errors to the same level of sensitivity. This is where the BeyondPlanck collaborations ambitious framework comes in to play, but more on this in chapter 4.

The CMB sky component $\boldsymbol{s}^{\mathrm{CMB}}$ is modeled by assuming that the CMB SED can be approximated as a blackbody. Accordingly, its brightness temperature SED is given by the conversion in equation 3.4 as

$$\boldsymbol{s}_{\mathrm{RJ}}^{\mathrm{CMB}}(\nu) \propto \frac{x^2 e^x}{(e^x-1)^2}\boldsymbol{s}^{\mathrm{CMB}}, \tag{3.5}$$

where $x = h\nu/kT_0$.

3.2 Galactic foreground components

The most important class of emissive sky components, other than the CMB itself, is the diffuse Galactic foregrounds. These are sky components that originate from within the Milky Way. They are the result of various ongoing physical processes in our galaxy where particles, electrons, ions, or dust interacts with one another or radiation. We will now give a brief introduction to each of the main physical emission mechanisms in addition to explaining how they are modeled in BeyondPlanck.

3.2.1 Synchrotron emission

Synchrotron emission is the dominating sky component at the lower microwave frequencies. The emission is produced when relativistic electrons ejected by supernova are accelerated by the Galactic magnetic field in a spiraling motion. This radiation is highly polarized (up to $\sim 75\%$) due to its spiraling nature. At low frequencies, polarized synchrotron radiation is heavily affected by Faraday rotation, an effect where the polarization angle of emission rotates due to left and right circularly polarized photons moving at different velocities through a magnetic field. The strong polarization nature of the emission makes synchrotron an important foreground in polarized CMB analysis.

When it comes to modelling the synchrotron emission, detailed models and observations suggest that the synchrotron SED can effectively be approximated by a power-law for the relevant BeyondPlanck frequency ranges. The model used in BeyondPlanck is an extension of the general synchrotron SED model from Kogut (2012) [38]. It is given by

$$\boldsymbol{s}^{\mathrm{s}}_{\mathrm{RJ}}(\nu) \propto \left(\frac{\nu}{\nu_{0,\mathrm{s}}}\right)^{\beta + C \ln \nu/\nu_{0,\mathrm{s}}}. \tag{3.6}$$

Here ν_0 is some reference frequency, β is a power-law index, and C is a curvature parameter. The data sets considered in BeyondPlanck does not have a sufficient signal to noise ratio to constrain the curvature parameter, meaning that for most cases the curvature parameter is set to zero, $C = 0$.

The structure of the Galactic synchrotron emission can be seen in the full-sky synchrotron intensity map from the *Planck* 2015 release, shown in Figure 3.4. The typical characteristics of synchrotron emission in maps is a strong signal in the Galactic center in addition to the arc of radiation known as the North Galactic Spur which is projecting from the Milky way towards the north galactic pole. This spur is believed to be the expanding shell of a supernova remnant.

3.2.2 Free-free emission

Free-free emission, also known as *bremsstrahlung* (German for braking radiation) is radiation emitted from interactions between free electrons and ions. Free electrons

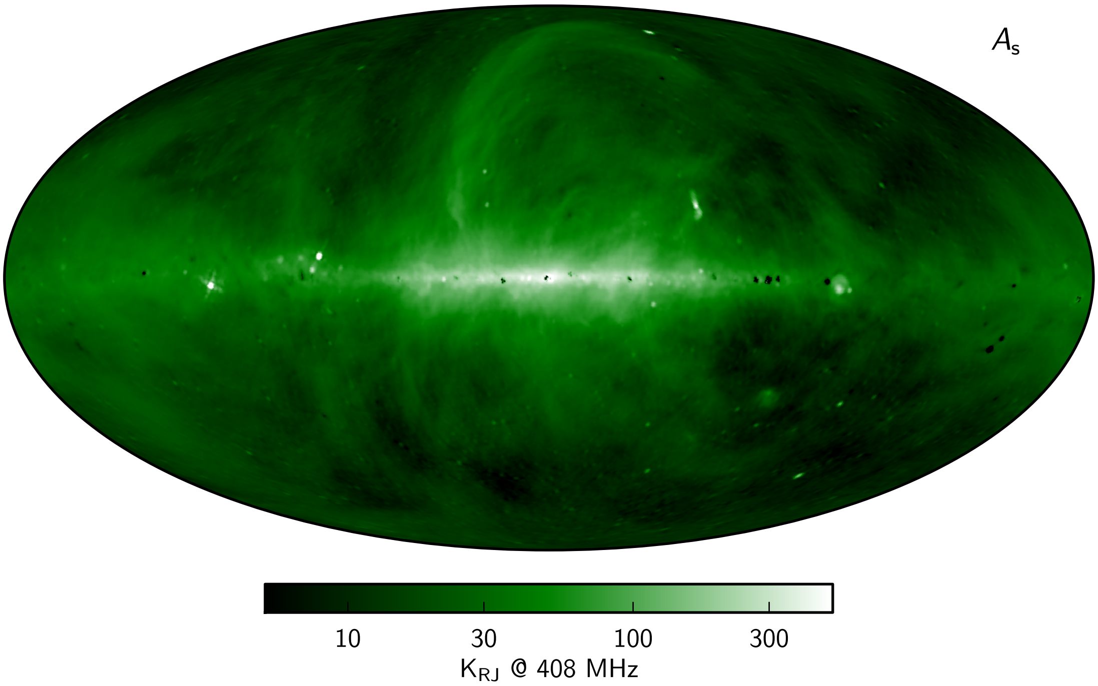

Figure 3.4: Full-sky synchrotron intensity map produced by `Commander` for the *Planck* 2015 release [39].

usually only exist in considerable amounts in regions where the temperature of the surrounding medium is comparable to the binding energy of hydrogen ($10^3 - 10^4$ K). Free-free emission, therefore, acts as a tracer of hot star-forming regions where stellar radiation ionizes and heat atoms in the surroundings. As such, the energy emitted during an interaction is highly dependant on the electron temperature, T_e.

Modelling free-free emission is somewhat more complicated compared to synchrotron emission, as the SED primarily depends on the number of free electrons along the line-of-sight. In BeyondPlanck, a simple linearized form which is strictly only valid in an optically thin medium is adopted, reading

$$\boldsymbol{s}^{\mathrm{ff}}_{\mathrm{RJ}}(\nu) \propto \frac{g_{\mathrm{ff}}\left(T_e\right)}{\nu^2}, \tag{3.7}$$

where g_{ff} is called the Gaunt factor related to the optical depth. There exists no effective alignment mechanism for thermal electrons in a hot medium. As such, large-scale free-free emission is expected to be nearly unpolarized. Free-free is the only component that is non-negligible over the frequency range of 1 to 1000 GHz, making it especially sensitive to degeneracies with respect to the CMB and the other sky components. As such, the foreground is of particular importance to component separation.

The free-free emission structure can be in the full-sky free-free intensity map from the *Planck* 2015 release, shown in Figure 3.5. Typical characteristics of free-free maps

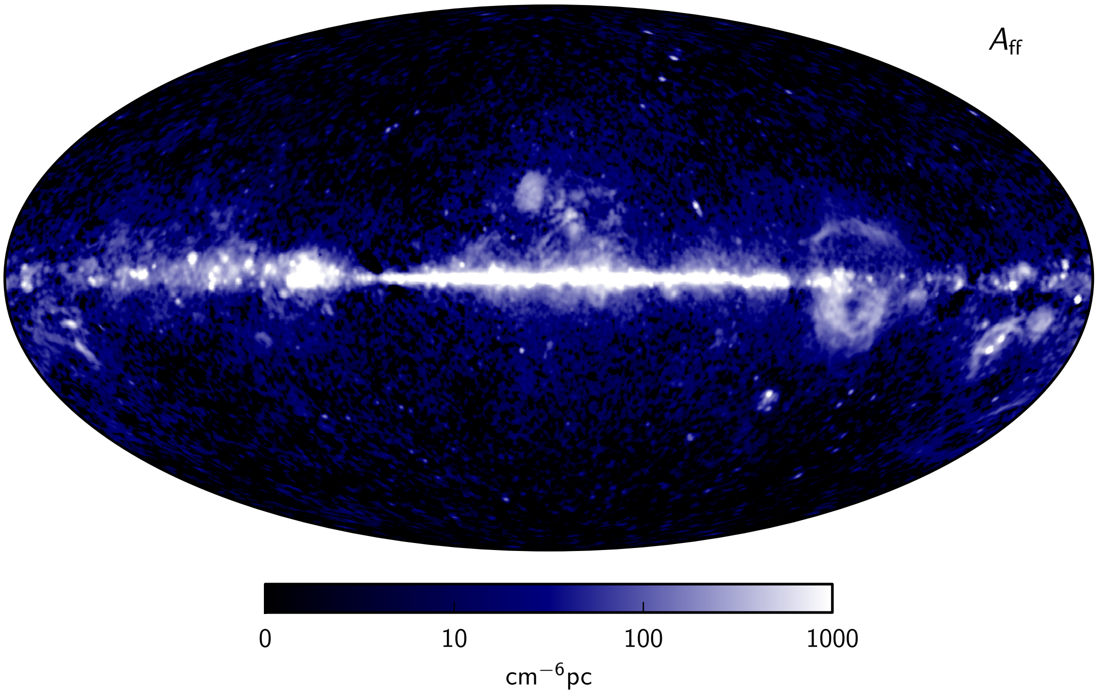

Figure 3.5: Full-sky free-free intensity map produced by `Commander` for the *Planck* 2015 release [39].

are the feature seen directly North of the Galactic center, along with the torus-shaped structure south-east of the Galactic center.

3.2.3 Thermal dust emission

Radiation from thermal dust is the dominating Galactic foreground at frequencies above 100 GHz. The radiation is thermal similar to ZLE and is the result of dust grains filling the interstellar medium (ISM) being heated up by starlight. The thermal energy of the grains is then radiated away in the microwave and infrared regime. The dust grains are thought to be of stellar origins. As stars die, their metal-rich outer layers are blown off either through a supernova event or through radiation pressure. The contents of these layers eventually form cold nebulae or molecular clouds. Inside these clouds, carbon and silicon atoms combine to form simple molecules, which further clump together into dust grains. These grains are believed to be ranging in size from a few nanometers to a few micrometers, depending on their environment. Regardless of their precise composition, all ISM dust grains are heated by nearby stellar radiation such that they equilibrate at some effective temperature in the range 10 to 30 K.

Modelling thermal dust emission proves to be somewhat complicated, mostly because of the varying composition of the ISM dust grains. It is therefore normal to make use of a simple fitting formulation for practical component separation analysis. In particular, one typically adopts a so-called modified blackbody spectrum which in intensity

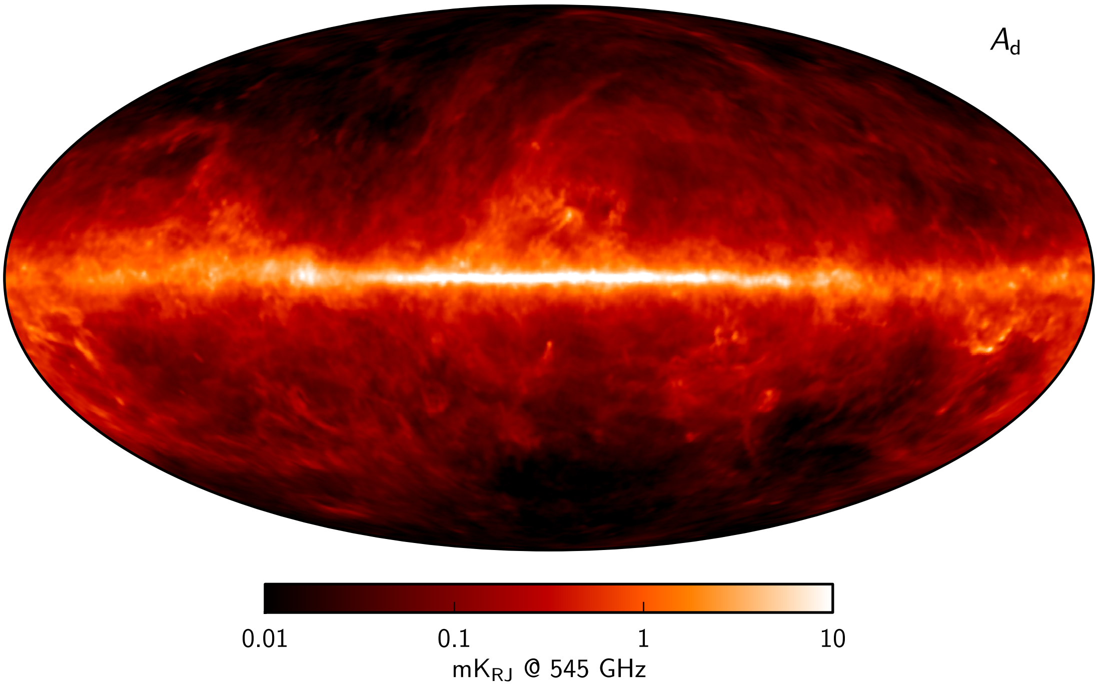

Figure 3.6: Full-sky thermal dust intensity map produced by `Commander` for the *Planck* 2015 release [39].

reads

$$I_\nu^{\mathrm{d}} \propto \tau \nu^{\beta_{\mathrm{d}}} B_\nu\left(T_{\mathrm{d}}\right), \tag{3.8}$$

which is the blackbody spectrum $B(\nu)$ given by equation 3.2, with temperature T_{d} determining the SED peak position modulated by a power-law index β_{d} that determines the slope of the SED. The optical depth, τ, depends directly on the surface density of particles along the line-of-sight and determines the amplitude of the intensity similar to free-free emission. Thermal dust emission is modeled in units of brightness temperature where the SED takes the form

$$\boldsymbol{s}_{\mathrm{RJ}}^{\mathrm{d}}(\nu) \propto \frac{\nu^{\beta_{\mathrm{d}}+1}}{e^{h\nu/kT_{\mathrm{d}}}-1}. \tag{3.9}$$

Dust grains can contain iron in their composition. Such grains exhibit a non-zero magnetic moment that results in the dust aligning along any local magnetic field. As a result, up to 20% of thermal dust emission is found to be polarized. The structure of thermal dust emission can be seen in the full-sky thermal dust intensity map from the *Planck* 2015 release, shown in Figure 3.6. Thermal dust maps are often characterized by strong emission along the entire Galactic plane as dust covers much of the sky.

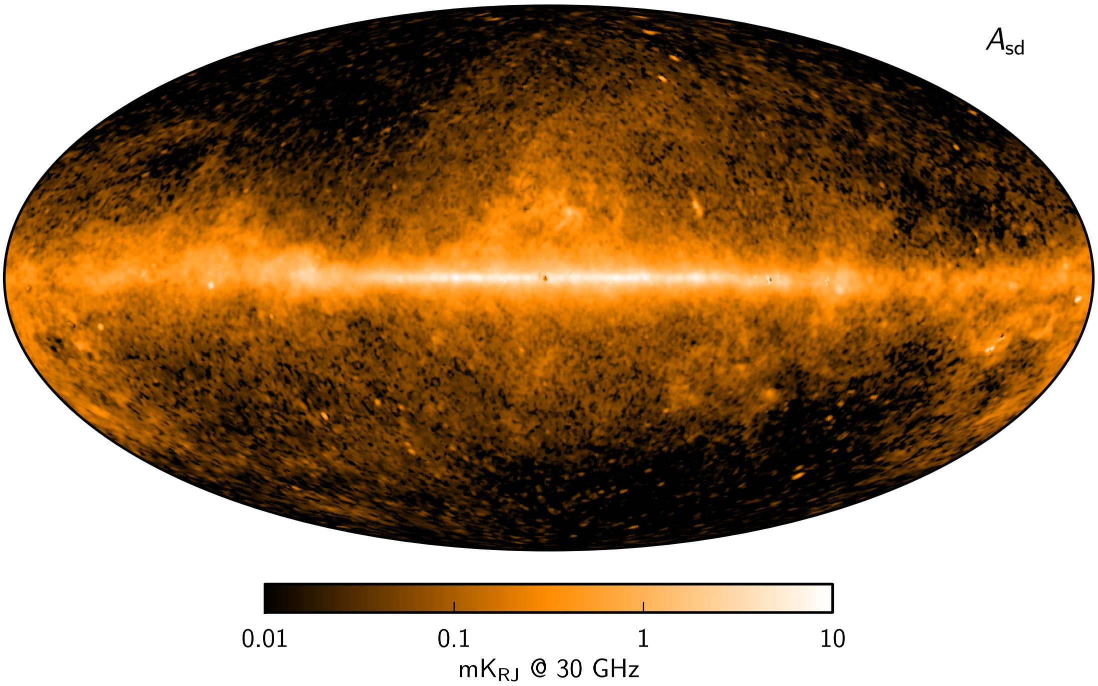

Figure 3.7: Full-sky map of spinning dust intensity produced by `Commander` for the *Planck* 2015 release [39].

3.2.4 Spinning dust (anomalous microwave) emission

In the preliminary stages of component separation, one only believed there to be three main diffuse foreground components, those being synchrotron, free-free, and thermal dust emission. However, some of the first papers on component separation reported strange results. Leitch et al. (1997) [40] found a significant excess of Galactic emission in the 10-40 GHz frequency range near the north celestial pole which was strongly correlated with thermal dust emission. They named this strange component Anomalous Microwave Emission (AME).

It was later shown by Draine, B. T., and Lazarian, A. (1998) [41] that AME could be accounted for by spinning interstellar dust grains. In addition to vibrating due to internal heat, dust grains can also rotate. Spinning grains of dust with a non-zero electric dipole would produce detectable radiation in the 10-100 GHz frequency range. Before the spinning dust theory, it was believed that the AME could be a form of free-free emission. However, the energy required for electrons to produce the observed AME signal would imply electron temperatures of $T \geq 10^6$ K rivaling supernova levels. The free-free hypothesis was therefore dismissed on energetic grounds. Today, the spinning dust theory remains the best description of the AME and recent observational progress with the WMAP and *Planck* experiments (*Planck* Collaboration XX (2011) [42]) has shined additional light onto the physical nature of the AME, further supporting the spinning dust theory.

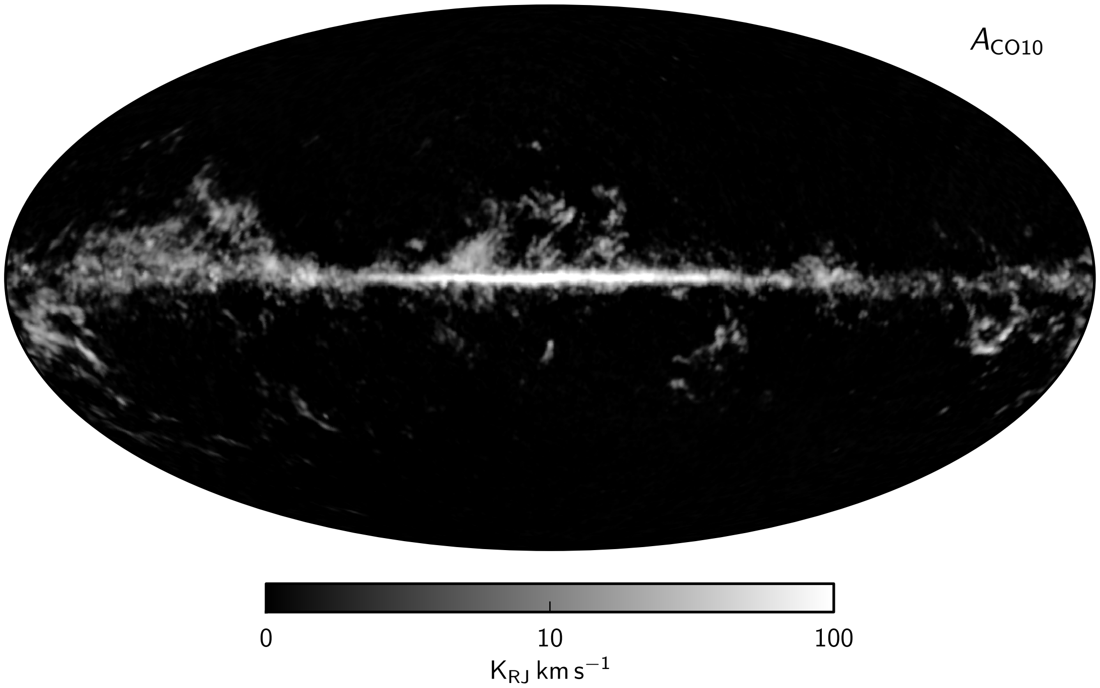

Figure 3.8: Full-sky map of the carbon monoxide emission resulting from the $J = 1 \rightarrow 0$ transition, produced by `Commander` for the *Planck* 2015 release [39].

BeyondPlanck adopts a spinning dust model based on a numerically computed SED template $\boldsymbol{s}_0^{\mathrm{sd}}(\nu)$ for a cold neutral medium. This spectrum is computed in units of intensity and peaks at 30 GHz. The template is then converted to brightness temperature and fitted to data through a peak position parameter ν_{p}, following the works of Bennett et al (2013) [43]. The resulting SED model is given by

$$\boldsymbol{s}_{\mathrm{RJ}}^{\mathrm{sd}}(\nu) \propto \nu^{-2} \boldsymbol{s}_0^{\mathrm{sd}} \left(\nu \cdot \frac{30.0\mathrm{GHz}}{\nu_p} \right). \tag{3.10}$$

The structure of spinning dust can be in the full-sky spinning dust intensity map from the *Planck* 2015 release, shown in Figure 3.7. It strongly resembles the structure of thermal dust emission.

3.2.5 Carbon monoxide emission

Molecules can emit radiation if they have a non-zero electric dipole, much like rotating dust particles. An example of such a molecule is carbon monoxide (CO) which behaves like a foreground due to its abundance and distribution throughout the galaxy. CO molecules are produced alongside dust through star formation and are commonly found in the two forms $^{12}\mathrm{C}^{16}\mathrm{O}$ (abbreviated to $^{12}\mathrm{CO}$), and $^{13}\mathrm{C}^{16}\mathrm{O}$ ($^{13}\mathrm{CO}$), where the superscripts refer to the nucleon number (number of protons + neutrons in the nucleus). The form $^{12}\mathrm{CO}$ is 10-100 times more abundant than $^{13}\mathrm{CO}$.

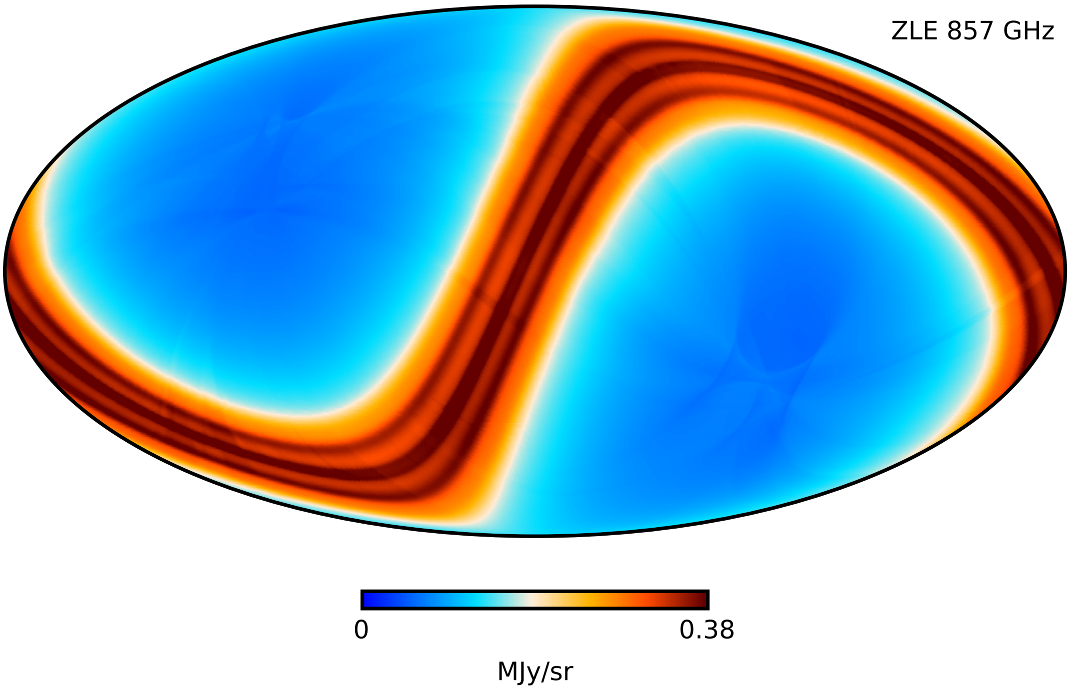

Figure 3.9: Full-sky Zodiacal emission template at 857 GHz used for Zodiacal correction in the 2015 *Planck* analysis. Units are MJy/sr.

In contrast to the other foregrounds discuss so far, CO emission is not continuous over the frequency spectrum. The emission is the result of discrete energy transitions in the molecule. Such a transition occurs when the molecule either absorbs or emits a photon. From quantum mechanics, we know that the allowed transitions emit photons with frequencies

$$\nu_0 = \frac{\hbar J}{2\pi I}, \quad J = 1, 2, \ldots \tag{3.11}$$

where $J = 1, 2, \ldots$ is the angular momentum quantum number, and I is the moment of inertia of the CO molecule. The $J = 1 \leftarrow 0$ transition results in a frequency of $\nu_0 = 115.27$ GHz for ^{12}CO, and 110.20 GHz for ^{13}CO. Any higher-order transitions are simply multiples of these frequencies. The frequencies where we observe CO emission is illustrated in Figure 3.2 (left). Since CO emission is essentially just a sharp line frequency, the corresponding SED can be given by a delta function at the respective frequencies as following

$$\boldsymbol{s}_{\mathrm{RJ}}^{\mathrm{CO}}(\nu) \propto \delta\left(\nu - \nu_0\right). \tag{3.12}$$

The structure of the CO line emission can be seen in the full-sky CO ($J = 1 \rightarrow 0$ transition) intensity map from the *Planck* 2015 release, shown in Figure 3.8. CO maps are often characterized by the shark-fin-like feature just north-west of the Galactic center.

3.3 Zodiacal Light emission

The final foreground we will consider, the ZLE is also the most important in the context of this thesis. ZLE was introduced in chapter 2 as the only local foreground. The emission is thermal and is in many ways identical to thermal dust emission. What separates ZLE from Galactic thermal dust emission, and more generally the other foregrounds is the proximity between the observer and the source of emission. Radiation from Galactic foregrounds can be assumed to originate from infinity. This is not the case for ZLE. The observed ZLE is sensitive to the exact position of the observer. Most observational missions are not stationary, meaning that the observed emission will vary throughout an observational survey. As such, ZLE appears as a variable foreground. Figure 3.10 illustrates how the IPD density along a line-of-sight to a specific celestial position changes throughout an observational survey.

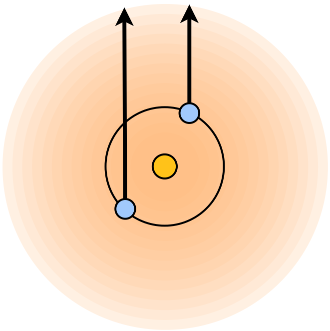

Figure 3.10: Illustration of how an observer can view different amounts of ZLE along a line-of-sight while looking at the same point on the distant sky. The yellow and blue dots represent the Sun and the Earth, respectively, at two different orbital positions. The black circle represents the orbit of the Earth. The orange cloud wrapped around the system represents the IPD distribution. The two arrows pass through different amounts of IPD.

The temporal variance of the ZLE requires the foreground to be dynamically modeled. The accuracy of Zodiacal corrections is therefore constrained by our understanding of the IPD distribution. There exists a variety of models describing the IPD distribution in the Solar System. Most notable is the DIRBE parametric model (Kelsall et al. (1998) [44]), successfully applied to perform Zodiacal corrections in both the COBE and *Planck* missions. In short, the DIRBE model functions by producing a map that represents the estimated ZLE contained in a data set. This map, sometimes referred to as a ZLE template, is then used in component separation to perform Zodiacal corrections. Figure 3.9 shows the ZLE template used for Zodiacal corrections in the 2015 *Planck* analysis [45]. In contrast to typical foreground maps where the emission is mostly distributed about the Galactic plane, the ZLE template exhibits an s-shaped structure. This is due to a difference in coordinate systems. Cosmological sky maps are usually plotted in Galactic coordinates, and in these coordinates, the ecliptic appears as the s-shape seen in the ZLE map.

3.4 Extra-galactic foreground emission

In addition to the Galactic foregrounds, there exist several extra-galactic mechanisms that cannot be neglected if one is to discover the elusive primordial gravity waves. We will only introduce the most relevant mechanisms in the following to keep the discussion short and relevant.

3.4.1 Extra-galactic compact sources

Some galaxies have so-called active galactic nuclei (AGN). This means that the supermassive black hole at the center of the galaxy powers quasars and other types of AGN through the accretion of interstellar gas. Such AGN's dominate the radio source population and emits mostly synchrotron radiation. These radio sources are distributed mostly randomly on the sky and are modeled as point sources in BeyondPlanck.

3.4.2 Sunyaev-Zeldovich effect

Sometimes, CMB-photons happens to have traveled through hot galaxy clusters before being observed by us. In a hot cluster, temperatures can reach up to 10^8 K resulting in an ionized intercluster medium. Traversing CMB photons, therefore, have a non-negligible probability of scattering of the free electrons in the medium, gaining energy in the process. This effect typically shifts the spectrum of the CMB-photons to higher frequencies and must be accounted for in component separation.

3.4.3 Cosmic infrared background

Thermal dust emission is not a phenomenon limited to our galaxy. In general, all galaxies emit some form of thermal radiation from internal dust grains. A background of extra-galactic thermal dust emission is therefore at all times present in the high-frequency data sets. This background signal is referred to as the Cosmic Infrared Background (CIB), as briefly touch on in chapter 1. The CIB may be spatially approximated as a continuous field, with its SED defined as the average of a large number of independent thermal dust SEDs, each appropriately redshifted according to their distance.

Part II

Methods

Chapter 4

Processing and Analysing Cosmological Data

In the previous chapters, we discussed how cosmological data are obtained along with what we expect to find in this type data. We will now enter the realm of component separation where the analysis and processing of observed data take place. Processing and interpreting cosmological data can be hard. Several statistical methods are required to be utilized if one is to go from raw data to cosmological maps and parameters. In this chapter, we will briefly introduce the BeyondPlanck analysis strategy along with its machinery, the Gibbs sampler.

4.1 Time-ordered data and scanning strategy

The main type of data processed by the BeyondPlanck component separation software is time-ordered data. This is data observed in a sequence of equally spaced points in time according to some *scanning strategy*. The scanning strategy is characterized by how the telescope scans the sky. A proper scanning strategy is important to ensure good sky coverage and to minimize systematic effects. The primary data set considered in the initial stage of BeyondPlanck is the *Planck* LFI data, which consists of nine observational surveys, each with varying sky coverage. The HFI data set, which requires Zodiacal corrections, is smaller in volume as the HFI only observed over surveys 1-4 and some of survey 5. *Planck* observed this data from the Sun-Earth Lagrange L2 point as it moved along the ecliptic approximately 1° per day. It scanned the sky while rotating about a spin axis tangential to its ecliptic orbit. *Planck*'s *boresight*, the axis observing maximum signal, was at all times facing away from the Sun at roughly 85° from the spin axis.

4.2 `HEALPix` and data representation

There exist several different ways of representing the observed cosmological data on a digital form. The standard practice in modern CMB analysis is to adopt the `HEALPix`

(Hierarchical Equal Area iso-Latitude Pixelization) pixelization (Gôrski et al. 2005 [46]). The `HEALPix` scheme projects cosmological data, assumed to be originating from the shell of a distant sphere, onto pixels of equal area. These pixels are aligned in a grid such that the center of every pixel occurs on a discrete number of rings of constant latitude. This property allows for fast spherical harmonic transformations; a topic we will introduce shortly. The pixel resolution is defined by the parameter N_{side}, with the total number of pixels on the sky being given by $N_{\mathrm{pix}} = 12N_{\mathrm{side}}^2$. A `HEALPix` grid is typically visualized in the form of a map through the Mollwiede projection, an equal-area map projection.

4.3 The BeyondPlanck analysis framework

The complete component separation pipeline is extensive, even more so in BeyondPlanck, which attempts to develop a single end-to-end analysis framework. Several preliminary steps are required to be carried out before one can even attempt to isolate the various sky components in the data. In the following, we will present a brief step-by-step outline of the BeyondPlanck framework.

1. The first step in the pipeline is the data selection module. Here, raw time-ordered data from the *Planck* LFI are processed through a selection module that identifies and removes bad data segments from further processing.

2. What follows in the second step is a round of calibrations and estimations related to the instruments. This includes gain estimation where the measured voltages in the instrument are translated to astrophysical sky temperatures.

3. Once clean and calibrated data is obtained, the third step considers the production of clean frequency maps through *mapmaking*, a process in which time-ordered data, along with pointing information, are arranged into complete maps.

4. It is only at the fourth step where the component separation process begins. In this step, the well-establish Gibbs sampling framework, `Commander`, is applied to derive the various astrophysical component and frequency maps.

5. The fifth and final step in the analysis chain is dedicated to the physical interpretation of the data, and it is here at the highest-level analysis step where cosmological parameters and the CMB power spectrum is estimated.

Until now, the pipeline has followed a very conventional procedure with a linear progression from the raw data to the final science products. The fundamentally new step in BeyondPlanck is to close the loop which starts with step one (data selection) through step five (physical interpretation) through the computational infrastructure provided by the overall Gibbs sampler, making this a circular and iterative process. This is what makes BeyondPlanck unique in comparison to other CMB analysis pipelines.

4.3.1 `Commander`

To perform component separation, BeyondPlanck adopts the well-established Bayesian CMB Gibbs sampler `Commander`, which was originally developed for *Planck*. The original iteration `Commander1` (see Eriksen et al. 2008 [47]) remains the most mature in terms of the implemented algorithms. It is, however, limited by the need for a common angular resolution over all data sets. `Commander2` got rid of this limitation through explicit beam convolution for each frequency map during component separation, as detailed by Seljebotn et al. (2019) [48]. When we refer to `Commander` in the following, we will refer to `Commander3`; the time-domain version of the software that is being extended by the BeyondPlanck collaboration to incorporate amongst others Bayesian calibration, mapmaking, a Zodiacal Emission module, and to connect component separation and cosmological parameter estimation. `Commander3` will act as a direct generalization and extension of `Commander2` with the main difference being the transition from pixel-domain to the time-domain. All `Commander` source code is available under an open-source license on GitHub [49]

4.4 Bayesian analysis and sampling

Going into detail on the methods mentioned in the step-by-step outline of the BeyondPlanck framework is unnecessary in the contexts of this thesis. We will, however, briefly describe the machinery that acts as the heart and glue of the framework, the Gibbs sampler. The following sections are based on BeyondPlanck I (2020) [23] and the Gibbs sampling review by Eriksen et al. (2008) [47].

4.4.1 Probability theory, spherical harmonics, and the CMB posterior

At the foundation of Gibbs sampling is Bayesian statistics. These are statistics that are particularly useful when we have some prior knowledge about what we want to study. In the case of component separation, we already have models that describe the various foregrounds we expect to find in the observed data, motivating the use of Bayesian statistics. The theory has its basis in Bayes' theorem which states that

$$P(\omega|\boldsymbol{d}) = \frac{P(\boldsymbol{d}|\omega)P(\omega)}{P(\boldsymbol{d})} \propto \mathcal{L}(\omega)P(\omega), \tag{4.1}$$

where $P(\omega|\boldsymbol{d})$ is known as the posterior or the conditional probability; the probability of having a set of parameters ω given some data $\boldsymbol{d}$. The term $P(\boldsymbol{d}|\omega) \equiv \mathcal{L}(\omega)$ is referred to as the likelihood. The prior $P(\omega)$ defines our knowledge (or assumptions) about the set of parameters ω before having observed the data. The final term $P(\boldsymbol{d})$ is referred to as the evidence and acts as a normalization factor. By being independent of ω, the evidence is irrelevant for CMB parameter estimations and is therefore ignored in the following, leaving us with the unnormalized posterior

$$P(\omega|\boldsymbol{d}) \propto P(\boldsymbol{d}|\omega)P(\omega) \tag{4.2}$$

We can demonstrate the applicability of Bayes' theorem to CMB analysis by considering the following simple data model

$$\boldsymbol{d} = \boldsymbol{s} + \boldsymbol{n}. \tag{4.3}$$

Here $\boldsymbol{d}$ is the observed data, $\boldsymbol{s}$ is the CMB sky signal, and $\boldsymbol{n}$ is the instrumental noise. The next step is to evaluate the CMB signal, $\boldsymbol{s}$, on the sphere where it is defined. This is where we make use of the spherical harmonics theorem which states that any function, for instance, the CMB temperature $T(\theta, \phi)$, defined on the sphere may be expanded into spherical harmonics on the form

$$T(\theta, \phi) = \sum_{\ell=0}^{\ell_{\max}} \sum_{m=-\ell}^{\ell} a_{\ell m} Y_{\ell m}(\theta, \phi), \tag{4.4}$$

where $a_{\ell m}$ are the expansion coefficients, and $Y_{\ell m}(\theta, \phi)$ the associated Legendre polynomials. The ℓ and m determine the "wavelength" (number of waves along a meridian) and "shape" (number of modes along the equator), respectively. This decomposition is critical to CMB analysis as it allows us to compute the CMB angular *power spectrum*, a quantity that measures the amplitude $a_{\ell m}$ as a function of wavelength. The power spectrum is given by

$$C_\ell = \frac{1}{2\ell + 1} \sum_{m=-\ell}^{\ell} |a_{\ell m}|^2 , \tag{4.5}$$

and essentially tells us the spectral distribution of power over the different scales. The power spectrum of the CMB signal is one of the most important quantities in CMB analysis as it contains an enormous amount of information about the Universe.

4.4.2 Gibbs sampling

Ultimately we want to estimate both the CMB sky signal $\boldsymbol{s}$ and the power spectrum C_ℓ. Bayesian analysis allows us to estimate these jointly through the joint posterior distribution $P\left(\boldsymbol{s}, C_\ell | \boldsymbol{d}\right)$. The joint posterior distribution generally ends up taking a form that in theory could be mapped out over a grid in $\boldsymbol{s}$ and C_ℓ, based on the data model used. However, the number of grid points required for this type of analysis scales exponentially with the number of free parameters in the model, meaning that this approach becomes impractical in higher-dimensional parameter space. A more efficient approach to this problem is to map out the joint distribution by sampling. One such process is the Markov chain Monte Carlo algorithm called Gibbs sampling (Geman & Geman (1984) [50]). In essence, Gibbs sampling tells us that it is possible to sample from a joint density conditional such as $P\left(\boldsymbol{s}, C_\ell | \boldsymbol{d}\right)$ by alternately sampling from the respective conditional densities

$$\begin{aligned} \boldsymbol{s}^{i+1} &\leftarrow P\left(\boldsymbol{s} | C_\ell^i, \boldsymbol{d}\right), \\ C_\ell^{i+1} &\leftarrow P\left(C_\ell | \boldsymbol{s}^{i+1}, \boldsymbol{d}\right), \end{aligned} \tag{4.6}$$

where ← indicates sampling from the distribution on the right-hand side. Gibbs sampling effectively reduces the problem to that of sampling from the two conditional densities $P\left(\boldsymbol{d}|\boldsymbol{s},C_\ell\right)$ and $P\left(\boldsymbol{s}|C_\ell\right)$. Another benefit of the Gibbs sampling method is that no samples (except for a few drawn during the initial burn-in period) are rejected

Although the Gibbs sampling algorithm forms the main computational framework of BeyondPlanck's analysis pipeline, a variety of different samplers are required to explore the various conditionals as Gibbs sampling only works well for uncorrelated or only weakly degenerate distributions.

4.5 Data modelling in BeyondPlanck

The first step in a Bayesian analysis process is to formulate an explicit parametric model that connects all relevant parameters with the observed data. Naturally, the BeyondPlanck data model is considerably more complex than the model in equation 4.3. The default BeyondPlanck sky model includes all the astrophysical signal sources discussed in chapter 3, and it is given in units of brightness temperature as follows

$$\begin{aligned}
\boldsymbol{s}_{\mathrm{RJ}}^{\mathrm{sky}} = & \boldsymbol{a}_{\mathrm{CMB}} \frac{x^2 e^x}{\left(e^x-1\right)^2} \frac{\left(e^{x_0}-1\right)^2}{x_0^2 e^{x_0}} \\
& + \boldsymbol{a}_{\mathrm{s}} \left(\frac{\nu}{\nu_{0,\mathrm{s}}}\right)^{\beta_{\mathrm{s}}} \\
& + \boldsymbol{a}_{\mathrm{ff}} \frac{g_{\mathrm{ff}}\left(\nu; T_e\right)}{g_{\mathrm{ff}}\left(\nu_{0,\mathrm{ff}}; T_e\right)} \left(\frac{\nu_{0,\mathrm{ff}}}{\nu}\right)^2 \\
& + \boldsymbol{a}_{\mathrm{AME}} \left(\frac{\nu_{0,\mathrm{sd}}}{\nu}\right)^2 \frac{\boldsymbol{s}_0^{\mathrm{sd}}\left(\nu \cdot \frac{\nu_p}{30.0\mathrm{GHz}}\right)}{\boldsymbol{s}_0^{\mathrm{sd}}\left(\nu_{0,\mathrm{sd}} \cdot \frac{\nu_p}{30.0\mathrm{GHz}}\right)} \\
& + \boldsymbol{a}_{\mathrm{d}} \left(\frac{\nu}{\nu_{0,\mathrm{d}}}\right)^{\beta_{\mathrm{d}}+1} \frac{e^{h\nu_{0,\mathrm{d}}/kT_{\mathrm{d}}}-1}{e^{h\nu/kT_{\mathrm{d}}-1}} \\
& + \sum_{i=1}^{N_{\mathrm{co}}} \boldsymbol{a}_{\mathrm{CO}}^i \delta\left(\nu-\nu_{0,\mathrm{CO}}^i\right) \\
& + \sum_{j=1}^{N_{\mathrm{src}}} \boldsymbol{a}_{\mathrm{src}}^j \left(\frac{\nu}{\nu_{0,\mathrm{src}}}\right)^{\beta_{j,\mathrm{src}}},
\end{aligned} \tag{4.7}$$

where $x = h\nu/kT_0$, $\nu_{0,i}$ is some reference frequency for component i, and $\boldsymbol{a}_i$ is a component given in units of $\mu\mathrm{K}_{\mathrm{RJ}}$ as observed at frequency $\nu_{0,i}$. Further, $\boldsymbol{a}_{\mathrm{CO}}^i$ is the amplitude of a CO transition in the relevant frequency range, and $\boldsymbol{a}_{\mathrm{src}}^j$ the amplitude of a bright source.

The instrumental noise $\boldsymbol{n}$ is assumed to consist primarily of Gaussian correlated and white noise,

$$\boldsymbol{n} = \boldsymbol{n}_{\mathrm{corr}} + \boldsymbol{n}_{\mathrm{wn}}. \tag{4.8}$$

The white noise is dominated by thermal noise, which results from the motion of thermal electrons within the electronics of the instrument, while the correlated noise is dominated by rapid gain fluctuations.

The sky model, along with the noise, is then combined with an instrumental model to form the full data model as considered by BeyondPlanck in the first phase. We will refer to this model as the LFI data model, and it reads

$$\begin{aligned}\boldsymbol{d}_{j,t}^{\mathrm{LFI}} = g_{j,t}\left[\mathbf{P}_{tp,j}\left[\mathbf{B}_{pp',j}\left(\boldsymbol{s}_{j}^{\mathrm{sky}} + \boldsymbol{s}_{j,t}^{\mathrm{orb}}\right) + \boldsymbol{s}_{j,t}^{\mathrm{fsl}}\right] + \boldsymbol{s}_{j}^{\mathrm{mono}}\right] \\ + n_{j,t}^{\mathrm{corr}} + n_{j,t}^{\mathrm{w}},\end{aligned} \tag{4.9}$$

where $g_{j,t}$ is the instrumental gain, and $\mathbf{P}_{tp,j}$ is the pointing matrix representing the scanning strategy of *Planck*. $\mathbf{B}_{pp',j}$ is the beam convolution matrix which accounts for the fact that the signal observed by a detector does not come from a single point on the sky, but rather from a so-called "point spread function" or *beam*. In addition to the astrophysical sky signal, the data model also includes some additional signal terms, the first being $\boldsymbol{s}_{j,t}^{\mathrm{orb}}$, which is the orbital dipole signal resulting from the motion of the Earth around the Sun. Secondly, $\boldsymbol{s}_{j,t}^{\mathrm{fsl}}$ is the excess signal produced by the *Planck* satellites far sidelobes, related to the instrumental design. And finally, $\boldsymbol{s}_{j}^{\mathrm{mono}}$, which is an overall time-independent offset for detector j that accounts for the relative uncertainties in the absolute zero-level of each detector.

At a later stage, BeyondPlanck will apply their framework to other data sets, most notably to the HFI observations. Although ZLE is absent in the LFI data model, it plays a significant role in the BeyondPlanck2 data model due to its prominence at the higher frequencies. In general, the complexity of a data model will depend strongly on the experimental setup. The HFI, which observes at higher frequencies, uses different detector technology than the LFI. As such, the proposed BeyondPlanck2 data model is considerably more complex than the relatively simple LFI model. It is given by

$$\begin{aligned}\boldsymbol{d}_{j,t}^{\mathrm{HFI}} = \mathbf{U}^{\mathrm{ADC}}\left(\xi_{j,t}\right)\Big\{\mathbf{T}_{\mathrm{b}}\left(\zeta_{j}\right) g_{jt}\left[\mathbf{H}_{tp}\left(\omega_{j}\right)\mathbf{B}_{j,tp}^{4\pi}\left(\boldsymbol{s}_{j}^{\mathrm{sky}} + \boldsymbol{s}_{tp,j}^{orb}\right) + \boldsymbol{s}_{tp,j}^{\mathrm{zodi}}\right] \\ + \boldsymbol{s}_{j,t}^{\mathrm{CR}} + \boldsymbol{s}_{j,t}^{\mathrm{jump}} + \boldsymbol{s}_{j,t}^{\mathrm{4K}} + n_{j,t}^{\mathrm{corr}}\Big\} + \boldsymbol{s}^{\mathrm{ADCNL}} + n_{j,t}^{\mathrm{w}}\end{aligned} \tag{4.10}$$

where $\boldsymbol{s}_{j,t}^{\mathrm{zodi}}$ is the time-dependant ZLE contribution produced by our Zodiacal Emission module. The other new terms are: 1) a linear ADC correction operator, A; 2) a bolometer transfer function operator, B; 3) a half-wave plate operator, C; 4) a beam convolution operator, D; 5-7) sky contributions from cosmic rays, jump, and the 4K cooler; and 8) a non-linear ADC correction term. We will leave the details of these terms unelaborated, as this is outside of the scope of this thesis.

Chapter 5

Modelling Interplanetary Dust

Before we begin the development of the Zodiacal Emission module for BeyondPlanck, we need to determine how we want to model the IPD. The model we select will function as the core of the Zodiacal Emission module and must align with the objectives of BeyondPlanck, meaning that it has to be efficient and accurately reproduce the ZLE present in observational data. Further, we will require that the model is physically motivated based on the discussion in chapter 2.

There exist several different IPD models, each with varying complexity. The aforementioned DIRBE model often referred to as the K98 model, is particularly well suited to our needs, and has proved successful when applied in both the COBE and *Planck* missions. As such, we will follow in the footsteps of *Planck*, and adopt the K98 IPD model for our BeyondPlanck Zodiacal Emission module. In the following, we will provide a detailed discussion on the K98 model and elaborate on how the model was applied in the COBE and *Planck* missions to perform Zodiacal corrections.

5.1 The DIRBE model (K98)

The K98 model, described in detail in Kelsall et al. (1998) [44], is one of the earliest IPD models to consider a complex IPD distribution. In the model, the IPD is geometrically distributed over several Zodiacal components based on the findings discussed in chapter 2, whereas prior models were mainly concerned with the Zodiacal Cloud. The model includes the following components: a smooth cloud (Zodiacal cloud), three asteroidal dust bands, and a circumsolar ring, along with parametric expressions describing their three-dimensional density distribution. The ZLE is evaluated as the integral along the line-of-sight of the product of these expressions and a source function. In the following, we will introduce the model in detail.

5.1.1 Model geometry

The model geometry is defined in the heliocentric coordinate frame, which is the natural frame of reference when working with objects or distributions in the Solar System. As such, all model calculations are performed in heliocentric coordinates (X, Y, Z). The coordinate transformation for a grid point at a distance s along a line-of-sight from Earth at geocentric ecliptic coordinates (λ, β) where λ and β are the longitude and latitude respectively is given as

$$\begin{aligned} X &= R_\oplus \cos\lambda_\oplus + s\cos\beta\cos\lambda\,, \\ Y &= R_\oplus \sin\lambda_\oplus + s\cos\beta\sin\lambda\,, \\ Z &= s\sin\beta\,, \\ R &= \sqrt{X^2 + Y^2 + Z^2}\,. \end{aligned} \tag{5.1}$$

Here $R_\oplus$ is the Earth-Sun distance, and $\lambda_\oplus$ is the heliocentric longitude of Earth ($\lambda_\oplus = \pi - \lambda_\odot$). Further, it is assumed that all Zodiacal components are intrinsically time-independent and have a plane of symmetry.

The model allows each component to be off-set from the Sun (X_0, Y_0, Z_0). The component coordinates are then translated as following

$$\begin{aligned} X' &= Z - Z_0\,, \\ Y' &= Y - Y_0\,, \\ Z' &= Z - Z_0\,, \\ R_c &= \sqrt{X'^2 + Y'^2 + Z'^2}\,, \end{aligned} \tag{5.2}$$

where R_c is the euclidean norm of the component. The model also allows for a tilt of the component plane of symmetry with respect to the ecliptic so that the vertical structure of a component is given by the height above the tilted midplane, Z_c. This height is expressed as

$$Z_c = X'\sin\Omega\sin i - Y'\cos\Omega\sin i + Z'\cos i\,, \tag{5.3}$$

where i and Ω are the inclination and ascending node of the midplane, respectively.

5.1.2 The smooth cloud

The first component encountered in the model is the smooth cloud, which represents the Zodiacal Cloud. Its density is modeled as a separable equation where the radial and vertical terms are separated,

$$n_c(X, Y, Z) = n_0 R_c^{-\alpha} f(\zeta)\,. \tag{5.4}$$

Here n_0 is some density normalization, and $R_c^{-\alpha}$ is the radial component with α as a power-law parameter describing how strongly the density falls with distance from the Sun. Furthermore, $f(\zeta)$ is the vertical component with $\zeta \equiv |Z_c/R_c|$. The separation between the radial and vertical terms is physically motivated by the Poynting-Robertson drag, which is an effect that causes the orbital semi-major axes of orbiting particles such as dust grains to decay as the particles lose angular momentum to the radiation of the star. The Poynting-Robertson effect does, however, not affect the vertical distribution of the smooth cloud as the orbital inclination is unaffected by the drag. The vertical distribution $f(\zeta)$ is modeled on a form which represents a widening modified fan

$$f(\zeta) = e^{-\beta g^{\gamma}}\,, \tag{5.5}$$

where

$$g = \begin{cases} \zeta^2/2\mu & \text{for}\, \zeta < \mu\,, \\ \zeta - \mu/2 & \text{for}\, \zeta \geq \mu\,, \end{cases} \tag{5.6}$$

and β, γ, and μ are free parameters[1] determining the shape of the distribution.

5.1.3 The dust bands

The second component accounts for the asteroidal dust bands that appear in pairs about the ecliptic. The density of a band is expressed as

$$\begin{aligned} n_{Bi}(X,Y,Z) =& \frac{3n_{3Bi}}{R} \exp\left[-\left(\frac{\zeta_{Bi}}{\delta_{\zeta_{Bi}}}\right)^6\right]\left[v_{Bi} + \left(\frac{\zeta_{Bi}}{\delta_{\zeta_{Bi}}}\right)^{p_{Bi}}\right] \\ &\times \left\{1 - \exp\left[-\left(\frac{R}{\delta_{R_{Bi}}}\right)^{20}\right]\right\}\,, \end{aligned} \tag{5.7}$$

where $3n_{3Bi}$ is the density of band i at a distance of 3 AU. Further, we have $\zeta_{Bi} \equiv |z_{Bi}/R_c|$, and the free parameters p_{Bi}, $\delta_{\zeta_{Bi}}$, and v_{Bi} which determines the shape of the band, while δ_R determines the distance to which band migrates in towards the Sun. The DIRBE model includes three dust bands which appear at ecliptic latitudes of $\pm 1\overset{\circ}{.}4$, $\pm 10^\circ$, and $\pm 15^\circ$, respectively.

5.1.4 The circumsolar ring

The third and final component included in the model is the circumsolar ring, which accounts for IPD trapped in resonant orbits around the Earth. Additionally, this component also includes an enhancement in density in the region trailing the Earth, referred to as the trailing blob. The three-dimensional density of the circumsolar ring is expressed as

$$\begin{aligned} n_R(X,Y,Z) = n_{\mathrm{SR}} &\exp\left[-\frac{(R - R_{\mathrm{SR}})^2}{2\sigma_{r\mathrm{SR}}^2} - \frac{|Z_R|}{\sigma_{z\mathrm{SR}}}\right] \\ + n_{\mathrm{TB}} &\exp\left[-\frac{(R - R_{\mathrm{TB}})^2}{2\sigma_{r\mathrm{TB}}^2} - \frac{|Z_R|}{\sigma_{z\mathrm{TB}}} - \frac{(\theta - \theta_{\mathrm{TB}})^2}{2\sigma_{\theta\mathrm{TB}}^2}\right]\,, \end{aligned} \tag{5.8}$$

where the subscript SR represents the circumsolar ring, and TB the trailing blob. n_{SR} and n_{TB} are the peak densities of the ring and blob, respectively, and R_{SR} and R_{TB} are

---

[1] β should not be confused with the ecliptic latitude.

the radial locations of these peaks. The $\sigma_{\theta \mathrm{SR}}$ and $\sigma_{\theta \mathrm{TB}}$ values are free parameters that determine the scale lengths in the coordinates R, Z_R and θ. The angle θ is the angle between Earth and the (X, Y) coordinate while θ_{TB} determines the angle with which the blob trails the Earth.

5.1.5 The brightness integral

Having introduced all model components, the next step is to show how the emission from these components is calculated. The ZLE is determined through the brightness integral, which computes the modeled emission in a line-of-sight to a given celestial position p (or to a pixel when discretized) at a time t. The integral for a wavelength λ is given by

$$\begin{aligned} Z_\lambda(p,t) = &\sum_c \int n_c(X,Y,Z)\, \left[A_{c,\lambda} F_\lambda^{\odot} \Phi_\lambda(\Theta)\right. \\ &\left. + \left(1 - A_{c,\lambda}\right) E_{c,\lambda} B_\lambda(T) K_\lambda(T)\right] ds, \end{aligned} \tag{5.9}$$

where $n_c(X,Y,Z)$ is the density of component c at a coordinate (X,Y,Z) along the line-of-sight to some grid point s. The density is then scaled by a set of physically motivated parameters: $A_{c,\lambda}$ is the albedo for component c, $F_\lambda^{\odot}$ is the solar flux, $\Phi_\lambda(\Theta)$ is the phase function at the scattering angle, $E_{c,\lambda}$ is a modification factor to the emissivity which measures deviations from the blackbody function $B_\lambda(T)$ with temperature T, $K_\lambda(T)$ is some color-correction factor specific for DIRBE appropriate for B_λ. The temperature of the dust grain is assumed to vary with distance from the Sun as $T(R) = T_0 R^{\delta}$, where T_0 is the temperature at 1 AU, and δ is the fitted power-law index determining how the temperature falls with distance. The integrand is then summed over for each Zodiacal component, leaving us with the total ZLE emitted along the line-of-sight for pixel p.

5.1.6 Best-fit parameters and isodensity contours

The model parameters were obtained by fitting the model to the DIRBE data with the Levenberg-Marquardt non-linear least-squares algorithm [51], taking advantage of the observed time-variations in the ZLE. This was achieved by forcing the mean of the model for all samples to match the mean of the observed data for each individual line-of-sight. They defined the following goodness of fit

$$\chi^2 = \sum_{\lambda,p,t} \frac{1}{\sigma_\lambda^2(p,t)} \left\{\left[I_\lambda(p,t) - \langle I_\lambda(p,t)\rangle_t\right] - \left[Z_\lambda(p,t) - \langle Z_\lambda(p,t)\rangle_t\right]\right\}^2, \tag{5.10}$$

where λ is the wavelength, p is the celestial position, and t the time of observation. Furthermore, $\sigma_\lambda^2(p,t)$ is the estimated uncertainty of the observed brightness $I_\lambda(p,t)$, and $Z_\lambda(p,t)$ is the modeled brightness given through the brightness integral. The obtained best-fit parameters can be seen in Table 5.1.

Having obtained the best-fit parameters for the model components, the DIRBE team produced some very insightful isodensity contour figures. These are seen in Figure 5.1.

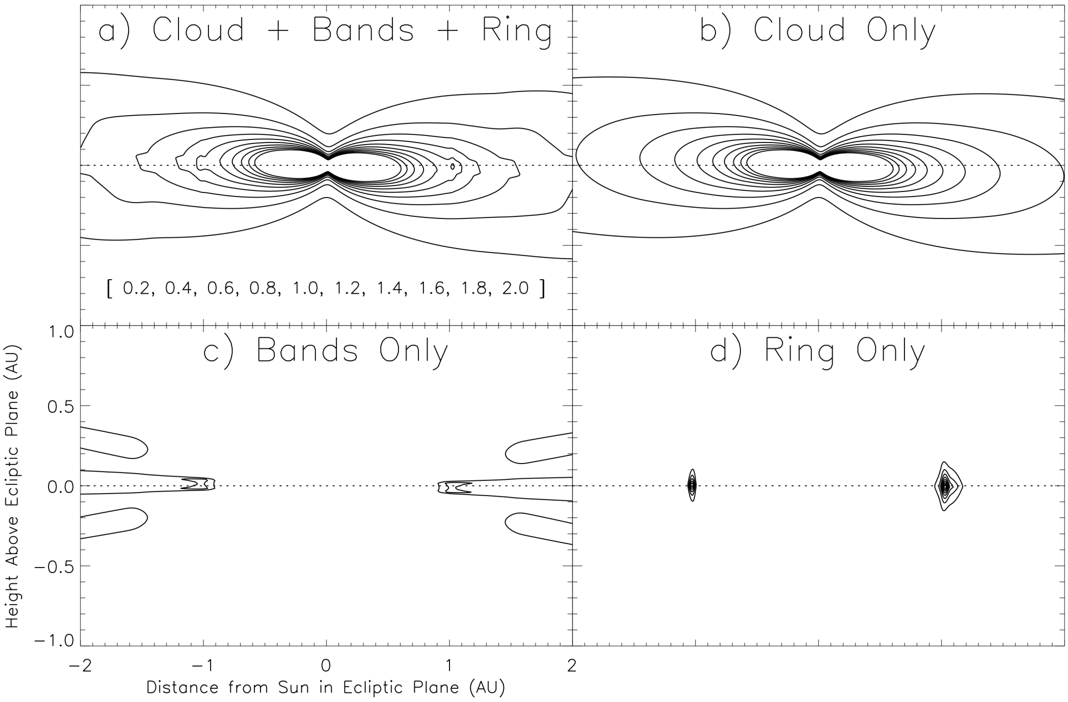

Figure 5.1: Isodensity contours for the DIRBE IPD model from Kelsall et al. (1998) [44]. The densities of each component are represented through a cross-section perpendicular to the ecliptic plane. The contours shown are: a) the total IPD density distribution; b) the smooth cloud; c) the dust bands; and d) the circumsolar ring. The contour levels used in a) and b) are listed in the brackets at the bottom of a) in units of 10^{-7} AU^{-1}. Contour levels used in c) and d) are smaller by a factor of 8.

The contour plots represent a cross-section of the density distribution of the various Zodiacal components in a plane perpendicular to the ecliptic. These figures allow us to better visualize and understand the morphology and structure of the individual Zodiacal components.

Table 5.1: Best-fit shape and density parameters in the K98 IPD model (Table 1 in Kelsall et al. (1998) [44]).

Parameter	Description	Final Value	68% Joint Confidence Uncertainty
Smooth Cloud			
n_0 [AU^{-1}]	Density at 1 AU	1.13×10^{-7}	6.4×10^{-10}
α	Radial power-law exponent	1.34	0.022
β	Vertical shape parameter	4.14	0.067
γ	Vertical power-law exponent	0.942	0.025
μ	Widening parameter	0.189	0.014
i [deg]	Inclination	2.03	0.017
Ω [deg]	Ascending node	77.7	0.6
X_0 [AU]	x offset from Sun	0.0119	0.0011
Y_0 [AU]	y offset from Sun	0.00548	0.00077
Z_0 [AU]	z offset from Sun	-0.00215	0.00043
Dust Band 1			
n_{B1} [AU^{-1}]	Density at 3 AU	5.59×10^{-10}	7.20×10^{-11}
$\delta_{\zeta_{B1}}$ [deg]	Shape parameter	8.78	Fixed
v_{B1}	Shape parameter	0.10	Fixed
p_{B1}	Shape parameter	4	Fixed
i_{B1} [deg]	Inclination	0.56	Fixed
Ω_{B1} [deg]	Ascending node	80	Fixed
$\delta_{R_{B1}}$ [AU]	Inner radial cutoff	1.5	Fixed
Dust Band 2			
n_{B2} [AU^{-1}]	Density at 3 AU	1.99×10^{-9}	1.28×10^{-10}
$\delta_{\zeta_{B2}}$ [deg]	Shape parameter	1.99	Fixed
v_{B2}	Shape parameter	0.90	Fixed
p_{B2}	Shape parameter	4	Fixed
i_{B2} [deg]	Inclination	1.2	Fixed
Ω_{B2} [deg]	Ascending node	30.3	Fixed
$\delta_{R_{B2}}$ [AU]	Inner radial cutoff	0.94	Fixed
Dust Band 3			
n_{B3} [AU^{-1}]	Density at 3 AU	1.44×10^{-10}	7.20×10^{-11}
$\delta_{\zeta_{B3}}$ [deg]	Shape parameter	15	Fixed
v_{B3}	Shape parameter	0.05	Fixed
p_{B3}	Shape parameter	4	Fixed
i_{B3} [deg]	Inclination	0.8	Fixed
Ω_{B3} [deg]	Ascending node	80	Fixed
$\delta_{R_{B3}}$ [AU]	Inner radial cutoff	1.5	Fixed
Circumsolar Ring			
n_{SR} [AU^{-1}]	Density at 1 AU	1.83×10^{-8}	1.27×10^{-9}
R_{SR} [AU]	Radius of peak density	1.03	0.00016
σ_{rSR} [AU]	Radial dispersion	0.025	Fixed
σ_{zSR} [AU]	Vertical dispersion	0.054	0.0066
i_{RB} [deg]	Inclination	0.49	0.063
Ω_{RB} [deg]	Ascending node	22.3	0.0014
Trailing Blob			
n_{TB} [AU^{-1}]	Density at 1 AU	1.9×10^{-8}	1.27×10^{-9}
R_{TB} [AU]	Radius of peak density	1.06	0.011
σ_{rTB} [AU]	Radial dispersion	0.10	0.0097
σ_{zTB} [AU]	Vertical dispersion	0.091	0.013
θ_{TB} [deg]	Longitude with respect to Earth	-10	Fixed
$\sigma_{\theta\mathrm{TB}}$ [deg]	Longitude dispersion	12.1	3.4

5.2 IPD modelling in *Planck*

The data observed by the *Planck* HFI contained significant amounts of ZLE due to the high-frequency range where the instrument operated. This is evident in the difference maps between two *Planck* sky surveys, as seen in Figure 4. This figure shows the full-sky frequency maps produced by *Planck* at 857 GHz over the sky surveys 1 and 2 in addition to the difference between the two surveys (survey 2 - survey 1). The two frequency maps look identical, but the difference map reveals clear structures along the ecliptic. The ecliptic structure is the difference in ZLE observed over the two surveys. Additional structures are also present in the difference map resulting from residual effects, such as the far sidelobes.

To correct for the ZLE contamination, the *Planck* collaboration chose to adopt the K98 IPD model. Although there had since been developments in the field of IPD research, the K98 model had proved to be successful at performing Zodiacal corrections in previous high-frequency analysis. The *Planck* implementation of the K98 IPD model is presented in *Planck* Collaboration XIV (2013) [45]. The model, as presented by *Planck*, uses a simplified notation when expressing the K98 Zodiacal components. Additionally, *Planck* discovered several differences between the K98 model components in the K98 paper and the DIRBE code implementation, which they corrected. As such, we will reiterate the Zodiacal components as presented by *Planck* in the following.

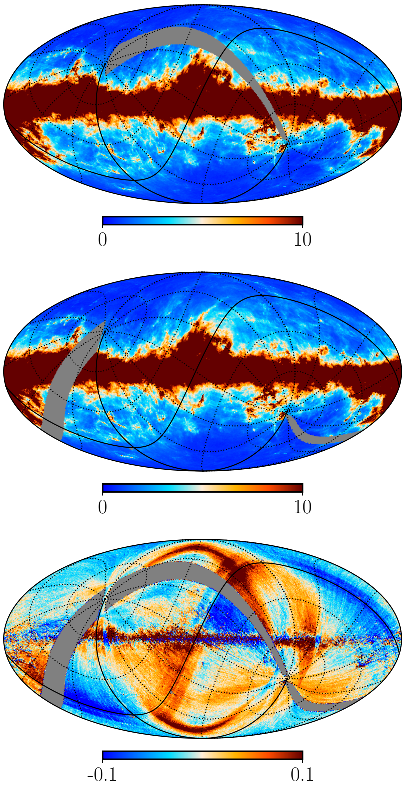

Figure 5.2: Full-sky frequency maps at 857 GHz in units of MJy/sr. Top: survey 1. Middle: survey 2. Bottom: survey 2 - survey 1.

5.2.1 The Diffuse Cloud

Planck refers to the smooth cloud as the Diffuse Cloud. The density is expressed on a simpler form where they have dropped the substitutions on the vertical term

$$n_{\mathrm{c}}(\boldsymbol{R}) = n_0 R_{\mathrm{c}}^{-\alpha} \begin{cases} e^{-\beta(\zeta^2/2\mu)^{\gamma}} & \text{if } \zeta < \mu \\ e^{-\beta(\zeta-\mu/2)^{\gamma}} & \text{if } \zeta \geq \mu, \end{cases} \tag{5.11}$$

where $\boldsymbol{R}$ is a heliocentric coordinate.

5.2.2 The Dust Bands

Planck presents the Dust Band densities with a shorter notation where the density of band B is given by

$$n_B(\boldsymbol{R}) = \frac{3N_0}{R} e^{-(\zeta/\delta_\zeta)^6} \left(1 + \frac{(\zeta/\delta_\zeta)^p}{v_B}\right) \left(1 - e^{-(R/\delta_R)^{20}}\right). \tag{5.12}$$

This expression differs from the K98 equivalent by a factor $1/v_B$. *Planck* made the following comment on the matter: "Note that Eq. 5 matches the code used for the zodiacal model (which can be found on the LAMBDA website), but that there is a factor of $1/v_B$ difference between Eqn. 5 and Eqn. 8 of K98" (*Planck* XIV 2013, p. 6). The expression for the Dust Bands in the DIRBE code used to perform the calculations did not match the expression in the K98 article. As such, *Planck* decided to proceed with the expression used in the code. Additionally, the emissivities of each Dust Band were assumed to be equal in K98. *Planck* relaxed this assumption and allowed the emissivities of each band to differ from one another.

5.2.3 The Circumsolar Ring and the Earth-trailing Feature

Planck separated the density expressions of the Circumsolar Ring and the Earth-trailing blob, which *Planck* refers to as the Earth-trailing Feature, into two separate components. The density of the Circumsolar Ring denoted by SR is given by

$$n_{\mathrm{SR}}(\boldsymbol{R}) = n_{\mathrm{SR}} \cdot e^{-(R-R_{\mathrm{SR}})^2/\sigma^2_{\mathrm{rsR}} - |Z_R|/\sigma_{\mathrm{zSR}}}, \tag{5.13}$$

while the density of the Earth-trailing Feature, denoted by TF, is given by

$$n_{\mathrm{TB}}(\boldsymbol{R}) = n_{\mathrm{TB}} \cdot e^{-(R-R_{\mathrm{TB}})^2/\sigma^2_{\mathrm{rTB}} - |Z_R|/\sigma_{\mathrm{zTB}} - (\theta-\theta_{\mathrm{TB}})^2/\sigma^2_{\theta\mathrm{TB}}}. \tag{5.14}$$

Similar to the case with the Dust Bands, *Planck* found the expression in the code and the article to differ by a factor of 2 in the denominator. As a result, they decided to remove this factor from the final expression.

5.2.4 Integrated Zodiacal emission

The integrated Zodiacal emission, referred to as the brightness integral in K98, is approached from a more practical aspect in the *Planck* implementation. *Planck* assumed that the ZLE from a component x is simply given by the product of its density multiplied with the blackbody function and an emissivity factor. The integral of the ZLE along a line-of-sight is then

$$I_x(\nu) = \epsilon_x \int d\boldsymbol{R} \cdot n_x(\boldsymbol{R}) \cdot B(\nu, T(\boldsymbol{R})), \tag{5.15}$$

where ϵ_x and $n_x(\boldsymbol{R})$ are the emissivity and density of component x, respectively. Further, $B(\nu, T(\boldsymbol{R}))$ represents the *Planck* function 3.2) at a frequency ν for a temperature

$T(\boldsymbol{R})$ determined by the distance from the Sun. By incorporating all the physical parameters used in the brightness integral of K98 into a single emissivity parameter, *Planck* heavily simplifies the emission calculations. This simplification is, however, at the expense of our physical understanding of the emission, which is now drastically reduced. The choice to simplify was sensible, considering that the primary objective of *Planck* was to study the CMB, and not the IPD.

Planck presented a set of ZLE templates (Figure 4 in the paper) showing the estimated ZLE. These were computed at 857 GHz with unit emissivity ($\epsilon_x = 1$). The templates, however, were shown with relative amplitudes making it difficult to study the true structure of each component. Fortunately, these templates can also be found on the ESA wiki webpage [52], where they are presented with absolute amplitudes. These templates can be seen in Figure 5.3, where the columns show the estimated ZLE in units of MJy/sr over *Planck* survey 1 (left), survey 2 (middle), and the difference between survey 2 and survey 1 (right). The rows show from top to bottom: 1) The Diffuse Cloud; 2) Dust Band 1; 3) Dust Band 2; 4) Dust Band 3; 5) the Circumsolar Ring; and 6) the Earth-Trailing Feature. The difference map of the Diffuse Cloud component, which is the dominating Zodiacal component at this frequency, is seen to match the structure of the ZLE in Figure 5.2.

Planck also presented the Zodiacal correction maps calculated during their 2013 analysis for each HFI frequency band. These are maps uncorrected for ZLE minus maps corrected for ZLE and can be seen in Figure 5.4. These correction maps are not the ZLE templates representing $\boldsymbol{s}_{\mathrm{zodi}}$ in the *Planck* data model, as these maps also contain the far sidelobes corrections performed alongside the Zodiacal corrections.

5.2.5 Zodiacal emissivities

The emissivities ϵ_x are obtained by taking advantage of the unique time-dependence of the ZLE. If we assume that the ZLE is the only time-varying sky component over two sky surveys, then in theory, the survey difference map should simply be the ZLE difference map. We can model the survey difference map at pixel p, D_p as follows

$$D_p = \sum_t \left(\epsilon_{2,t} T_{2,t,p} - \epsilon_{1,t} T_{1,t,p}\right) + \text{constant}, \tag{5.16}$$

where $\epsilon_{i,t}$ is the emissivity fits for template t for survey i, and $T_{i,t,p}$ is the value of the corresponding template t at pixel p. As we saw in Figure 5.2, there are additional sources of contamination present in a survey difference map, which also has to be accounted for if the emissivities are to accurately be estimated. As such, *Planck* included templates of the far sidelobes in addition to the Zodiacal component templates when performing the fit. The emissivities were then acquired by minimizing the following

$$\chi^2 = \sum_p \left(\Delta_p - D_p\right), \tag{5.17}$$

where Δ_p is a constant to which *Planck* is not sensitive.

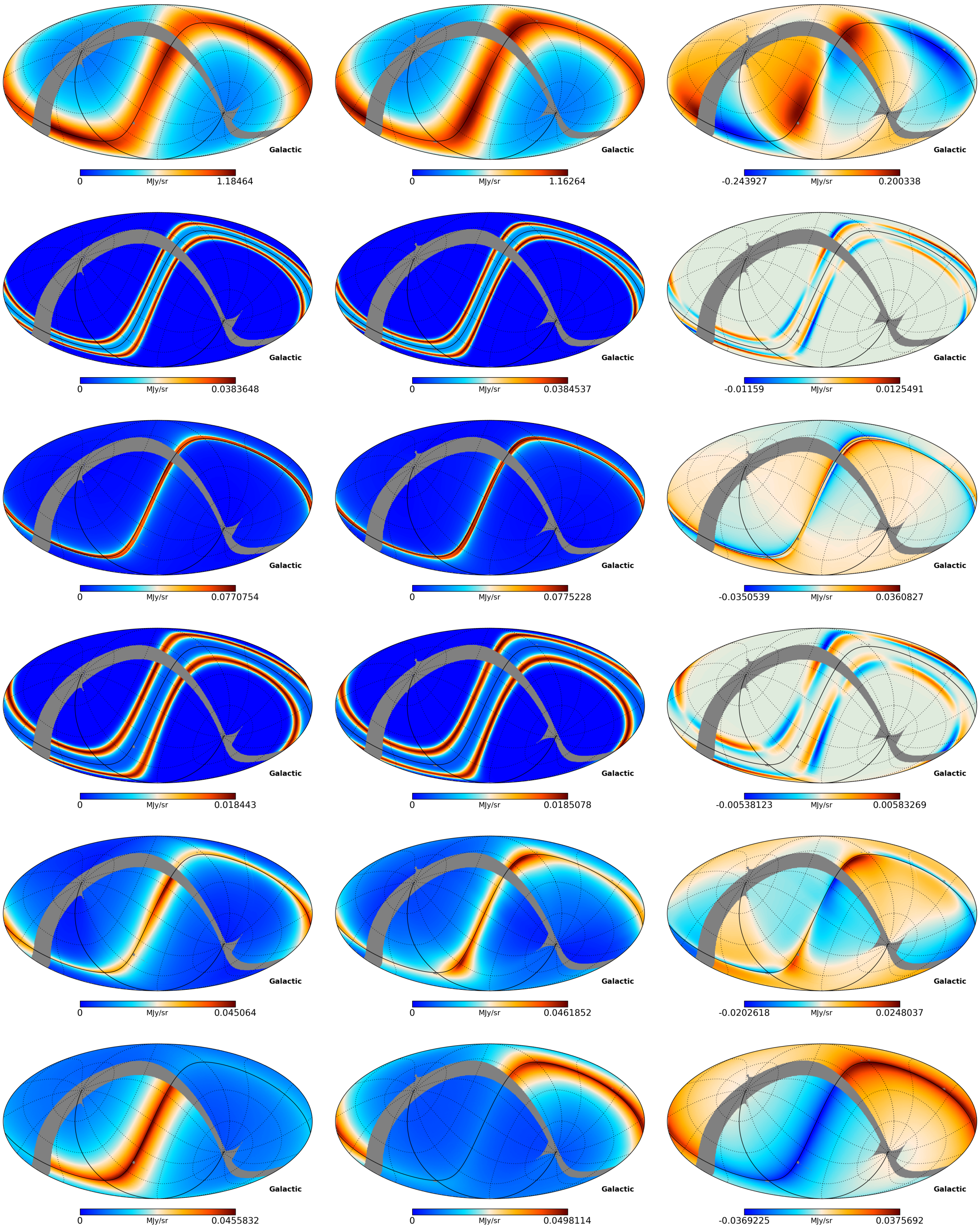

Figure 5.3: Estimated ZLE maps of each Zodiacal component at 857 GHz in units of MJ/sr from the *Planck* 2013 analysis [52]. The columns show from left to right: 1) the ZLE over *Planck* survey 1; 2) survey 2; and 3) the difference maps between survey 2 and survey 1. The rows show from top to bottom: 1) The Diffuse Cloud; 2) Dust Band 1; 3) Dust Band 2; 4) Dust Band 3; 5) the Circumsolar Ring; and 6) the Earth-Trailing Feature.

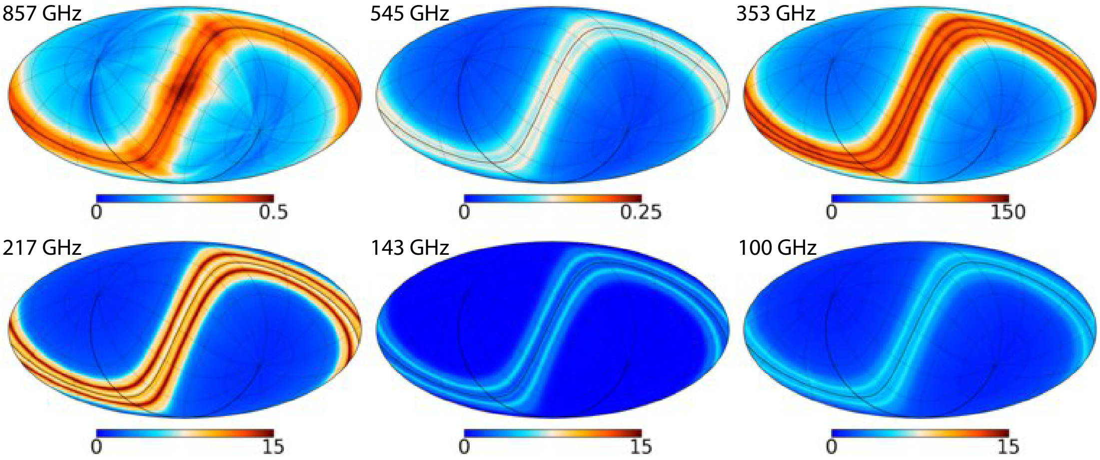

Figure 5.4: Difference maps (maps uncorrected for ZLE minus maps corrected for ZLE) showing the Zodiacal corrections calculated in the *Planck* 2013 analysis. Units are MJy/sr for the 857GHz and 545GHz maps, and μK_{CMB} for the other frequencies.

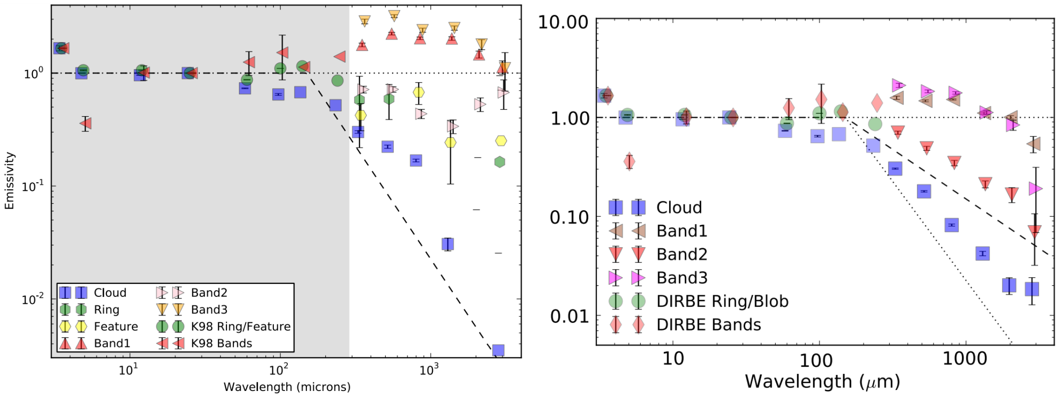

Figure 5.5: Emissivity fits of the Zodiacal component from the *Planck* 2013 analysis (left) and 2018 analysis (right). Wavelenghts smaller than 300μm (shaded in gray in the 2013 plot) represents the emissivites obtained by COBE/DIRBE. The lines mark emissivities that are unity at wavelengths less than 250μm, but proportional to λ^{-2}, λ^{-1}, and λ^0 at longer wavelengths. Note that negative fits do not appear in the 2013 log-log plot.

Table 5.2: Frequency-averaged emissivities for the Zodiacal components from the *Planck* 2013, 2015, and 2018 results.

ν [GHz]	Cloud	Band 1	Band 2	Band 3	Ring	Feature
			2013 emissivities			
857	0.301 ± 0.008	1.777 ± 0.066	0.716 ± 0.049	2.870 ± 0.137	0.578 ± 0.359	0.423 ± 0.114
545	0.223 ± 0.007	2.235 ± 0.059	0.718 ± 0.041	3.193 ± 0.097	0.591 ± 0.203	−0.182 ± 0.061
353	0.168 ± 0.005	2.035 ± 0.053	0.436 ± 0.041	2.400 ± 0.100	−0.211 ± 0.085	0.676 ± 0.149
217	0.031 ± 0.004	2.024 ± 0.072	0.338 ± 0.047	2.507 ± 0.109	−0.185 ± 0.143	0.243 ± 0.139
143	−0.014 ± 0.010	1.463 ± 0.103	0.530 ± 0.073	1.794 ± 0.184	−0.252 ± 0.314	−0.002 ± 0.180
100	0.003 ± 0.022	1.129 ± 0.154	0.674 ± 0.197	1.106 ± 0.413	0.163 ± 0.784	0.252 ± 0.455
			2015 emissivities			
857	0.256 ± 0.007	2.06 ± 0.19	0.85 ± 0.05	3.37 ± 0.38		
545	0.167 ± 0.002	1.74 ± 0.11	0.54 ± 0.03	2.54 ± 0.18		
353	0.106 ± 0.003	1.58 ± 0.07	0.39 ± 0.02	1.88 ± 0.14		
217	0.051 ± 0.006	1.30 ± 0.07	0.15 ± 0.02	1.27 ± 0.14		
143	0.022 ± 0.010	1.23 ± 0.10	0.15 ± 0.04	1.16 ± 0.22		
100	0.012 ± 0.005	1.02 ± 0.16	0.08 ± 0.03	0.72 ± 0.27		
			2018 emissivities			
857	0.304 ± 0.004	1.58 ± 0.06	0.70 ± 0.03	2.11 ± 0.10		
545	0.179 ± 0.003	1.47 ± 0.03	0.49 ± 0.02	1.84 ± 0.06		
353	0.082 ± 0.002	1.52 ± 0.02	0.35 ± 0.02	1.77 ± 0.05		
217	0.042 ± 0.002	1.11 ± 0.03	0.21 ± 0.02	1.12 ± 0.05		
143	0.020 ± 0.004	1.00 ± 0.04	0.17 ± 0.03	0.84 ± 0.10		
100	0.018 ± 0.006	0.54 ± 0.10	0.07 ± 0.04	0.19 ± 0.12		

The emissivity fits obtained by *Planck* in the 2013 analysis were suspicious. The emissivities generally exhibited large uncertainties, and some of the fits were found to be negative. Most notably were the emissivity fits for the Circumsolar Ring and the Earth-trailing Feature which were inconsistent from frequency to frequency. As such, in the 2015 *Planck* analysis [53], *Planck* performed a new emissivity fit where they opted to not include the Circumsolar Ring and the Earth-trailing Feature components. These fits were further improved upon with the 2018 results [37] through general improvements to the HFI data. The emissivity fits for the 2013, 2015 and 2018 *Planck* results can be seen in Figure 5.5. The detector-averaged numerical values of the emissivities are tabulated in Table 5.2.

Chapter 6

The BeyondPlanck Zodiacal Emission Module

Having finished our discussion on IPD modelling, it is time to introduce the BeyondPlanck Zodiacal Emission module. For this, we adopt the parametric K98 IPD model as implemented by *Planck*. The main concern of the implementation is to translate the model to the time-ordered domain. The Zodiacal Emission module will need to be able to estimate the ZLE by constructing a line-of-sight that matches the pointing of the *Planck* instruments at the time of observation. Additionally, computational efficiency becomes increasingly important in the time-ordered domain, particularly in a dynamic IPD model based on line-of-sight integration, where each additional point evaluated along the line-of-sight effectively acts as a multiplier to the computation time.

In the coming sections, we review the structure of our BeyondPlanck Zodiacal Emission module and outline the role of the module in `Commander`. Further, we provide a detailed explanation of how a line-of-sight is drawn, before concluding the chapter with a brief discussion on numerical integration.

6.1 Module overview

The BeyondPlanck machinery `Commander` operates by reading in blocks of time-ordered data in succession. One such block represents the data observed by *Planck* during a single operational hour, which typically contains the signal from $n_{\mathrm{TOD}} \approx 80000-120000$ observed celestial positions. Additionally, each block of time-ordered data contains some auxiliary data, such as satellite position and velocity. The Zodiacal emission module is part of the time-ordered component separation loop in `Commander` and has the following objective: for every block of time-ordered data read by `Commander`, return the expected ZLE signal matching each observed celestial position. The Zodiacal emission module consists of two main methods:

1. A method that initializes the module. This method is called upon only once before entering the time-ordered component separation loop in `Commander`. The

main function of the method is to initialize the IPD model components and to pre-compute frequently used quantities. Most notably of these quantities are the heliocentric ecliptic coordinates corresponding to the observed galactic coordinates, which are computed through the HEALPix framework and later used in the line-of-sight calculations.

2. A method that estimates the ZLE in the time-ordered data based on the IPD model. This method, which is called with each new block of time-ordered data, iterates over all celestial positions (pixels) in the time-ordered data block. For each pixel, a discrete line-of-sight is drawn from *Planck*'s location to a distance of R_{LOS} towards each pixel. For each point along this line-of-sight, the following quantities are calculated: 1) the density of each Zodiacal component at the heliocentric ecliptic coordinate (x,y,z), corresponding to the coordinate of the discrete point; and 2) the *Planck* function that represents the radiation emitted by the IPD, determined by the frequency ν and the temperature T at the coordinates (x,y,z). The line-of-sight is then numerically integrated over to obtain the total ZLE observed in the given pixel. This process is repeated for every uniquely observed pixel and the result stored in a signal array.

Most of the pixels contained in a given block of time-ordered data are observed multiple times in the same block due to *Planck*'s scanning strategy. We can exploit this to significantly increase computational efficiency. The satellite position is assumed to be constant over each chunk, meaning that we only need to calculate the ZLE for each unique pixel once per block and tabulate it. The next time the same pixel is hit, we simply look up the tabulated value, and use this to increment the total ZLE observed in that pixel. Once the module has iterated over a full set of data, the signal array containing the calculated ZLE is passed to the mapmaking of `Commander`, where it is appropriately weighted and normalized into a sky map.

6.2 Determining the line-of-sight

Constructing an accurate line-of-sight is a critical aspect of the ZLE evaluation. It might be tempting to assume that a radial vector $\boldsymbol{x}_{\mathrm{max}}$ pointing from the Sun towards the coordinates of a pixel observed by *Planck* would make for a sufficient line-of-sight. After all, orbital variations can usually be neglected when working with cosmological data assumed to be emitted at infinity. However, we recall from our discussion on the IPD that a line-of-sight towards a celestial position does observe different amounts of ZLE depending on the orbital position of the observer, as illustrated in Figure 3.10.

To properly capture the time-variation in the ZLE, a vector $\boldsymbol{x}_{\mathrm{LOS}}$ must be drawn directly from the location of the observer (x_0, y_0, z_0), represented by the vector $\boldsymbol{x}_0$, in the direction of the observed pixel. The length of this vector will vary for each line-of-sight as it has to end at a point along a circle of radius R_{max} centered on the Sun, which is the maximum integration length considered. We call this variable-length R_{LOS}. Since the celestial position observed by an observer, such as *Planck*, is at infinity, the

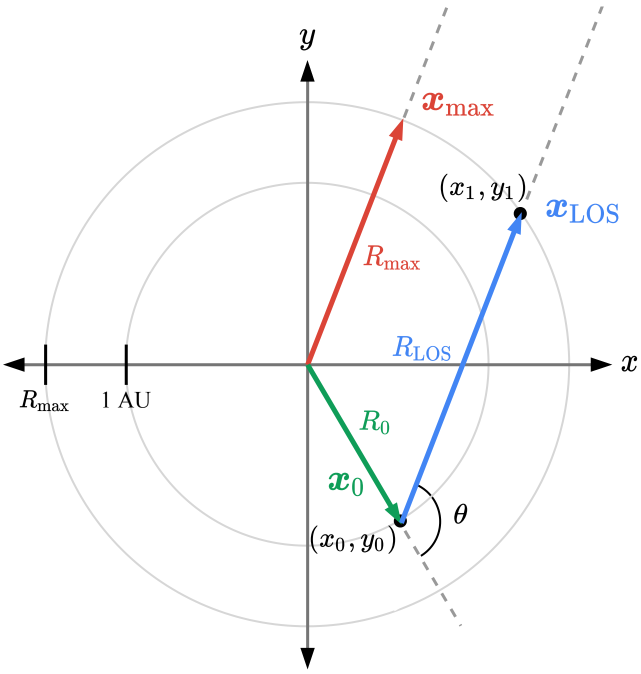

Figure 6.1: Vector diagram illustrating the geometry in the LOS problem. $\boldsymbol{x}_{\max}$ is the vector pointing from the heliocentric origin towards a celestial position at infinity with length $R_{\max}$, $\boldsymbol{x}_0$ is the vector pointing to the observer from the heliocentric origin with length R_0, and $\boldsymbol{x}_{\mathrm{LOS}}$ is the LOS vector with length R_{LOS}. The angle θ is the angle between $\boldsymbol{x}_0$ and $\boldsymbol{x}_{\max}$, which is equivalent to the angle between $\boldsymbol{x}_0$ and $\boldsymbol{x}_{\mathrm{LOS}}$ as $\boldsymbol{x}_{\max}$ and $\boldsymbol{x}_{\mathrm{LOS}}$ are parallel.

vector pointing towards this position would have to be parallel with a vector pointing from the Sun to the same pixel. We can, therefore, use the unit vectors of $\boldsymbol{x}_{\max}$, $(\hat{\boldsymbol{x}}_{\max}, \hat{\boldsymbol{y}}_{\max}, \hat{\boldsymbol{z}}_{\max})$ as our pointing vectors when drawing the line-of-sight. Using the above information, we can determine the end-coordinates of the line-of-sight to be

$$\begin{aligned} x_1 &= x_0 + R_{\mathrm{LOS}} \hat{\boldsymbol{x}}_{\max}, \\ y_1 &= y_0 + R_{\mathrm{LOS}} \hat{\boldsymbol{y}}_{\max}, \\ z_1 &= z_0 + R_{\mathrm{LOS}} \hat{\boldsymbol{z}}_{\max}. \end{aligned} \tag{6.1}$$

Now that we have both the coordinates of the observer and the endpoint along the line-of-sight, we can construct a line-of-sight with N_{LOS} discrete points which accurately represent the satellite pointing at the time of observation. The line-of-sight problem is shown in the vector diagram seen in Figure 6.1. The illustrated approach is general and should apply to any cosmological observer. This means that any time-ordered data set for which these vectors can be found is eligible for ZLE estimation in BeyondPlanck.

The only unknown quantity in the line-of-sight problem is the variable-length R_{LOS}, which is not trivial to find. We can calculate this length by considering the following circle identity,

$$|\boldsymbol{x}_{\max}| = |\boldsymbol{x}_0 + \boldsymbol{x}_{\mathrm{LOS}}|, \tag{6.2}$$

which says that the length of the two added vectors $\boldsymbol{x}_0 + \boldsymbol{x}_{\mathrm{LOS}}$ equal the length of $\boldsymbol{x}_{\max}$ as both these vectors are the radius of some circle with radius $R_{\max}$. By writing out the magnitude at the right-hand-side we get the following expression

$$|\boldsymbol{x}_{\max}| = \sqrt{|\boldsymbol{x}_0|^2 + |\boldsymbol{x}_{\mathrm{LOS}}|^2 + 2|\boldsymbol{x}_0||\boldsymbol{x}_{\mathrm{LOS}}|\cos\theta}, \tag{6.3}$$

where θ is the angle between $\boldsymbol{x}_0$ and $\boldsymbol{x}_{\mathrm{LOS}}$. Since $\boldsymbol{x}_{\mathrm{LOS}}$ is parallel with $\boldsymbol{x}_{\max}$, θ is also the angle between $\boldsymbol{x}_{\max}$ and $\boldsymbol{x}_0$. Furthermore, we rewrite expression 6.3 in terms of the actual lengths ($|\boldsymbol{x}_0| = R_0$, $|\boldsymbol{x}_{\max}| = R_{\max}$, and $|\boldsymbol{x}_{\mathrm{LOS}}| = R_{\mathrm{LOS}}$) so that

$$R_{\max} = \sqrt{R_0^2 + R_{\mathrm{LOS}}^2 + 2R_0R_{\mathrm{LOS}}\cos\theta}. \tag{6.4}$$

Squaring both sides of the equation allows us to reformulate the identity as a quadratic equation

$$R_{\mathrm{LOS}}^2 + 2R_0R_{\mathrm{LOS}}\cos\theta + R_0^2 - R_{\max}^2 = 0, \tag{6.5}$$

which results in the two solutions for the line-of-sight distance

$$R_{\mathrm{LOS}} = -R_0\cos\theta \pm \sqrt{R_0^2\cos^2\theta - R_0^2 + R_{\max}^2}. \tag{6.6}$$

We are only interested in the positive solution as the negative solution represents a line to the opposite side of the circle of radius $R_{\max}$. Note that the length of any LOS observed by an observer is uniquely given by the angle θ.

6.3 Numerical integration

As stressed several times, the transition to the time-ordered domain requires that the Zodiacal Emission module is efficient in its calculations. Integrating along a line-of-sight is typically an expensive operation, and it is, therefore, important that we pick the appropriate method of quadrature. We are mainly looking for a method with a minimal of integrand evaluations per step along the line-of-sight, meaning that we are prepared to lose some precision on the estimated signal. We will attempt to justify this by arguing that the K98 IPD model is already an approximation, and this loss of precision could be accounted for by a new set of emissivity fits performed by BeyondPlanck at later stages.

There exists a wide range of numerical integration techniques that one can choose between depending on the specific problem one wants to solve. In our case, we are working with a function tabulated at equally spaced intervals along a line-of-sight. The most straightforward integration technique for such a problem, and also the fastest, is the Newton-Cotes formulas. The two methods we will consider for the BeyondPlanck ZLE module are the 2- and 3- point formulas called the trapezoidal rule, and the Simpson's rule, respectively, which we will briefly introduce in the following.

In general, any continuous function $f(x)$ over an interval $[a, b]$ can be divided into N equally spaced subintervals with length $\Delta x = (b - a)/N$, with endpoints at $x_0, x_1, x_2, \ldots, x_N$. The trapezoidal rule is an approximation to the definite integral

$$\int_a^b f(x)dx \approx \frac{\Delta x}{2}(f(x_0) + 2f(x_1) + 2f(x_2) + \cdots + 2f(x_{n-1}) + f(x_n)), \tag{6.7}$$

which evaluates the area under a curve by dividing the total area into trapezoids. A more accurate approximation to the definite integral is given by Simpson's rule

$$\begin{aligned} \int_a^b f(x)dx \approx \frac{\Delta x}{3}(f(x_0) + 4f(x_1) + 2f(x_2) + 4f(x_3) + 2f(x_4) + \\ \cdots + 4f(x_{n-1}) + f(x_n)). \end{aligned} \tag{6.8}$$

which uses piecewise quadratic functions to approximate the area under the curve. Note that Simpson's rule requires the interval $[a, b]$ to be divided into an even number of N subintervals.

To settle on a standard method for the Zodiacal Emission module, we performed a survey where we compared results with both methods while varying the number of subintervals N. The outcome of this survey will be presented in chapter 7, together with our results.

Part III

Results

Chapter 7

Interplanetary Dust Distribution and Zodiacal Light Emission

Having finished our discussion on the BeyondPlanck Zodiacal Emission module, we conclude the methods part of the thesis. We are just about ready to present our results, but before we put the Zodiacal Emission module to the test, we will perform a study on the K98 Zodiacal components. The density distribution of the Zodiacal components is the primary model attribute when it comes to describing the structure observed in ZLE maps. It is, therefore, important that we understand the Zodiacal components in the IPD model to the best of our abilities so that we know what to expect from the coming results and how to interpret them.

Before we present our results from the IPD model, we would like to stress that we are working with a purely parametric description of the Zodiacal components. The K98 IPD model was developed for component separation with the primary objective of reproducing the apparent time variations over the sky, with stable residuals over all frequencies. This means that the structure we see in the coming results is not necessarily the true physical geometry of the IPD distribution, but rather a representation of the IPD as best described by the data observed by the DIRBE instrument. The authors behind had the following to say about the model: "It is, in fact, impossible to determine a unique model from any set of data taken from within the IPD cloud. Only a mission flying well beyond the orbit of Jupiter could gather data permitting a unique solution" (Kelsall et al. 1998, p.72). This must be kept in mind when we in the coming attempt to interpret the results from a physical point of view.

7.1 A study on the K98 Zodiacal components

We begin our study of the Zodiacal components by initializing a three-dimensional Cartesian grid with n^3 cells to represent the section of the Solar System relevant for our analysis. Each cell is assigned a coordinate (x, y, z) in the heliocentric reference frame. We can then compute the amount of IPD contained in a given cell by using the density expressions of each respective Zodiacal component. The grid is then effectively

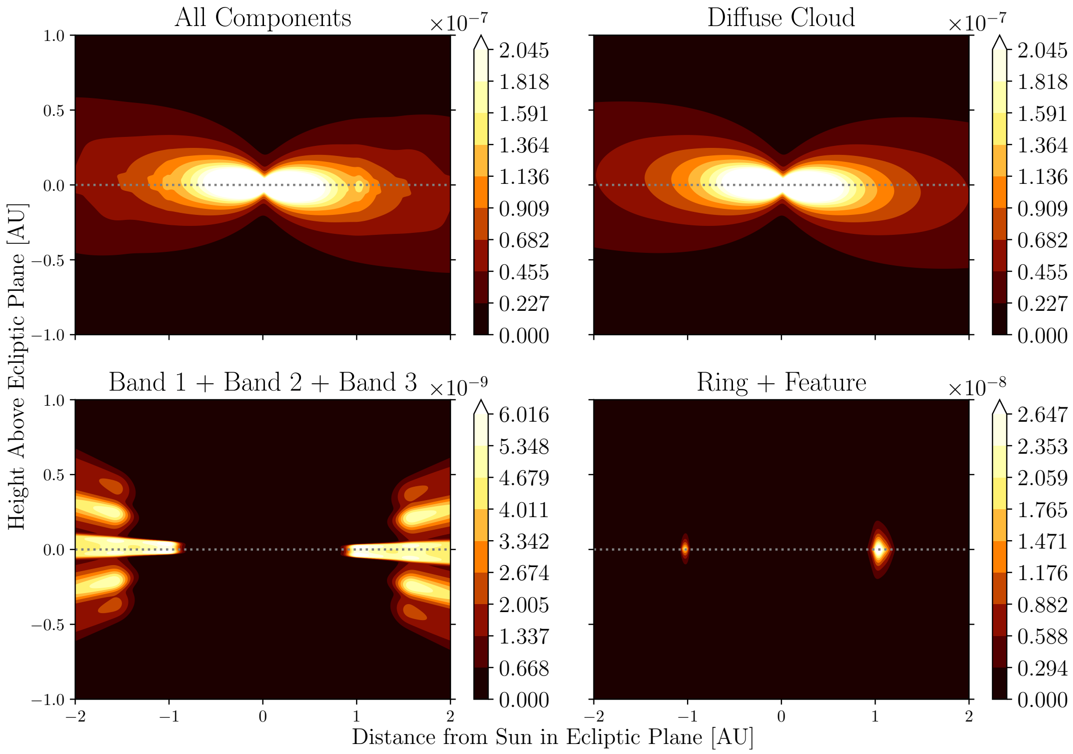

Figure 7.1: Isodensity contour reproduction of Figure 5.1. The contours are illustrating the spatial density distribution of the various Zodiacal components in a cross-sectional slice perpendicular to the ecliptic plane. All subfigures share y- and x-axis. From left to right, in the top row: 1) the combined density of all included Zodiacal components; and 2) the Diffuse Cloud. In the bottom row: 1) all three Dust Bands; and 2) the Circumsolar Ring and the Earth-trailing Feature together. The color bar represents the density values of the contour levels. The gray dotted line represents the ecliptic plane and is included to show the tilt of the component with respect to the Ecliptic.

representing a three-dimensional scalar field of the IPD density. When deciding how we wanted to visually represent this scalar field, we found no satisfactory three-dimensional visualization tools that could illustrate the complete geometric extent of our model. However, due to the existing symmetries in the way the IPD is distributed, the geometry of most Zodiacal components would be fully illustrated through a cross-section of the grid in the xz- or yz-plane. We, therefore, follow the method used by K98, which is to illustrate the geometry of each Zodiacal component through cross-sectional isodensity contour figures. We found it sufficient to represent the Diffuse Cloud, Dust Bands, and the Circumsolar Ring through a single cross-section through the Ecliptic in the xz-plane. The Earth-trailing Feature is the only component in the model without a plane of symmetry. As such, we have included an additional overhead plot with a cross-section of the xy-plane to illustrate this asymmetry. We will discuss these contour figures shortly.

To make sure that the Zodiacal components are correctly implemented, we reproduce the K98 isodensity contour figure (Figure 4 in K98 and Figure 5.1 in chapter 5) to compare results. The only difference between our IPD models are some minor factors in the Zodiacal component expressions as discussed in sections 5.2.2 and 5.2.3, and as such, we expect our results to be mostly identical to those of K98. Our reproduction is seen in Figure 7.1. These contour plots are produced using two-dimensional cross-sections of the grid with ranges [-2, 2] AU in the x-plane, and [-1, 1] AU in the z-plane. Our contour plots are convincingly similar to those of K98, with the only apparent deviation being the Dust Bands. Only a total of two Dust Bands are present in K98 subfigure c), despite the model including three individual bands. This is likely the result of the contour levels selected by K98 being too weak to display the third Dust Band. Dust Band 3 is significantly weaker in terms of density when compared to Dust Bands 1 and 2, which is apparent in our results. Nevertheless, we conclude that our IPD model is correctly implemented and proceed by analysing the Zodiacal components further individually.

7.1.1 The Diffuse Cloud

The Diffuse Cloud is seen in the left-most subfigure of the first row in Figure 7.2. It is plotted in the range [-6, 6] AU in the x-plane, and [-2, 2] AU in the z-plane. These ranges were selected to more accurately illustrate the full extent of the component in the relevant BeyondPlanck integration range. The observed results of the Diffuse Cloud are consistent with our expectations and with the results of K98. The Diffuse Cloud is highly concentrated along the Ecliptic, specifically along its plane of symmetry tilted by 2° with respect to the Ecliptic. The component is distributed in a fan-like shape with densities increasing exponentially as one approaches the Sun. We recall from chapter 2 that there is a physical radial limit to how close dust particles can get to the Sun before being burnt up or pushed out through solar winds. The density expression for the Diffuse Cloud does not account for this cut-off. This is intentionally left out of the model as observational experiments typically do not observe the inner-most parts of the Solar System, meaning that no integrated LOS ever includes these regions with non-physical densities.

7.1.2 The Dust Bands

The Dust Bands are shown in the right-most subfigure in the top row and both subfigures in the middle row of figure 7.2. We have plotted the bands with individual contour levels to aim the attention at their structures and not their relative strengths. After all, high density does not necessarily translate into strong observed emission due to factors such as emissivity scaling. All three Dust Bands appear in pairs at ecliptic latitudes of approximately ±9° for Band 1, ±2° for Band 2, and ±15° for Band 3. We see that Dust Band 2 extends much further towards the Sun than the other two bands with a cut-off radius at 0.94 AU, which puts the peak density of the component

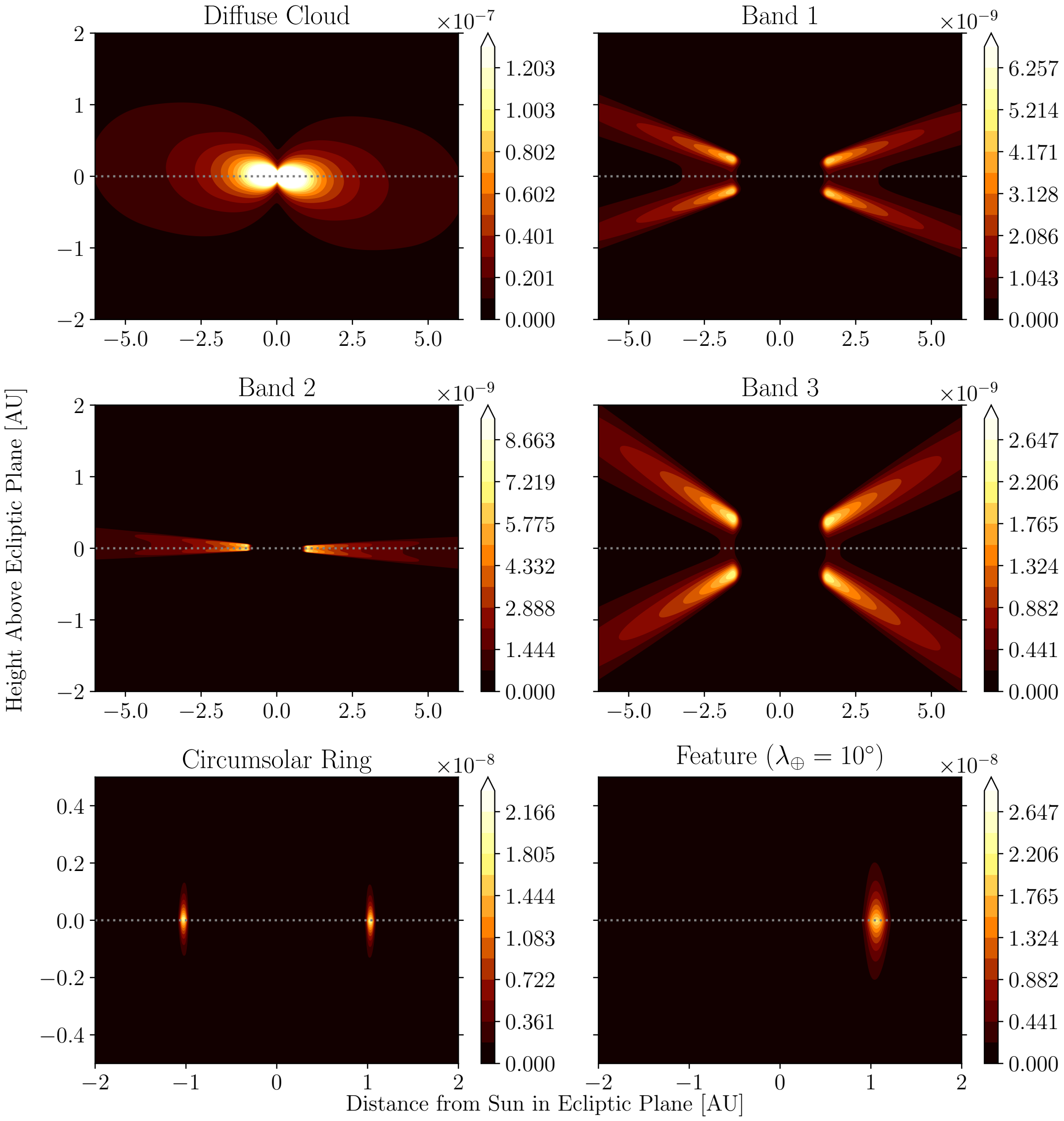

Figure 7.2: Isodensity contours illustrating the spatial density distribution of the six K98 Zodiacal components in a cross-sectional slice perpendicular to the ecliptic plane. From left to right, in the top row: 1) the Diffuse Cloud; and 2) Dust Band 1. In the middle row: 1) Dust Band 2; and 2) Dust Band 3. In the bottom row: 1) the Circumsolar Ring; and 2) the Earth-trailing Feature. The Earth-trailing Feature is computed while setting the longitude of Earth to $\lambda_\oplus = 10°$, which puts the feature directly in the cross-section at $x = 1.06$ AU. The color bar represents the density values of the contour levels. The gray dotted line represents the ecliptic plane and is included to show the inclined plane of each component with respect to the Ecliptic. Rows share a common y-axis.

within Earth's orbit. Dust Bands 2 and 3, on the other hand, share the same cut-off radius of 1.5 AU. Despite the proximity to Earth, the density of Dust Band 2 is very weak compared to that of the Diffuse Cloud and even to the Circumsolar Ring and Earth-trailing Feature. It is only when one looks directly along the Dust Band that one observes significant emission from the accumulated density. This is true for all three Dust Bands. Additionally, Dust Band 2 appears as the strongest of the three bands

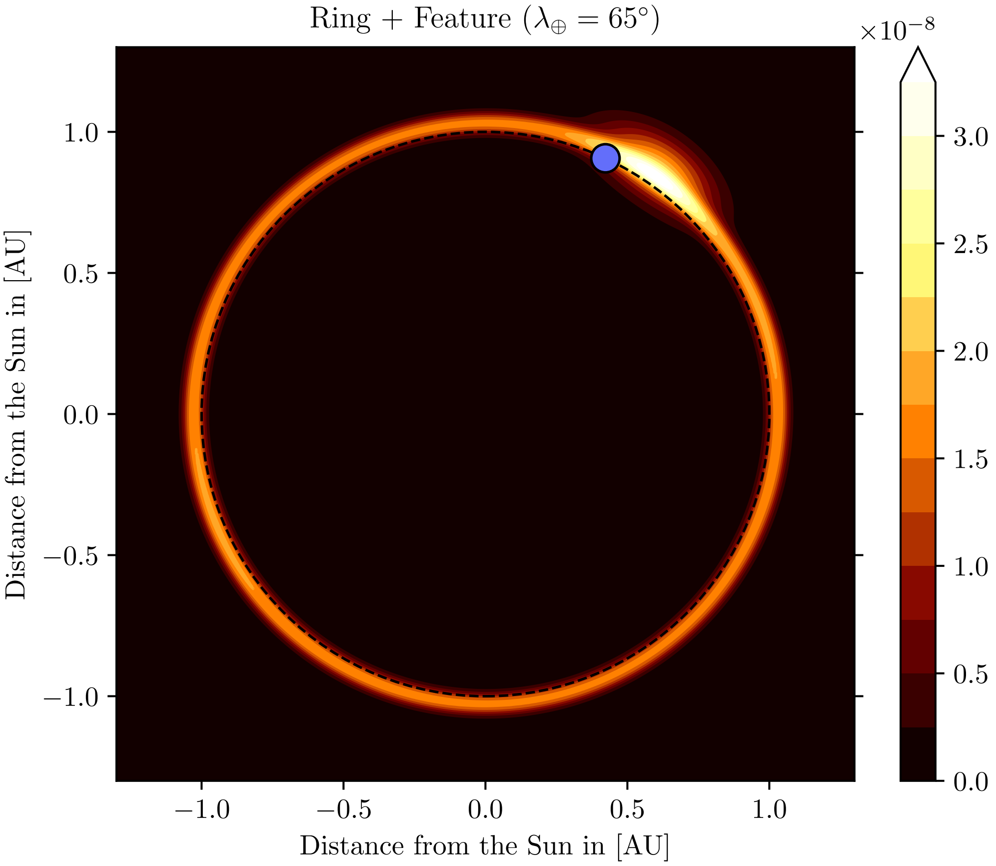

Figure 7.3: Isodensity contour of the Circumsolar Ring and the Earth-trailing Feature in a cross-sectional slice along the ecliptic plane. The Earth-trailing Feature is computed while setting the longitude of Earth to $\lambda_\oplus = 65°$. The color bar represents the density values of the contour levels of the combined components. The blue circle represents the Earth, with Earth's orbit marked in black dashed lines.

due to the band pair overlapping, which effectively doubles the density at the ecliptic equator. We also note that all three bands do have densities extending past the relevant line-of-sight integration ranges set to 5.2 AU, although we do not expect IPD at such a distance to make any significant contribution to the sky brightening. We will discuss the reasoning behind this integration length in section 7.1.4.

7.1.3 The Circumsolar Ring and the Earth-trailing Feature

The Circumsolar Ring and Earth-trailing Feature are seen in the bottom row of Figure 7.2 in the left- and right-most subplots, respectively. The Circumsolar Ring exhibits a peak density at 1.03 AU with a width of roughly 0.1 AU, making it sharply defined in space in contrast to the previously discussed components. The Earth-trailing Feature has no plane of symmetry unlike the other components and, therefore, only appears on one side of the contour plot as it was computed while setting the longitude of Earth to $\lambda_{\oplus} = 10°$ such that the Feature appears directly in the cross-section.

The Earth-trailing Feature is seen to be wider than the Circumsolar Ring in this cross section, but it is hard to make any comments on the exact shape of the component from these figures alone. We have, therefore, included an additional plot seen in Figure 7.3 where we get an overhead view of the two components through a cross-section of the xy-plane. In this figure, the Earth, represented by the blue circle, is positioned at a longitude of $\lambda_{\oplus} = 65°$, with the black dashed lines showing its orbit. This view gives us a better understanding of the geometry of the system between an observer and the two components. From the overhead view, it becomes apparent that the Earth-trailing Feature exhibits an oval-like form, which significantly enhances the IPD density in the region directly behind the Earth. We also note small asymmetries along the Circumsolar Ring caused by the components tilt (0.5°) with respect to the Ecliptic. The Earth orbits at the inner edge of the ring, meaning that it, along with any nearby observer, is encapsulated in the dust from both components. The beam of an observer will, therefore, always look through a portion of this dust. As such, we should expect these two components to contribute with some emission over the full sky, similar to the Diffuse Cloud.

7.1.4 Comments going into map production

Having gained some valuable insight into the geometry of the Zodiacal components, the next natural step in our analysis is to apply this knowledge to produce ZLE templates. The IPD model is converted to ZLE templates through the line-of-sight integration. We discussed how we would perform these calculations in detail in chapter 6.3, but there was one quantity that we left unelaborated, the maximum integration length R_{max}. This length describes the radius of a circle with Sun as the origin and sets a limit to which part of the IPD distribution we will consider when computing the ZLE. Optimally, the integral would be performed from the location of the observer and to infinity, but this is computationally infeasible. Typically, this value would be selected to make sure that we capture all the significant ZLE produced by the model, although, selecting this value is not trivial.

The first problem is related to the efficiency of the model. Increasing R_{max} while leaving the integration step length the same would directly increase the computation times of the module. To compensate for this, we would have to increase the step length, which would in turn decrease the integration accuracy. The second problem is related to the diffuse nature of the Zodiacal components making it difficult to select a clean cut-off distance at which their densities become small enough for us to be able to neglect the emission produced. On top of this, the emissivities differ for each component at the different frequencies making the contribution from some of the components at far distances more significant at specific frequencies.

A third potential problem that is more or less connected to the nature of the parametric model is whether or not we can even treat $R_{\max}$ as a free parameter. K98 obtained the model parameters using a radial cut-off at $R_{\max} = 5.2$ AU, which corresponds roughly to Jupiter's orbit. Performing a fit of the model parameters using different values of $R_{\max}$ could potentially have resulted in different model parameters. We do not expect the structure of a ZLE map to change with $R_{\max}$, but the component amplitudes will change as more emission is captured by the model for larger values of $R_{\max}$. This could potentially change the best-fit values for parameters such as the peak-densities of the Zodiacal components. In line with this discussion, we believe that the safest option is to adopt the radial cut-off value of $R_{\max} = 5.2$ AU, as used by K98.

7.2 Producing maps with the Zodiacal Emission module

Although the main application of the ZLE modules is to produce ZLE templates for high-frequency data sets, only the LFI time-ordered data was fully prepared for use at the time during this analysis. From our previous discussion on the ZL, we know that there is inconsiderable emission produced at the frequency ranges covered by the LFI. Nevertheless, the module requires information on instrument pointing and observer location at the time of observation to function. For the sake of being able to test the module, we will use the LFI 30 GHz data and manually set the frequency in the calculations to 857 GHz so that we can compare our results with those obtained by *Planck* in *Planck* Collaboration XIV (2013) [45]. We will assume that the difference in pointing between the LFI and HFI is small enough such that we still get representative results.

7.2.1 Zodiacal component maps over surveys 1 and 2

To make sure that the line-of-sight calculations are working properly, we test if our module can reproduce the structure seen in the 857 GHz unit emissivity ZLE templates produced by *Planck* Collaboration XIV (2013) [45] seen in Figure 5.3. There are two benefits to making maps with unit emissivity: 1) the emissivity as defined in our model works like a direct scaling of the templates. Having computed each component with unit emissivity means that we can construct any other ZLE template at the same frequency as a combination of the individual components scaled by their respective emissivities; 2) the individual strength of each component is illustrated as if they all emitted perfect black body radiation.

Similar to *Planck*, we produce the ZLE unit emissivity templates for *Planck* surveys 1 and 2. Our results are seen in Figure 7.4. The rows show the Zodiacal components from top to bottom: 1) the Diffuse Cloud; 2) Dust Band 1; 3) Dust Band 2; 4) Dust Band 3; 5) the Circumsolar Ring; and, 6) the Earth-trailing Feature. The columns

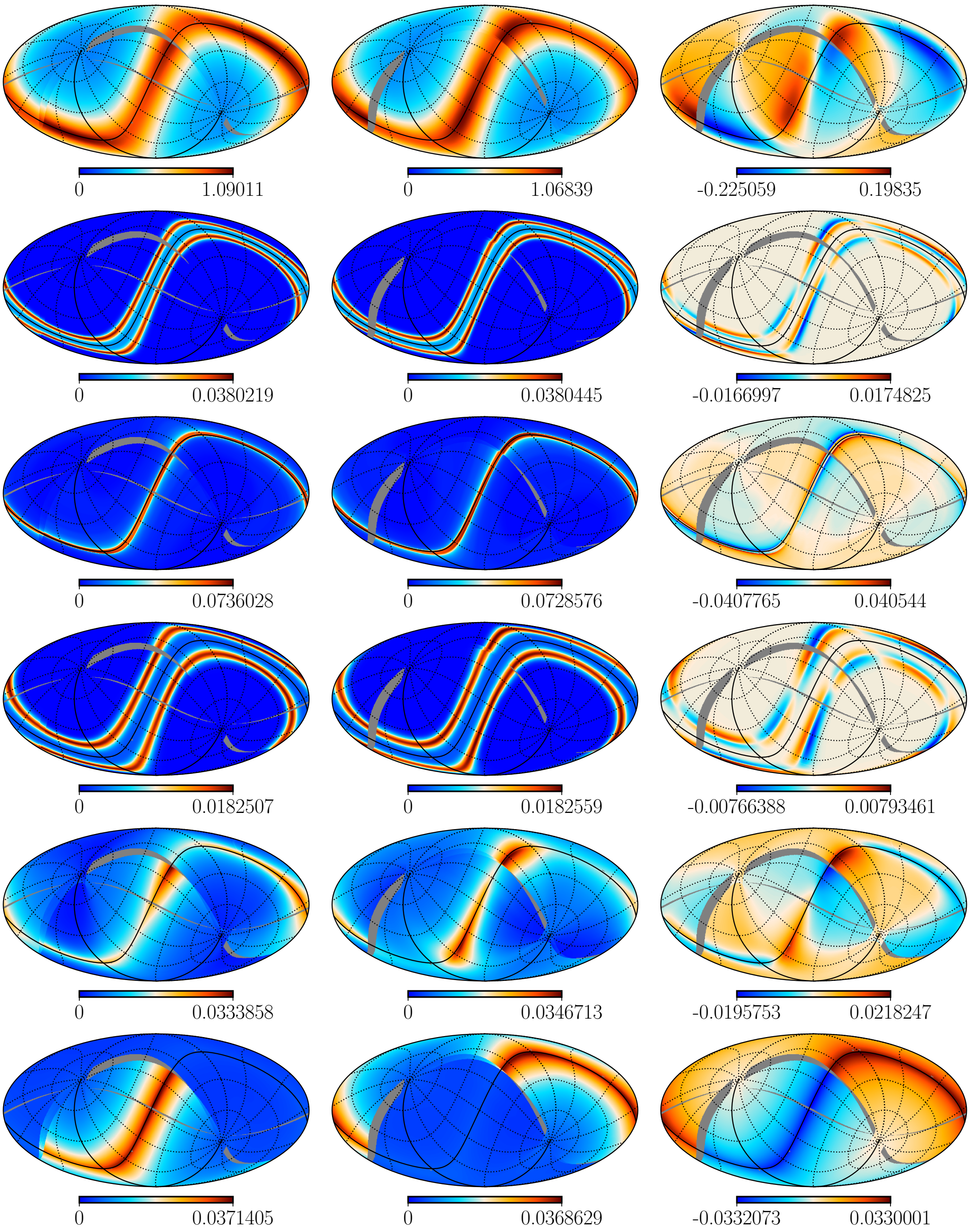

Figure 7.4: Estimated ZLE maps of Zodiacal component with unit emissivity at 857 GHz in units of MJy/sr. Columns show survey 1, survey 2, and the difference between the two surveys, respectively. Rows show the following components, from top to bottom: 1) the Diffuse Cloud; 2) Dust Band 1; 3) Dust Band 2; 4) Dust Band 3; 5) the Circumsolar Ring; and 6) the Earth-trailing Feature. Note that these are estimated using 30 GHz pointing.

from left to right show the expected emission for *Planck* surveys 1, 2, and the difference between these surveys (survey 2 - survey 1). The maps are plotted in units of MJy/sr. Since the ZLE is mostly aligned with the Ecliptic, it is useful to include graticules that show lines of parallel ecliptic latitude and longitude in the plots. It should be noted that *Planck* appears to have mixed up Dust Bands 1 and 3 in their paper (Dust Band 3 appears at the largest ecliptic latitude).

We were unable to make direct comparisons between our results and *Planck*'s, as we could not get our hands on the necessary data files. It is, however, still possible to compare the overall map amplitudes and the structure. The structure in our maps seems to coincide well with that of the *Planck* templates, with the only noticeable exception being the templates for the Circumsolar Ring. In terms of amplitude, our templates seem to be generally weaker than those computed by *Planck*. The Diffuse Cloud is weaker by approximately 8% in both survey maps, the Circumsolar Ring by 26% in survey 1 and 20% in survey 2, and the Earth-trailing Feature by 18% in survey 1 and 26% in survey 2. On the other hand, the amplitudes of the Dust Bands coincide very well with the results of *Planck*. Dust Bands 1 and 3 differ only by 1%, with Dust Band 2 differing by 5%. It is difficult to pinpoint the exact reason as to why our templates appear to be weaker than *Planck*'s, but we believe it might be due to either of the following (or a combination of these):

1. There seems to be a correlation between the proximity of the Zodiacal component presented in a template and the relative errors in maximum amplitude between our results. The Diffuse Cloud, the Circumsolar Ring, and the Earth-trailing Feature are all components with peak densities in proximity to the observer. As such, the observed emission is extremely sensitive to variations in the position of the observer. For instance, by assuming that the observer was located on Earth instead of L2, we would effectively move the observer to a denser region of the Diffuse Cloud, which would result in more ZLE captured in a line-of-sight. Similarly for the Circumsolar Ring and the Earth-trailing Feature, any line-of-sight drawn by our module would look through a longer region of density, resulting in more signal. It is, therefore, possible that some of the differences in amplitude between our maps are attributed to certain assumptions made by us or the *Planck* collaboration regarding observer position. In our module, we update the observer position once per observational hour, using the ecliptic *Planck* coordinates provided by the HORIZONS Web-Interface [54].

2. We are uncertain of the extent to which using the data pointing of the 30 GHz time-ordered data affects our results, although we do not have any motive to believe that this would change the amplitudes.

3. We were informed that a bug was present in the code during the making of the *Planck* 2013 maps after a conversation with Kenneth Ganga, the writer of the original Planck Zodiacal module. Despite not knowing exactly how the bug affected the templates, it is reasonable to believe it could have affected the amplitudes.

Overall we believe that our results are in line with the objective of BeyondPlanck, and hence we continue with the production of the final results, which are the full survey ZLE maps.

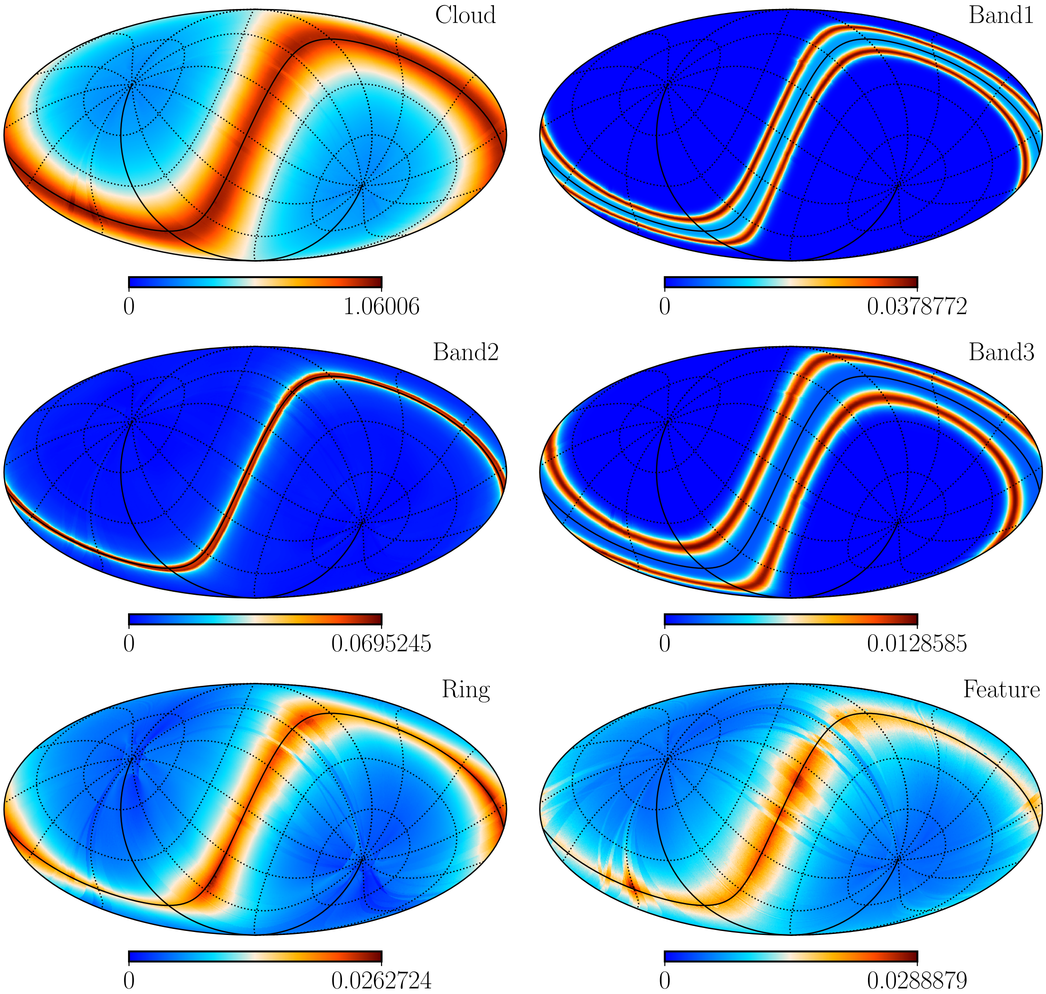

Figure 7.5: Maps of the estimated ZLE for each Zodiacal component computed with unit emissivity at 857 GHz in units of MJy/sr over the HFI data set including surveys 1-5. From top to bottom: row 1) the Diffuse Cloud (left), and Dust Band 1 (right); row 2) Dust Band 2 (left), and Dust Band 3 (right); row3) The Circumsolar Ring (left), and the Earth-trailing Feature (right).

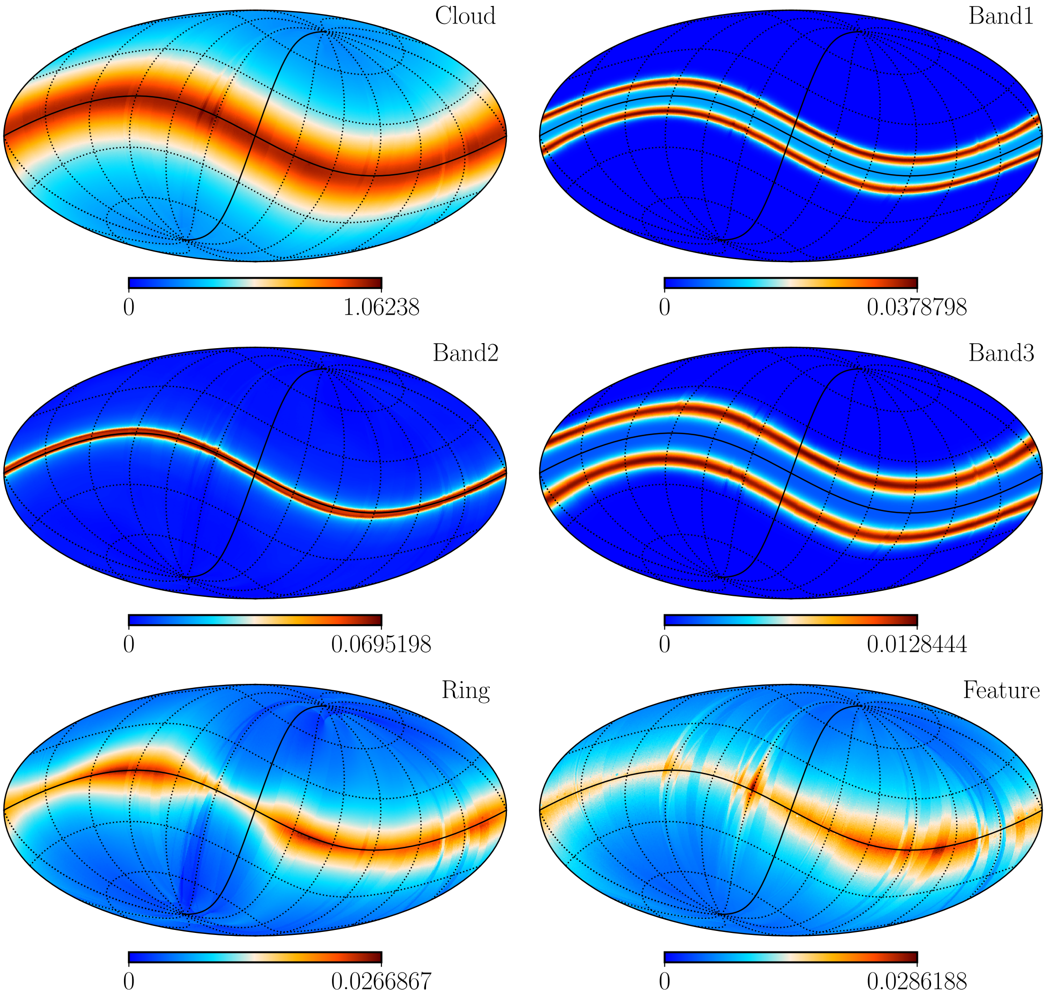

Figure 7.6: Templates of the estimated ZLE for each individual Zodiacal component with unit emissivity at 857 GHz in units of MJy/sr over the the HFI data set including surveys 1-5. From top to bottom: row 1) the Diffuse Cloud (left), and Dust Band 1 (right); row 2) Dust Band 2 (left), and Dust Band 3 (right); row3) The Circumsolar Ring (left), and the Earth-trailing Feature (right).

7.2.2 Zodiacal component maps over the full HFI data set

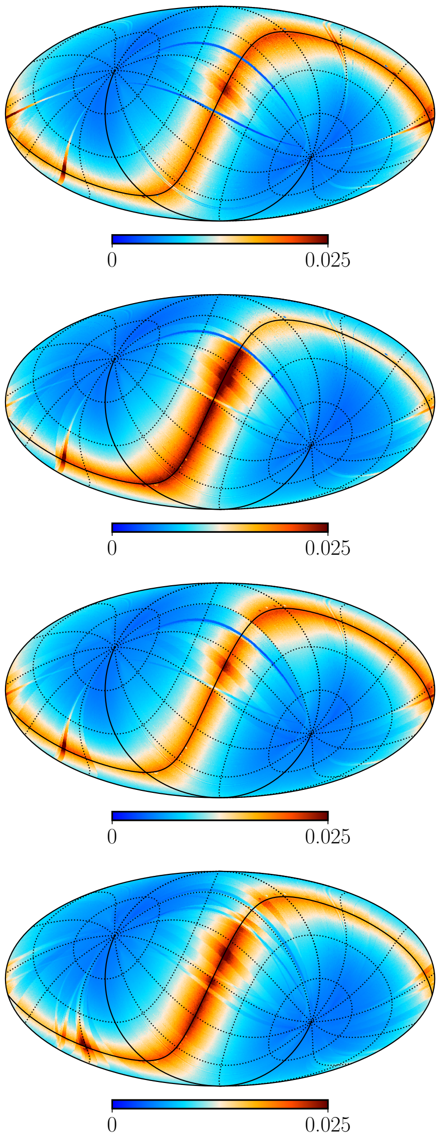

Figure 7.7: Composite survey maps of the Earth-trailing feature at 875 GHz with unit emissivity. From top to bottom the ZLE computed over surveys: 1) 1-2; 2) 1-3; 3) 1-4; and 3) 1-5.

The next step in our analysis is to scale up the survey numbers so that the produced ZLE templates represent the complete HFI data set, which is where the Zodiacal corrections are required. Figure 7.5 shows each Zodiacal component at 857 GHz in units of MJy/sr with unit emissivity computed over *Planck* surveys 1-5. Additionally, we have included a similar figure where the components are plotted in celestial coordinates, which are coordinates relative to an observer situated on Earth. This figure may present a more intuitive view of the Zodiacal components considering our experience with the isodensity contour figures, in addition to better representing the ZLE as seen by an observer on Earth.

In general, we observe that the emission in each map is now much more evenly distributed about the full structure of each component. This is the result of `Commander` mapmaking combining and weighting all *Planck* surveys based on pixel hits, which effectively smoothes out any time-dependent feature that differed between the survey maps. Additionally, we observe a few stripy features most prevalent in the Circumsolar Ring and the Earth-trailing Feature maps, which both look strikingly different from the single survey counterparts. To better study these stripy structures, we include four composite survey maps of the Earth-trailing Feature computed with increasing data volumes. These can be seen in Figure 7.7, which from top to bottom shows the ZLE estimated over the composite *Planck* surveys: 1) 1-2; 2) 1-3; 3) 1-4; and 3) 1-5, plotted in the same color range in units of MJy/sr. In the 1-2 survey map, we see that mapmaking has normalized the observed emission over the two individual surveys so that the observed structure now covers the entire ecliptic at roughly half the amplitude. We also observe the aforementioned stripy features, which appear in the regions with non-overlapping sky coverage. In the 1-3 multi-

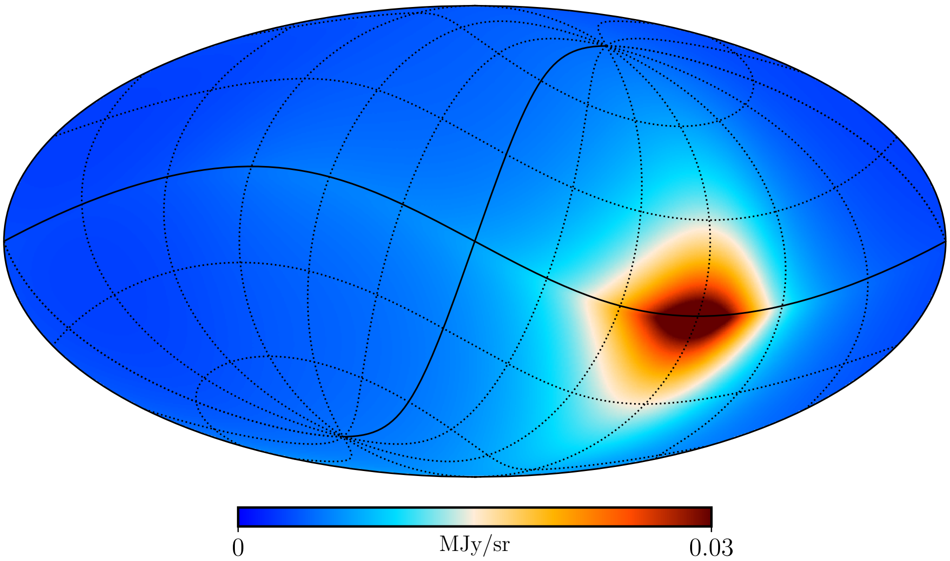

Figure 7.8: The Earth-trailing Feature as seen by an observer sitting at a constant heliocentric position over the course of a full-sky survey. Units are MJy/sr.

survey map, we have effectively added a set of data where the Earth-trailing Feature is only observed over half the sky. Mapmaking expectedly enhances this region in amplitude while weakening the remaining region. Non-overlapping regions are especially subject to the effects of mapmaking, which results in additional stripes. This process is repeated with the addition of surveys 4 and 5, as seen in the 1-4 and 1-5 composite maps. These observed effects are somewhat enhanced with the addition of surveys 4 and 5 due to lesser sky coverage. Such stripes are not unique to the Earth-trailing Feature but become most prevalent due to the strong temporal variance of the component. By carefully observing each component map, we see that these also exhibit small stripy structures in the same regions.

The appearance of the Earth-trailing Feature in our maps can be confusing. After all, the isodensity contours displayed an oval-formed density distribution constrained to a small portion of the sky. The reason as to why the Earth-trailing Feature appears as a "continuous" band across the Ecliptic is due to the scanning strategy of *Planck*. The Earth-trailing Feature appears directly behind *Planck* as the satellite moves along the orbit of Earth, such that its position shifts with every rotation of the satellite. This also means that the Earth-trailing Feature is directly looked through by a beam in roughly half of the observed data by *Planck*. We can, however, simulate what the component would look like if *Planck* were to stand still along with the Earth and observe the full sky. By setting the observer position to a constant location along the Ecliptic, the Earth-trailing Feature does take the shape of an oval-like distribution, as seen in Figure 7.8. This figure will hopefully help convince the reader that all components are properly implemented in our module and that the patchy appearance exhibited by some of the maps is due to the *Planck* scanning strategy and mapmaking.

Before we move on to combining and scaling the full-mission component templates by their respective emissivities, we would like to make some general comments on the observed structure of each component based on our expectations coming from the Zodiacal component study. The Diffuse Cloud matches well with our predictions; most of the emission is concentrated around the Ecliptic with a significant contribution to the full sky as a result of the inner Solar System being encapsulated by IPD. The Dust Bands appear as band pairs at inclinations matching the latitudes seen in the isodensity contours. We did expect Dust Band 2 to contribute with significant emission to the full sky due to the observer position with respect to the density peak, but this is not the case. It seems that the magnitude of the peak density is so small that the emission from the very surroundings of the observer becomes negligible compared to the integrated density along the Ecliptic. Additionally, we also predicted that the Circumsolar Ring and the Earth-trailing Feature would contribute with some emission over the full sky due to the geometry between the components and the observer. Although we do observe some emission over the full sky for these components, it appears to be less significant than initially assumed, likely due to the reasoning above.

7.2.3 *Planck* best-fit Zodiacal emissivities

We recall from our discussion on the Zodiacal Light in chapter 2 that the IPD does not emit perfect blackbody radiation. Each Zodiacal component may consist of dust grains with different compositions such that the emitted radiation deviates from standard blackbody emission by various amounts. The IPD model accounts for this variation by scaling the emission for each component with an emissivity parameter. The emissivities would optimally be obtained by fitting the unitary component templates to the processes BeyondPlanck HFI data through equation (5.16). In the next phase of BeyondPlanck, we will obtain these emissivities by fitting the unitary component templates to the processed BeyondPlanck HFI data through equation (5.16). For now, we will proceed with the emissivities as fit by *Planck* in the 2013, 2015, and 2018 *Planck* analysis. These can be seen in Figure 5.5, and in Table 5.2.

To give us a clearer picture of the *Planck* emissivities, we have plotted the 2013 and 2018 fits against frequency, as can be seen in Figure 7.9. The estimates found from the 2013 analysis (left) included all Zodiacal components, while the 2018 analysis (right) only included the Diffuse Cloud and the three Dust Bands. We previously mentioned that the fit performed in the 2013 analysis resulted in strange emissivities. This is evident in our plot, where we see several missing fits due to negative estimates and generally large uncertainties. In the 2015 and 2018 fits, *Planck* omitted the most troublesome components, those being the Circumsolar Ring and the Earth-trailing Feature components. Additionally, the bug present in the code at the time of the 2013 analysis was fixed. The emissivities obtained in the 2015 and 2018 analysis are all positive, with more reasonable uncertainties that decrease smoothly with frequency as expected due to a lack of ZLE at lower frequencies. The fit also suggests that the radiation emitted

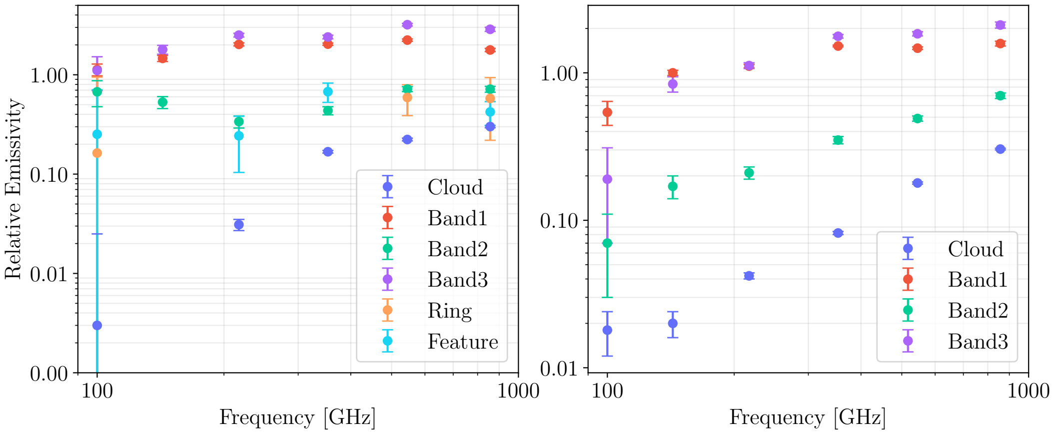

Figure 7.9: Best-fit emissivities found by the *Planck* collaboration 2013 results (left) and 2018 results (right) plotted against frequency to highlight the frequency dependence. Negative estimates do not show up in the plots due to the log-log scale.

by the components falls linearly with frequency in log-log space. Note that this is on top of the typical blackbody feature of weakening with frequency. When it comes to the overall emissivity amplitudes, *Planck* made the following comment in the 2015 analysis: "- the overall amplitudes of the emissivities, which are completely degenerate with the assumed particle density in the bands, are not being interpreted physically." (*Planck* 2015 results. VIII. 2015, p.12). We will continue our analysis using the emissivities from the 2015 and 2018 fits. The only problem with this is that we disregard the Circumsolar Ring and the Earth-trailing Feature components, which we know to be true physical components of the IPD distribution. It is possible that by fitting emissivities to templates made solely with the Diffuse Cloud and Dust Bands, we accidentally capture any residue emission from the rejected components that is overlapping with the cloud or bands. This could explain why the emissivities of the Dust Bands are seen to be slightly larger in the 2015 and 2018 fits at 857 GHz, although, it is hard to make any decisive conclusion as the remaining five frequency bands all exhibit at least one negative fit in the 2013 results.

The applicability of the emissivity scaling can be tested against the 2013 Zodiacal correction maps seen in Figure 5.4. Our frequency templates produced for the full HFI mission with the 2013 emissivities can be seen in Figure 7.10, where we have used the same color ranges as *Planck*. We observe a strong agreement between our results and the 2013 corrections, which indicate that our module is functioning properly. The 857 GHz *Planck* Zodiacal correction map exhibits some notable differences from our 857 GHz map. These differences are likely due to other contamination sources such as far sidelobes, which are also present in the *Planck* Zodiacal correction maps. Other than this, we observe slight deviations in amplitude, which we expect as our unit emissivity maps were generally weaker than the *Planck* counterparts.

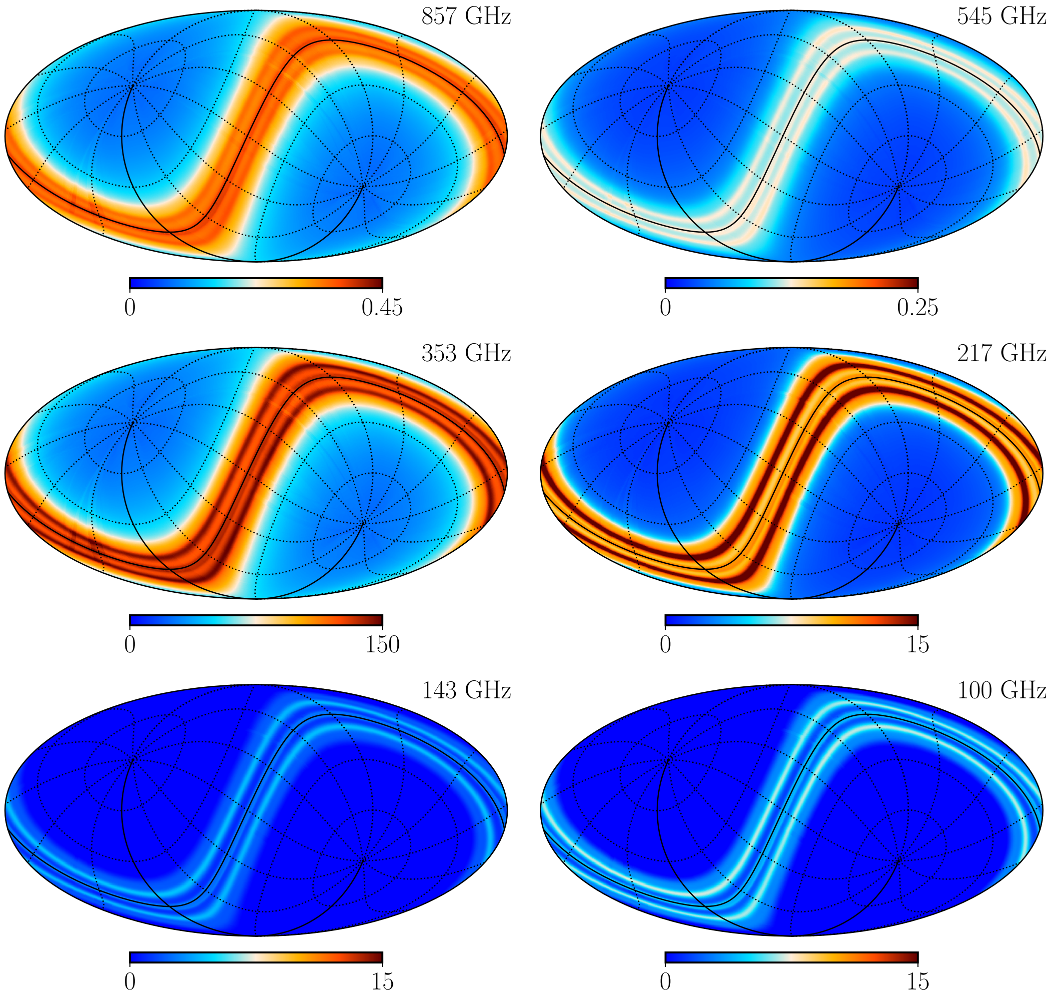

Figure 7.10: ZLE templates produced with *Planck* 2013 emissivities. Units are MJy/sr for 857 GHz and 545 GHz, and $\mu\mathrm{K}_{\mathrm{CMB}}$ for the other frequencies.

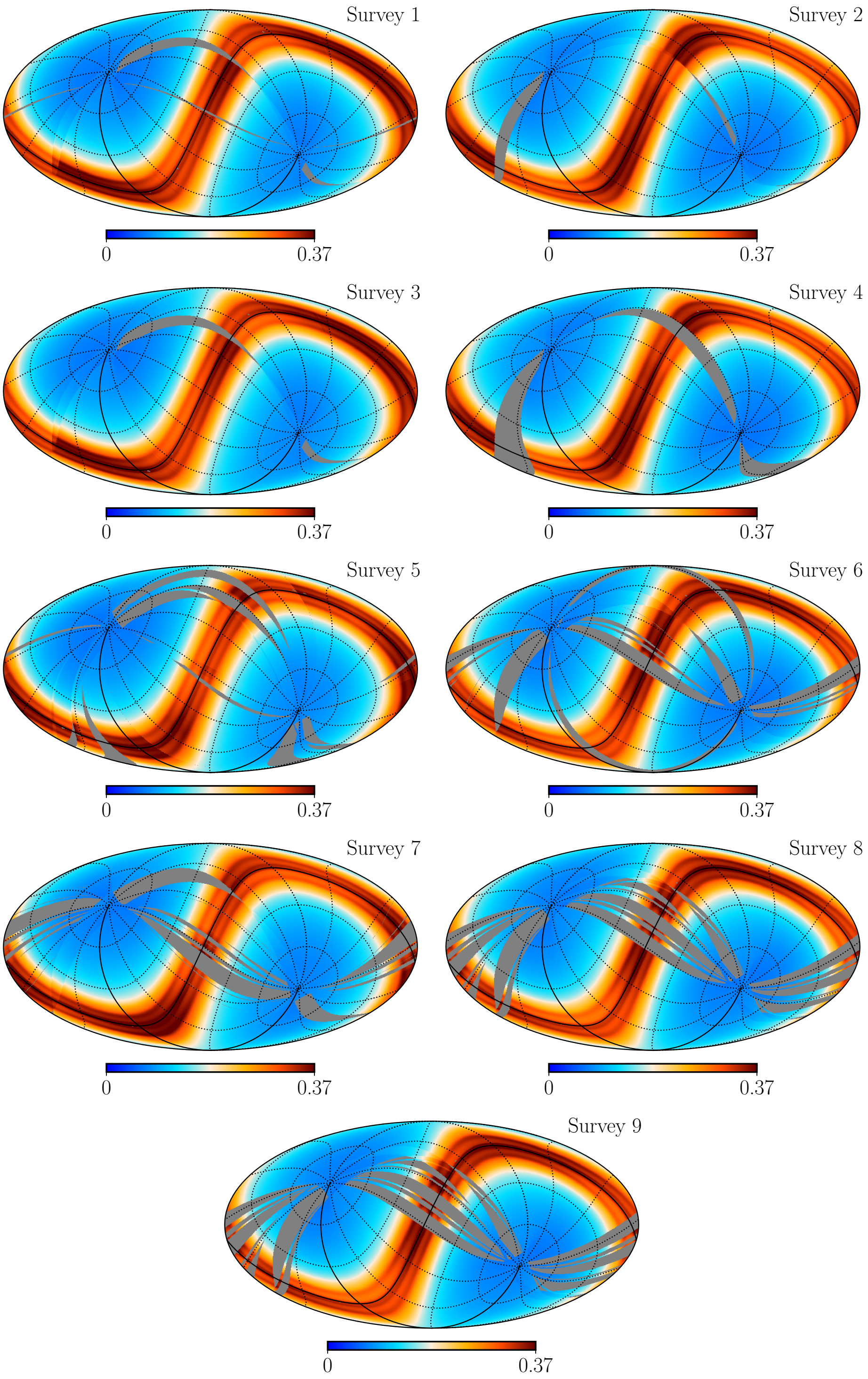

Figure 7.11: Estimated ZLE templates at 857 GHz in units of MJy/sr, as seen by *Planck* over each observational survey.

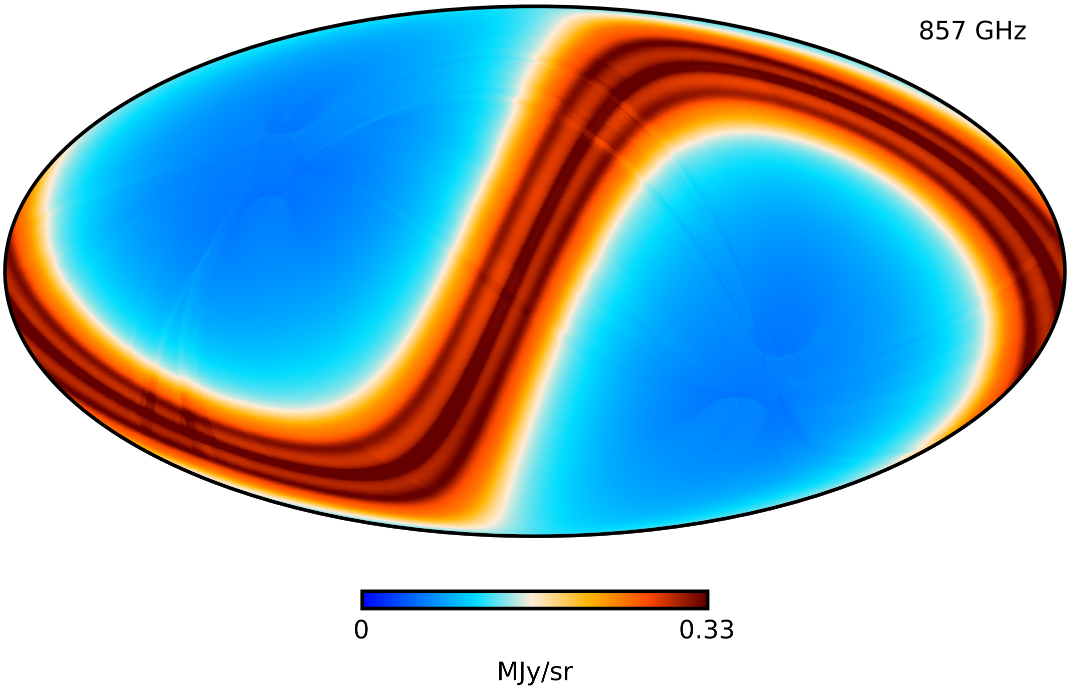

Figure 7.12: ZLE template of the full HFI mission at 857 GHz produced with the *Planck* 2015 emissivity fits.

7.2.4 Zodiacal emission frequency templates

Having tested the different aspects of the module, we are ready to present the final products produced by the BeyondPlanck Zodiacal emission module; the ZLE frequency maps that will represent $\boldsymbol{s}_{\mathrm{zodi}}$ in the BeyondPlanck HFI data model. The first frequency templates we present are the individual survey maps estimated with the 2018 emissivities at 857 GHz, seen in Figure 7.11. HFI , These maps do a good job of illustrating both the time dependence of the ZLE and the varying sky coverage of each survey. The unobserved patches on the sky, masked in gray, are seen to match the regions where the stripes were observed in the full HFI unitary component maps in Figure 7.5. These results also show that we are able to flexibly estimate the ZLE for any given portion of data, which will significantly help analysis in the coming BeyondPlanck HFI analysis.

The main portion of the BeyondPlanck high-frequency analysis will be performed over the complete HFI data set. As such, the primary use case for our Zodiacal Emission module before estimating our own Zodiacal emissivities will be to produce full HFI mission ZLE frequency templates with the 2018 *Planck* fit. We present these templates in a gallery at the end of the result part of the thesis, more specifically in section 7.7. We are unable to test the credibility of these with other similar templates due to the lack of *Planck* 2018 ZLE templates. We can, however, make comparisons between our full mission templates scaled by the 2015 fits, seen in figure 7.12 and those used by

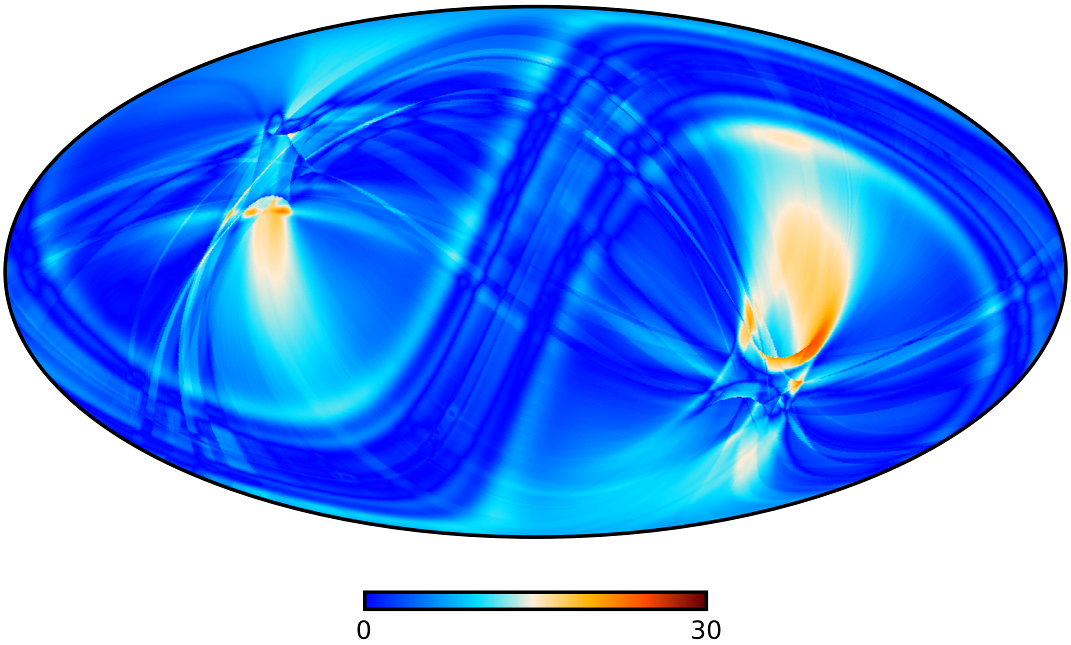

Figure 7.13: Relative difference map in percentage between the 857 GHz normalized *Planck* and our Zodiacal Emission module ZLE templates.

`Commander` during the *Planck* 2015 analysis, which we were able to find. It is sufficient to only consider the 857 GHz template since the structure of each Zodiacal component remains constant with frequency, only changing in amplitude. Comparing the templates directly through difference maps is ineffective due to the initial difference in the map amplitudes following our unit emissivity results. Instead, we normalize both templates and use these to produce a relative difference map given by

$$\boldsymbol{d}_{\mathrm{r}} = \frac{\mid \tilde{\boldsymbol{s}}_{\mathrm{zodi}}^{\mathrm{Planck}} - \tilde{\boldsymbol{s}}_{\mathrm{zodi}}^{\mathrm{BP}} \mid}{\mid \tilde{\boldsymbol{s}}_{\mathrm{zodi}}^{\mathrm{Planck}} + \tilde{\boldsymbol{s}}_{\mathrm{zodi}}^{\mathrm{BP}} \mid /2}, \tag{7.1}$$

where

$$\tilde{\boldsymbol{s}}_{\mathrm{zodi}} = \frac{\boldsymbol{s}_{\mathrm{zodi}}}{\max(\boldsymbol{s}_{\mathrm{zodi}})}. \tag{7.2}$$

This difference map between our 857 GHz estimate and the *Planck* equivalent is shown in Figure 7.13. The main Zodiacal structure appears to agree well in both maps, differing only by a few percents. Our template appears to exhibit a wider overall structure along the Ecliptic. The region on the sky where we observe the biggest difference between the two templates is the ecliptic poles. This is also the region with the highest integration time during each survey due to the scanning strategy of *Planck*. We believe that this error might result from inaccurate pointing information due to our approximation of using the 30 GHz LFI pointing. It could also be an effect of differences in the data sets as we have uncarefully used the full survey 5, although the HFI only partially observed during this survey.

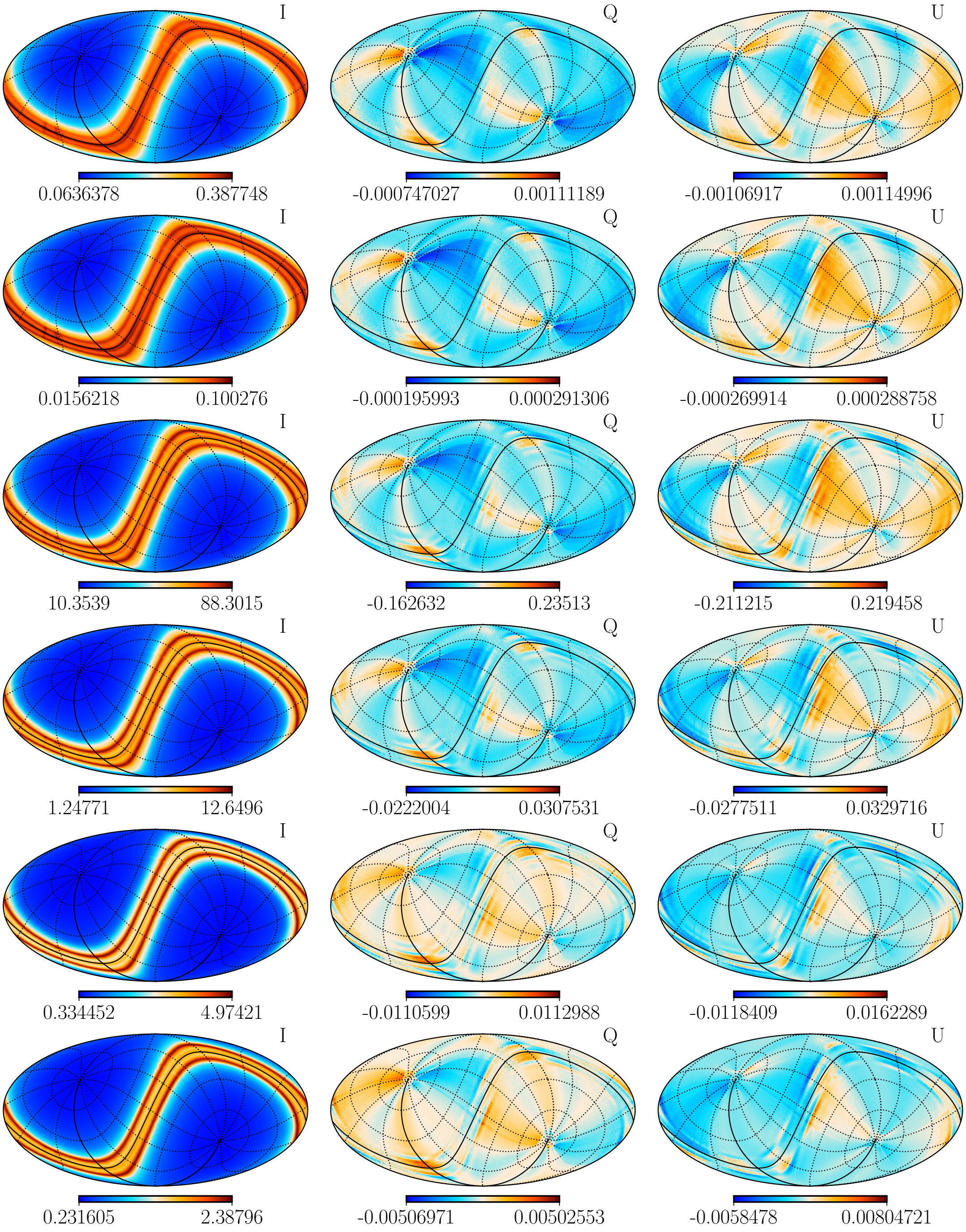

Figure 7.14: Stokes I, Q, and U maps of the ZLE at each HFI frequency. Units of MJy/sr for 857 GHz, and μK_{CMB} for the other frequencies. Columns show Stokes parameters I, Q, and U, respectively. The Q, and U maps show the polarization leakage from I as seen by *Planck* over the HFI mission. Rows show the following frequencies, from top to bottom: 1) 857 GHz; 2) 545 GHz 1; 3) 353 GHz 2; 4) 217 GHz 3; 5) 143 GHz; and 6) 100 GHz.

7.2.5 Polarization leakage

Mapmaking allows us to solve the sky signal in terms of intensity, given by the Stokes parameter I or linear polarization, given by Stokes Q and U, respectively. In a given coordinate frame, Stokes Q represents the difference between linear polarization in the horizontal and vertical direction, while Stokes U represents the same system rotated by 45°. Together, Q and U form the basis of linear polarization. Since *Planck* is polarization sensitive, `Commander` mapmaking solves the sky signal into all three Stokes parameters.

The IPD model used in the Zodiacal Emission module does not account for polarization, and as such, one might expect the Q and U maps to be signal-free. However, this is not the case, as is seen in Figure 7.14, where we have plotted all three Stokes parameters for each full mission ZLE frequency maps. The observed polarization signal is the result of so-called polarization leakage, a process in which signal leaks from temperature to polarization in the mapmaking process. Although the leakage in Q and U is small compared to the I-signal (typically less than 1%), the I-signal itself is massive compared to the types of polarization signal which we hunt. As such, polarization leakage tends to quickly become a dominating systematic. Any polarization contamination, whether it is from foregrounds or instrumental effects, has to be accounted for to nanokelvin precision if we are to detect the elusive gravitational waves. Polarization leakage of this form is particularly important to coming CMB missions such as the hypersensitive LiteBIRD, which will observe the sky at frequencies up to 400 GHz, making precise Zodiacal corrections along with any polarization leakage very relevant.

7.3 Zodiacal brightness profiles

Having computed the ZLE frequency maps allow us to study the IPD as seen by *Planck* in further detail. By binning the maps in heliocentric latitudes, we can observe the emission as a function of latitude. This is illustrated in Figure 7.15, which shows the brightness (intensity) profiles of the ZLE. The top subfigure shows the brightness for each *Planck* frequency, as described by the 2018 *Planck* Zodiacal emissivities. The bottom subfigure illustrates how each Zodiacal component contributes to the total brightness profile at 217 GHz. A small noise-like feature is observed in the profile of Dust Band 1 at $\sim 33°$. This feature could be the result of the stripes observed in our maps, as discussed in section 7.2.2. However, if this was the case, then we should expect to see a similar feature in all components at the same latitude. As such, we believe this to be the result of small errors made during the binning process as we also observe noise-like structure at high latitudes for all components.

Although this type of result is not of direct use to component separation, it can prove useful to the IPD community. The brightness profiles can help constrain the dust composition in the various Zodiacal components by comparing theoretical models describing dust emission to our results. Additionally, the profiles can be used to associate the Dust Bands to asteroid families observed at similar latitudes, further giving insight into the composition of the dust.

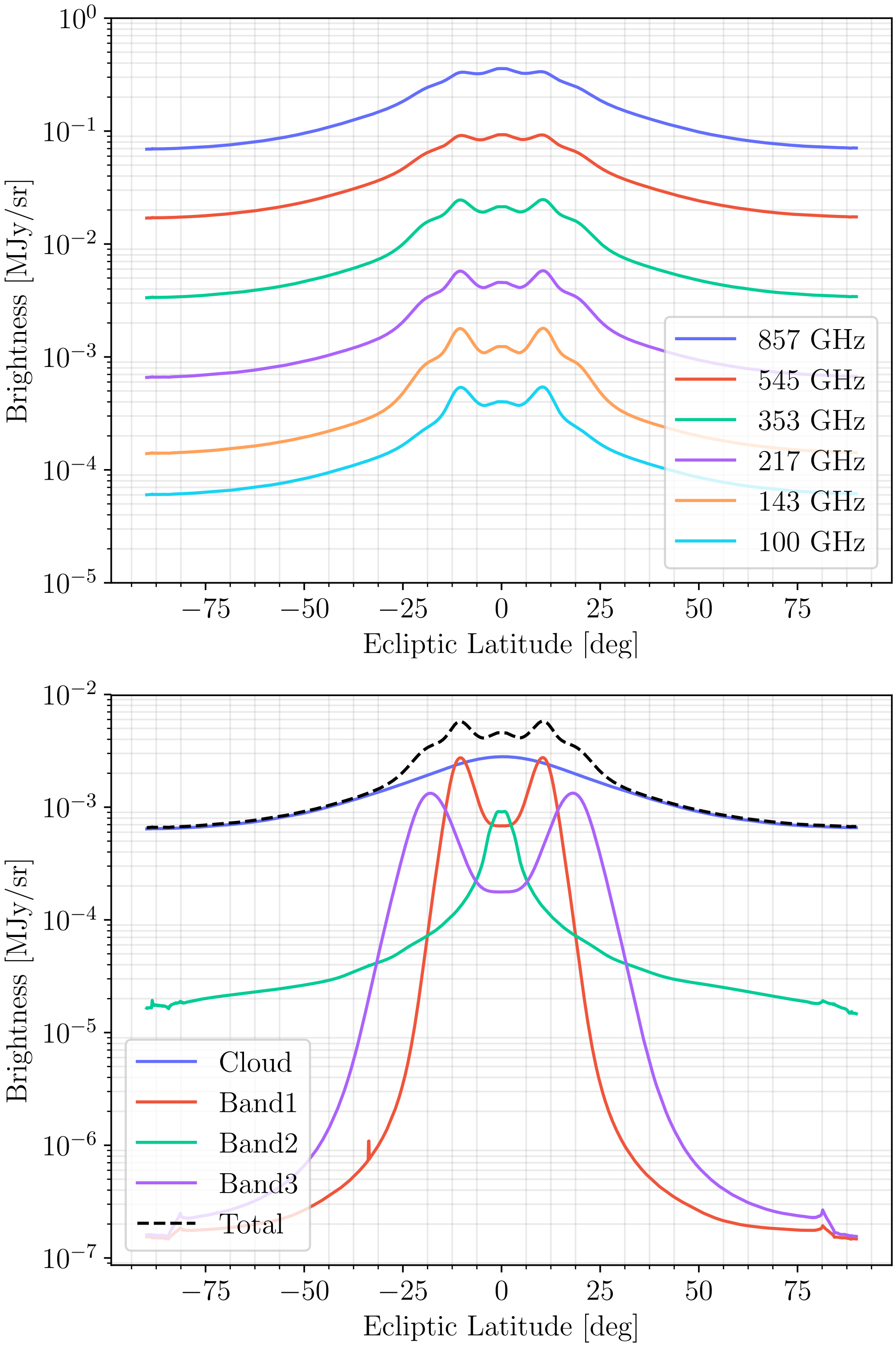

Figure 7.15: Brightness profiles for the ZLE computed with the 2018 *Planck* Zodiacal emissivity fits binned in heliocentric latitudes. Top: brightness profile at each *Planck* frequency. Bottom: componentwise brightness at 217 GHz.

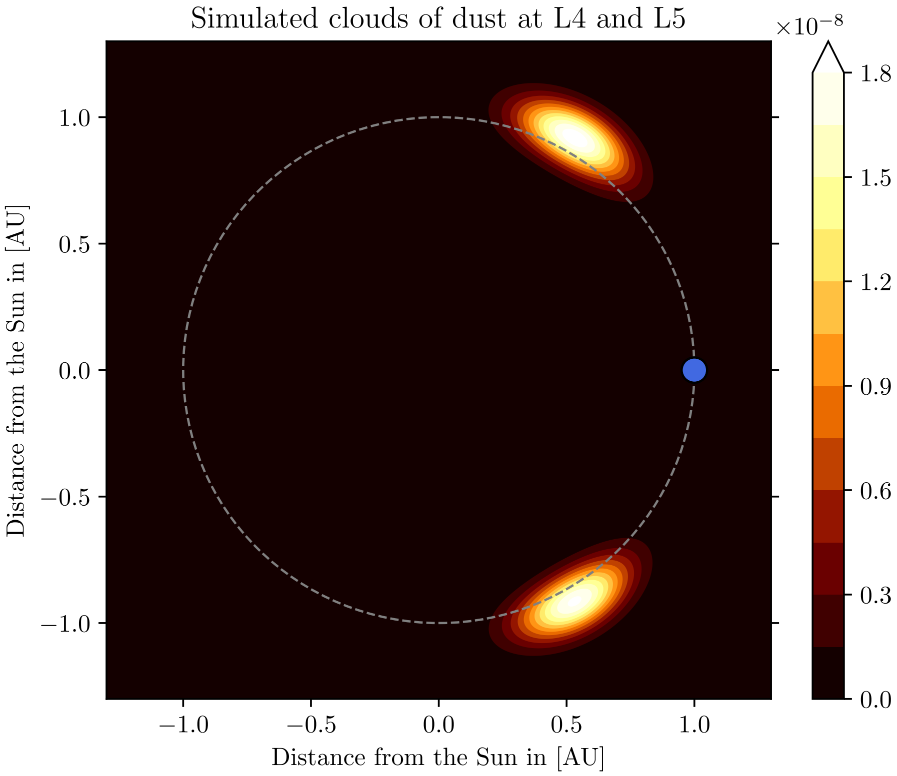

Figure 7.16: Isodensity contour of the simulated dust clouds at the Lagrange points L4 and L5 in a cross-sectional slice along the ecliptic plane. The clouds are computed while setting the longitude of Earth to $\lambda_\oplus = 0°$. The color bar represents the density values of the contour levels. The blue circle represents the Earth, with Earth's orbit marked in gray dashed lines.

7.4 Simulating possible enhancements to the dust concentration in the Circumsolar Ring

Recent discoveries about the IPD distribution suggests that there are enhancements to the dust concentration at the L4 and L5 Lagrangian points of the Earth-Moon system, called Kordylewski clouds. These were first predicted by Kazimierz Kordylewski in 1961 [55] and confirmed in 2018 [56]. These clouds are, however, located far within *Planck*'s orbit and are therefore never directly observed during a survey due to the scanning strategy of the satellite. However, findings such as the Kordylewski clouds and the Earth-trailing Feature shows that in general, IPD tends to concentrate at or in proximity of the Lagrange points. In 2010, NASA's Wide-field Infrared Survey Explorer discovered a near-Earth asteroid orbiting at L4 [57]. This asteroid may well be accompanied by a concentration of IPD, which in turn would suggest that Sun-Earth

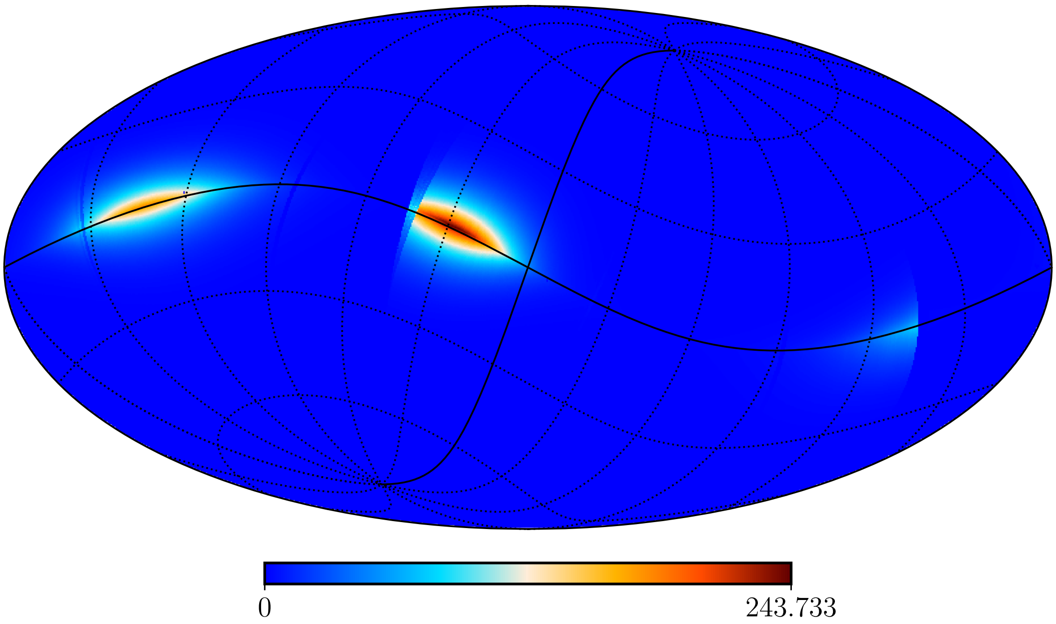

Figure 7.17: ZLE from the simulated dust enhancements at the Lagrange points L4 and L5 as seen by *Planck* over survey 1. Units are $\mu\mathrm{K}_{\mathrm{CMB}}$.

L4 and L5 points could be hotspots for interplanetary dust.

The framework of our BeyondPlanck Zodiacal Emission module allows us to perform a simple simulation to test the significance of ZLE originating from these Lagrange points. The Sun-Earth L4 and L5 points are located at Earth's orbit at 60° angles opposite of the Sun. By altering the geometrical parameters of the Earth-trailing Feature, more specifically by changing θ_{TB}, the longitude of the Earth-trailing Feature with respect to Earth to $\pm 60°$, we can effectively shift its location to the L4 and L5 Lagrangian points. The isodensity contours for clouds appearing at these regions can be seen in Figure 7.16. The other parameters are left untouched as this is a simple simulation to primarily illustrate the significance of emission from such distant clouds. If such clouds were indeed present at the order of magnitude the Earth-trailing Feature, then according to the Zodiacal Emission module, *Planck* would have observed the following ZLE over survey 1, seen in Figure 7.17, where the emission is plotted in units of $\mu\mathrm{K}_{\mathrm{CMB}}$ in celestial coordinates. The two clouds appear as faint spots along the Ecliptic in an otherwise empty map. The signal strength is roughly 3 orders of magnitude weaker than the total ZLE emission at the same frequency. It, therefore, unlikely that an improvement of this order would play any immediate role in the Zodiacal corrections performed; the uncertainties related to the parametric IPD model outweigh any correction of this size. It is still, however, important to quantify possible sources of emission in the grand scheme of Zodiacal corrections, and as such, an idea for future IPD models could be to fit these L4 and L5 cloud components to actual data to see if there is any significant dust concentration present, or even simply look for similar patterns in high-frequency residual maps.

7.5 Quadrature efficiency

As previously stressed, a critical aspect of BeyondPlanck's component separation software is the computational efficiency of the internal modules. It is, therefore, important that we find a balance between the precision of our calculations and the time spent by the Zodiacal Emission module. We can directly affect the computation time of the module through the following:

1. LOS resolution. Most of the calculations in the module are done step-wise along the LOS, meaning that the time spent by the module scales linearly with N_{LOS}, the number of points along the LOS.

2. Quadrature selection. The two methods of numerical integration we are considering for the module are the trapezoidal rule and Simpson's rule. We expect the trapezoidal rule to be slightly faster than the Simpson's rule; it requires one less evaluation per step along the LOS which could become a significant time-saver when applied to the full BP data set. On the other hand, Simpson's rule is a more accurate method and could perhaps make our results converge on sufficiently accurate estimates for lower values of N_{LOS}, which in turn would save time.

We will now perform a study to determine the ideal relationship between a method of quadrature and a value of N_{LOS}. For this purpose, we produce a set of Zodiacal component maps with both methods of quadrature over a wide range of N values. Naturally, we expect these maps to become more precise with increasing values of N_{LOS} (hereby referred to as just N), and as such, we somewhat arbitrarily select a sufficiently large value of $N = 2000$ to represent a resolution where each component is sufficiently resolved. For each Zodiacal component, we compare the maximum precision map, and a map of lower precision by computing the relative error between the two maps. We define the relative error between two maps as the pixel averaged relative error

$$\mathrm{E_r}^N = \frac{1}{P}\sum_{p=1}^{P}\frac{\mathbf{M}_p^{N=2000} - \mathbf{M}_p^N}{\mathbf{M}_p^{N=2000}}. \tag{7.3}$$

Here, $\mathbf{M}_p^N$ is the value of pixel p in map $\mathbf{M}^N$, evaluated at a resolution N, and P is the total number of pixels in the maps.

Only three out of the six Zodiacal component maps exhibit a non-negligible signal over the full sky, those being the Diffuse Cloud, the Circumsolar Ring, and the Earth-trailing Feature. In the case with the Dust Bands, most of the pixels in the maps have values very close to zero, dictated by integration noise only. Comparing this noise between maps would result in large relative errors. As such, we have carefully masked

Table 7.1: Comparison of quadrature and line-of-sight resolution for our Zodiacal Emission module.

N	Cloud	Band 1	Band 2	Band 3	Ring	Feature
Trapezoidal rule						
Pixel averaged relative error, E_r, in percentage						
10	4.1709×10^{0}	7.0681×10^{0}	3.3870×10^{0}	6.9977×10^{0}	1.4229×10^{2}	1.4760×10^{2}
20	6.2141×10^{-1}	1.1775×10^{0}	6.4633×10^{-1}	1.2221×10^{0}	4.6161×10^{1}	4.1658×10^{1}
50	1.2481×10^{-1}	3.9026×10^{-1}	1.4836×10^{-1}	4.0865×10^{-1}	6.4729×10^{0}	6.1526×10^{0}
100	4.6062×10^{-2}	1.8870×10^{-1}	6.5653×10^{-2}	1.9759×10^{-1}	1.4964×10^{0}	1.4049×10^{0}
200	1.8917×10^{-2}	8.9051×10^{-2}	2.9694×10^{-2}	9.3244×10^{-2}	4.1745×10^{-1}	3.4902×10^{-1}
500	5.8938×10^{-3}	2.9615×10^{-2}	9.6177×10^{-3}	3.1011×10^{-2}	7.2046×10^{-2}	5.4917×10^{-2}
1000	1.9395×10^{-3}	9.8623×10^{-3}	3.1685×10^{-3}	3.1011×10^{-2}	1.5246×10^{-2}	1.1346×10^{-2}
Time spent [sec]						
10	33.42	31.59	31.93	31.45	30.84	30.65
20	37.16	33.90	34.31	33.94	31.33	31.92
50	49.57	44.08	45.03	42.69	35.81	39.81
100	73.72	63.38	66.21	60.74	44.25	46.56
200	124.39	104.31	114.74	99.66	64.64	68.54
500	280.52	241.08	257.27	222.22	131.49	139.40
1000	546.04	457.09	501.50	429.03	245.07	260.28
2000	1074.27	896.83	988.17	844.15	477.14	508.07
Simpson's rule						
Pixel averaged relative error, E_r, in percentage						
10	3.7066×10^{0}	3.8183×10^{0}	5.6425×10^{0}	3.7341×10^{0}	7.4966×10^{1}	8.6284×10^{1}
20	9.5912×10^{-1}	1.9550×10^{0}	1.0097×10^{0}	1.9640×10^{0}	3.0403×10^{1}	1.2680×10^{1}
50	9.8040×10^{-2}	5.2292×10^{-1}	1.8070×10^{-1}	5.4594×10^{-1}	2.7104×10^{0}	9.3956×10^{-1}
100	4.9172×10^{-2}	2.5128×10^{-1}	8.0256×10^{-2}	2.6311×10^{-1}	7.2490×10^{-1}	3.7432×10^{-1}
200	2.3051×10^{-2}	1.1864×10^{-1}	3.7764×10^{-2}	1.2423×10^{-1}	2.6506×10^{-1}	1.2588×10^{-1}
500	7.6762×10^{-3}	3.9472×10^{-2}	1.2560×10^{-7}	4.1333×10^{-2}	5.2865×10^{-2}	2.4174×10^{-2}
1000	2.5575×10^{-3}	1.3146×10^{-2}	4.1831×10^{-7}	1.3769×10^{-2}	1.5503×10^{-2}	7.3350×10^{-3}
Time spent [sec]						
10	33.43	31.66	32.28	31.43	31.21	31.23
20	36.57	33.86	34.56	33.14	32.30	30.98
50	49.24	44.06	45.67	42.77	36.63	36.52
100	72.67	62.76	66.42	60.43	44.38	46.09
200	123.86	105.88	112.70	99.44	64.62	67.76
500	283.55	239.60	258.37	291.56	132.29	139.58
1000	548.58	460.96	501.86	434.23	247.46	261.89
2000	1085.98	903.06	998.97	862.44	477.92	514.21

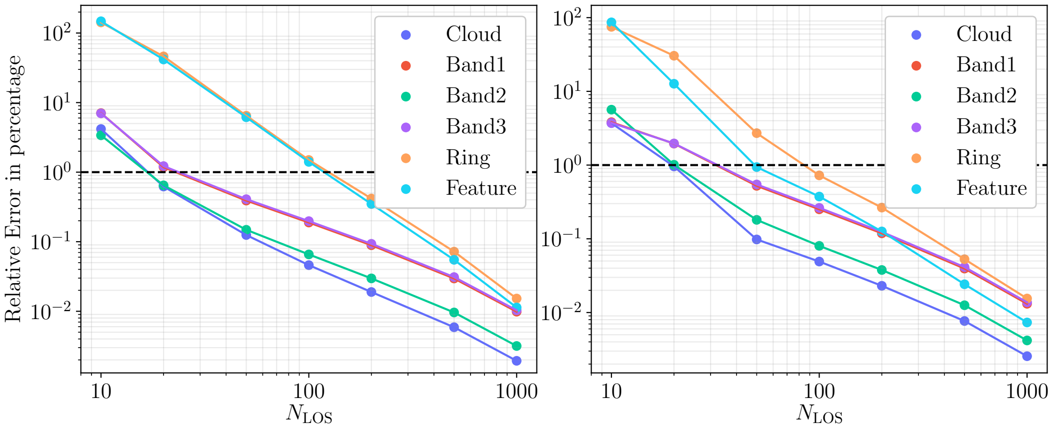

Figure 7.18: Percentage relative errors in each Zodiacal component map when using the trapezoidal rule (left), and Simpson's rule (right). The black stapled line highlights the 1% relative error cut-off.

out pixels that do not significantly contribute to the total sky brightening for all three Dust Bands. The results of the study can be seen in Table 7.1 which shows the averaged relative error, $\mathrm{E_r}$, as well as the total time spent by the ZLE module to compute each map. The tabulated values are plotted in Figure 7.18.

In the left subfigure, we see the percentage relative errors in each Zodiacal component map when using the trapezoidal rule. We have included a black stapled line to highlight the 1% relative error cut-off, which we believe represents a sufficient accuracy threshold for the templates. The Diffuse Cloud and Dust Band 2 appear to be the two best-resolved components. They follow a similar curve on the plot, which makes sense as these are both components with significant densities along the entire line-of-sight. Dust Bands 1 and 3 are very similar in terms of their density distribution. They also share a common peak density position. As such, these components are for all computational purposes equivalent and therefore follow the same curve in the figure. We expect the Circumsolar Ring and Earth-trailing Feature to be the hardest components to resolve as these are very sharply defined along a given line-of-sight. This is evident in our results, as both components start with errors larger than 150%. In general, the trapezoidal rule appears to do a great job of resolving the Diffuse Cloud and Dust Bands, which are all confidently below the 1% threshold at $N = 50$. On the other hand, the method seems to struggle with the Circumsolar Ring and the Earth-trailing Feature, which requires an additional 150 evaluations per line-of-sight.

The right subfigure shows the relative errors in percentage when using Simpson's rule. In general, this method appears to do a worse job of resolving the Diffuse Cloud and the Dust Bands. On the other hand, it does a significantly better job of resolving the Circumsolar Ring and the Earth-trailing Feature, which are both found below the 1% threshold at $N = 100$. It is apparent from the tabulate time that the advantage of using a lower N highly outweighs the difference in time spent by the two methods. Simpson's method allows us to resolve all components to the 1% threshold at a significantly lower value of N, and will, therefore, be the standard method used by the ZLE module. Although, if the BeyondPlanck emissivity fits results in inconclusive results, similar to the case of the *Planck* analysis, and the Circumsolar Ring and Earth-trailing Feature are again rejected, the trapezoidal method could be utilized instead with the benefit of a value of N as low as $N \approx 25$.

7.6 Further optimization of the Zodiacal Emission module and BeyondPlanck HFI analysis forecast

There are several possible improvements to the module in terms of computational efficiency. One idea is to evaluate the IPD model at a lower map resolution and then interpolate to each observation. This would significantly cut down the computation time, which is directly proportional to the number of pixels evaluated on a map. A similar approach could be applied to the line-of-sight integration method, where we evaluate the IPD model at lower resolution line-of-sight grids and again interpolate, although this could prove to be problematic in resolving the Circumsolar Ring and Earth-trailing Feature, which are sharply defined along the line-of-sight.

These optimization methods must be addressed before the BeyondPlanck HFI analysis takes place to make sure that the Zodiacal Emission module functions at maximum efficiency. The module is expected to spend significantly more computation time with the coming HFI analysis due to the higher sampling rate of the HFI. The sampling rate of the instruments is influenced by the spin rate of the satellite and the detector beams. Both the HFI and the LFI naturally spins at the same rate along with *Planck*, but HFI has significantly smaller beams, meaning that it samples data at a much higher frequency. Not only does this result in a larger data volume for HFI, despite only having observed over two years, but the data comes in at a much higher resolution. HFI analysis is typically performed at $N_{\mathrm{side}} = 2048$ or even 4096 for the highest frequency channels compared to the $N_{\mathrm{side}} = 512$ for LFI. Such an increase in resolution has great implications for our module, which calculates the emission pixel by pixel meaning that it will have to consider 10-100 times more pixels than during the LFI testing.

7.7 Gallery of frequency templates

The following 3 pages contain the estimated ZLE frequency templates for the full HFI mission computed with the *Planck* 2018 Zodiacal emissivities. These are our best estimates of the ZLE as seen by *Planck* during the full HFI mission, limited by differences in pointing information, map resolution, sky coverage, and a Zodiacal emissivity fits.

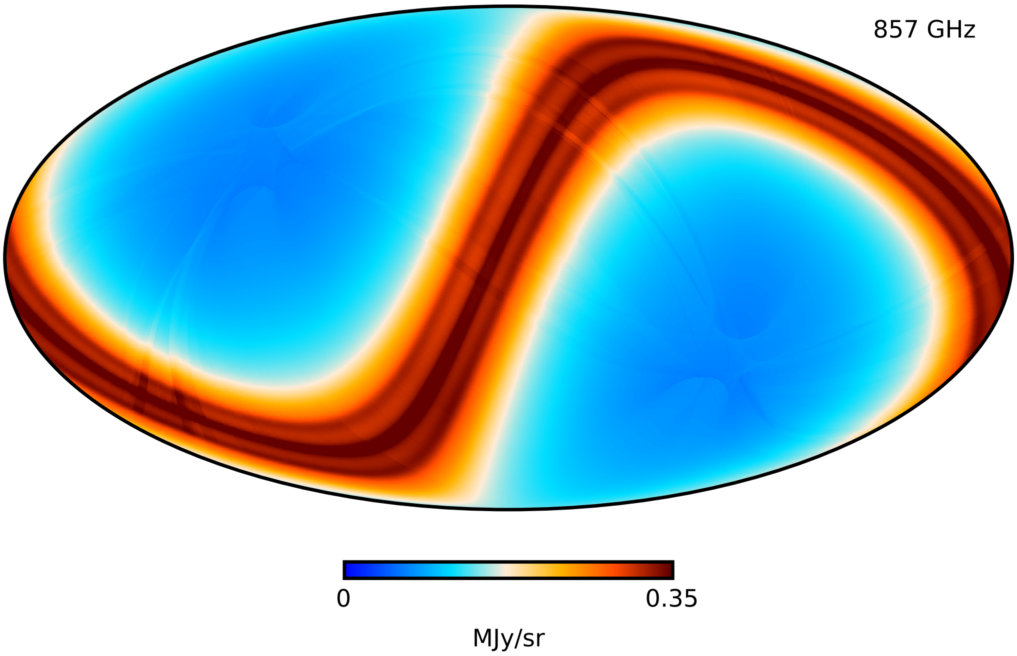

Figure 7.19: ZLE template for 857 GHz produced by our Zodiacal Emission module with the *Planck* 2018 emissivity fits.

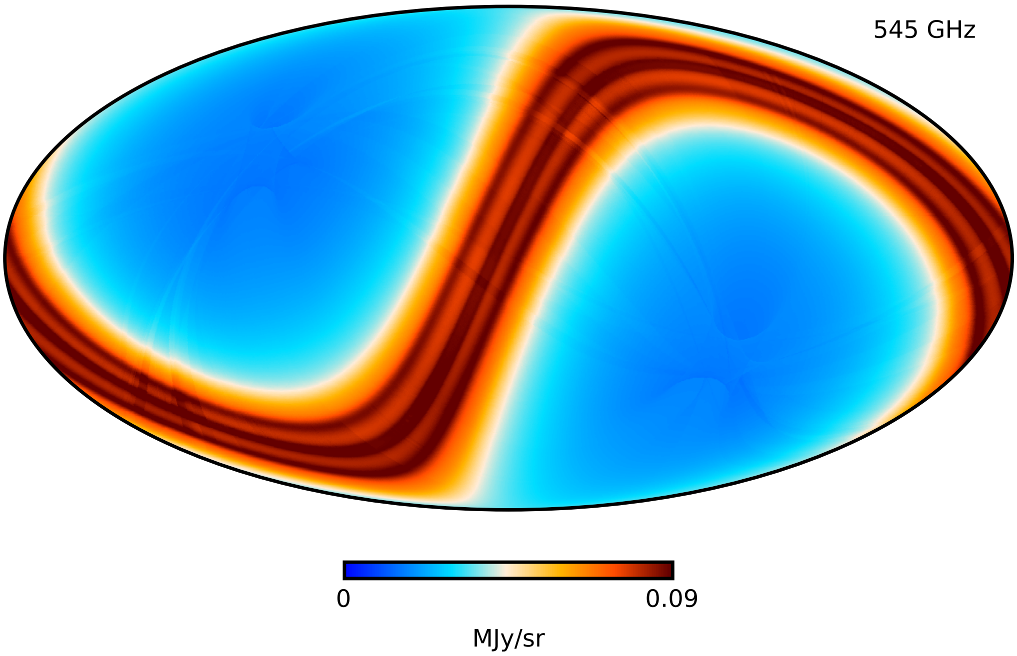

Figure 7.20: ZLE template for 545 GHz produced by our Zodiacal Emission module with the *Planck* 2018 emissivity fits.

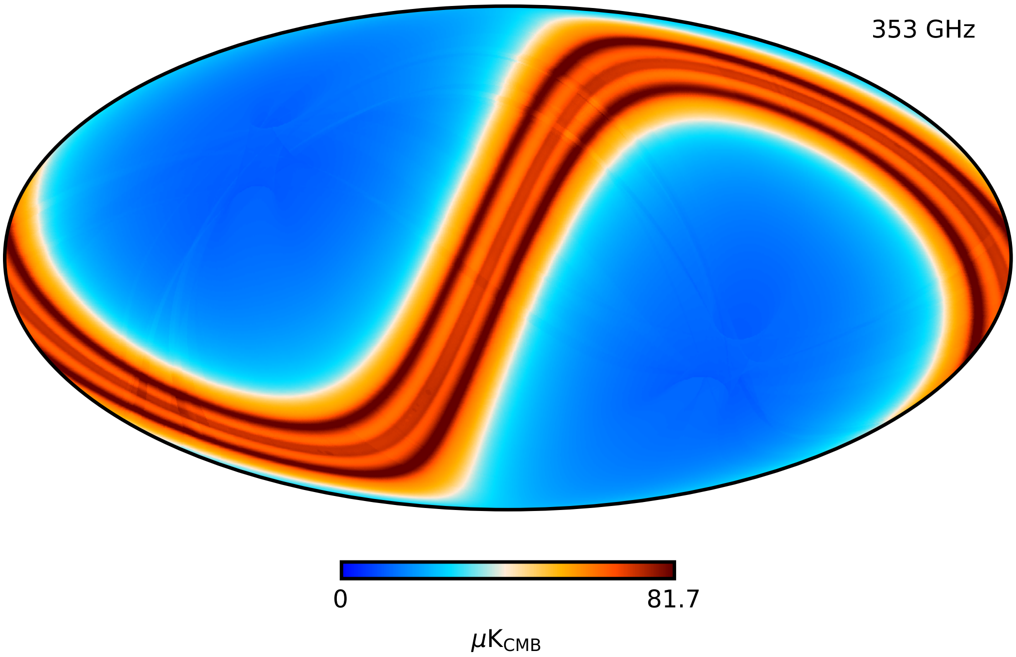

Figure 7.21: ZLE template for 353 GHz produced by our Zodiacal Emission module with the *Planck* 2018 emissivity fits.

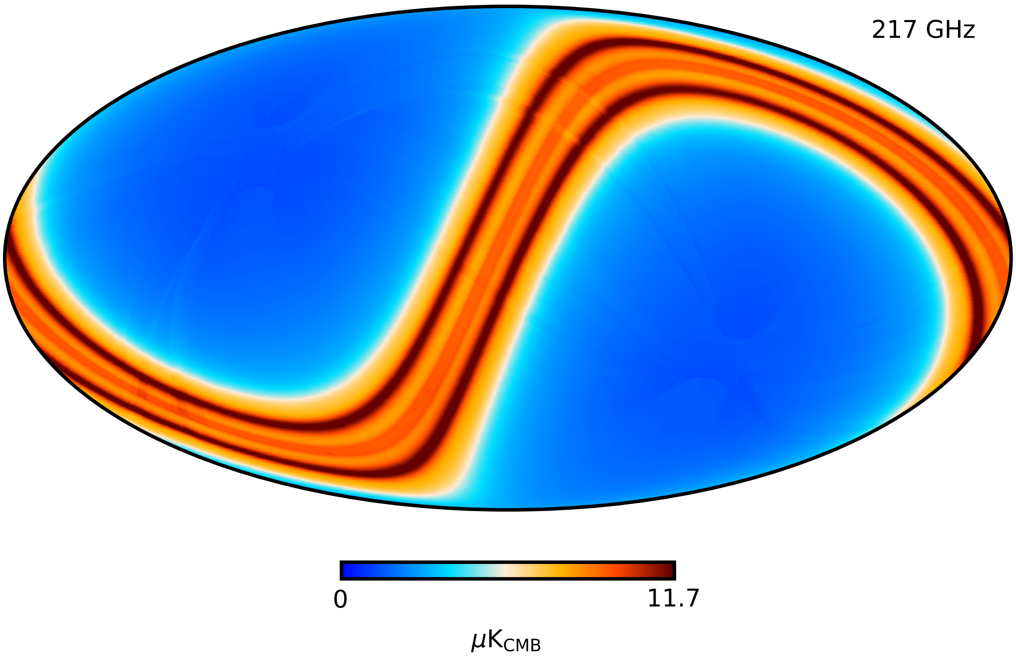

Figure 7.22: ZLE template for 217 GHz produced by our Zodiacal Emission module with the *Planck* 2018 emissivity fits.

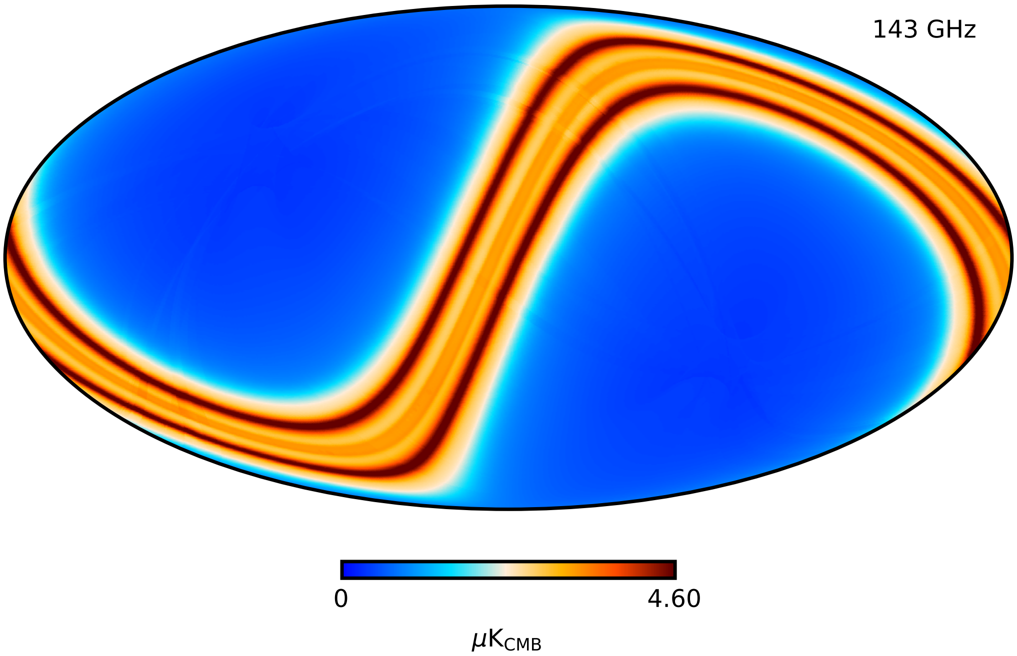

Figure 7.23: ZLE template for 143 GHz produced by our Zodiacal Emission module with the *Planck* 2018 emissivity fits.

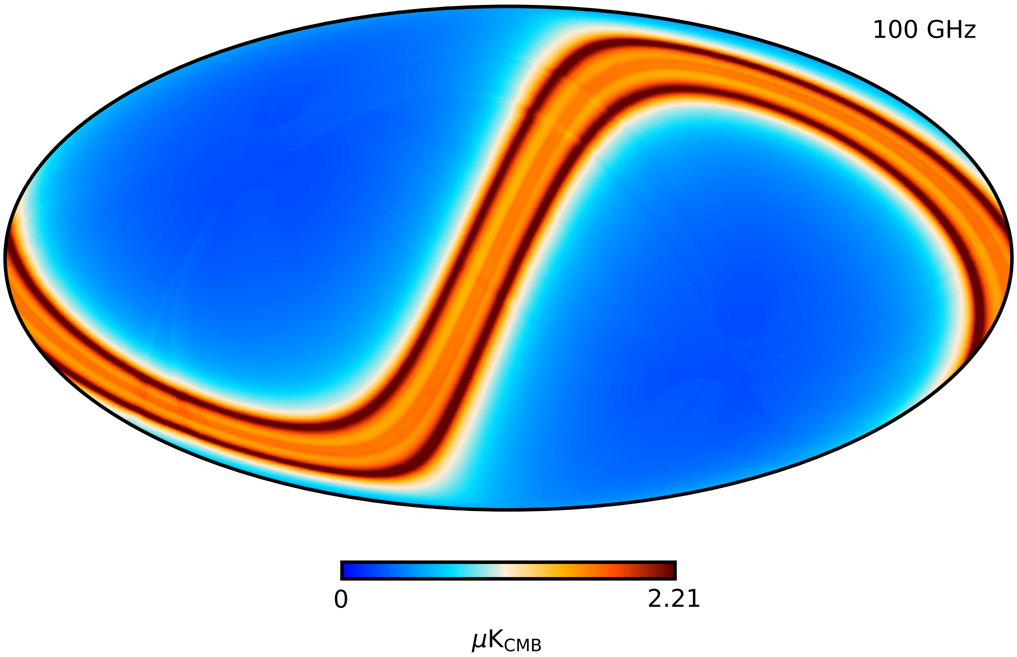

Figure 7.24: ZLE template for 100 GHz produced by our Zodiacal Emission module with the *Planck* 2018 emissivity fits.

Chapter 8

Conclusion and Future Prospects

In this thesis, we have implemented a flexible and computationally efficient method of performing highly accurate Zodiacal correction to high-frequency cosmological data. By adopting the K98 Interplanetary Dust model and translating it to the time-ordered domain, our BeyondPlanck Zodiacal Emission module is effectively able to estimate the observed Zodiacal emission over most sets of time-ordered data. While the lack of HFI pointing information limits the precision of our estimates, we find that our Zodiacal Emission maps are consistent with the templates produced by the *Planck* collaboration, differing only slightly in the overall signal amplitude.

8.1 Conclusion

Estimating the Zodiacal emission in high-frequency cosmological data is a comprehensive process. The time-dependent nature of the signal requires the evaluation of a dynamic three-dimensional model of the Interplanetary Dust distribution used to estimate the emission in a line-of-sight from an observer. Previously, the BeyondPlanck machinery `Commander` has performed Zodiacal corrections using fixed templates of the estimated Zodiacal Emission. The problem with this approach is that due to the temporal variance of the emission, such a template is strictly only valid if applied to the exact section of data for which it was created. We have, therefore, built a Zodiacal Emission module where we have adopted the K98 IPD model as implemented by *Planck* collaboration, and translated it to the time-ordered domain to be used in the coming BeyondPlanck HFI analysis.

The main benefit of our module is that it can be applied to any section of a time-ordered data set, considered by BeyondPlanck, to produce an accurate representation of the ZLE observed in real-time during component separation. Not only does this allow us to better estimate the ZLE, but we are also provided with information about the polarization leakage, which we believe to be a critical step to obtain "cleaner" CMB maps in both temperature and polarization from high-frequency data.

We have tested the module with satellite and pointing information from the 30 GHz LFI data set for which we have obtained maps that accurately reproduce the templates used to perform Zodiacal corrections by *Planck*. The main concern with our results is that the unit normalized emission amplitudes of the Zodiacal components tend to be slightly weaker than the *Planck* counterparts. We believe that these differences are mainly related to our approximation of using the LFI data and pointing information, but it could also be the result of generally more accurate estimation. It is unclear how the overall emission amplitudes will end up once we perform new fits of the Zodiacal emissivities with the HFI data.

The framework of our Zodiacal Emission module has allowed us to consider potential inclusions to the IPD model. Based on recent findings regarding IPD and asteroid discoveries, we have reason to believe that there could exist further concentrations to the dust in the Circumsolar Ring similar to the Earth-trailing Feature, specifically at the Sun-Earth Lagrangian points L4 and L5. We have performed a simple simulation to test the significance of such enhancements to the overall ZLE by adding oval formed clouds to the dust distribution in these regions. Our findings suggest that enhancements of magnitudes similar to the Earth-trailing Feature would contribute with emission three orders of magnitude smaller than the overall ZLE at the same frequency, and is, therefore, unlikely to play any significant role in Zodiacal corrections with current IPD models.

8.2 Future improvements to the K98 IPD model

The K98 IPD model has had a reputation of being an older model with uncertainties related to the model parameters as these were fit using DIRBE data. Despite its reputation, the model has proven successful in Zodiacal corrections in recent CMB analysis. We believe that the model in combination with the *Planck* approach of using Zodiacal emissivities to fit the emission to data is both a practical and precise method of estimating the emission without the need for a complicated description of the IPD distribution. There is, however, some validity to the criticism of the model. To better constrain the Zodiacal components in terms of their densities and geometry, we recommend that the K98 model parameters are re-estimated in future studies using more detailed cosmological high-frequency data. Such a fit could be performed along with the BeyondPlanck reprocessing of *Planck* HFI and DIRBE data jointly, as these data cover both ends of the thermal dust spectrum.

Part IV

Appendices

Appendix A

Fortran implementation of the Zodiacal Emission module

The code for our Zodiacal Emission module as implemented in `Commander` is shown over the following 13 pages:

```fortran
module comm_zodi_mod
    !   """
    !   Module which returns the Zodiacal Light Emission computed for a given
    !   chunk of time-ordered data.
    !
    !   Main Methods
    !   ------------
    !   initialize_zodi_mod(cpar)
    !       Initializes the zodi_mod. Pre-computes galactic to ecliptic
    !       pixel coordinates, and initializes Zodiacal components.
    !   compute_zodi_template(nside, pix, nu, s_zodi)
    !       Routine which calculates and returns the zodiacal emission over
    !       a line-of-sight for a chunck of time-ordered data at a given
    !       frequency nu.
    !
    !   """
    use comm_utils
    use comm_param_mod
    implicit none

    private
    public :: initialize_zodi_mod, compute_zodi_template

    integer(i4b)                                :: n_LOS
    real(dp)                                    :: T0, T0_inv, delta, delta2
    real(dp)                                    :: const1, const2
    real(dp)                                    :: R_max, R_sat
    real(dp), dimension(:), allocatable :: x, y, z
    real(dp), dimension(:), allocatable :: zodi_density, blackbody_emission
    real(dp), dimension(:), allocatable :: zodi_emission, tabulated_emission


    ! ==========================================================================
    !                           ZodiComponent Class Definition
    ! ==========================================================================
    type, abstract :: ZodiComponent
        ! Pointers to the next/prev links in the linked list
```

```fortran
        class(ZodiComponent), pointer :: nextLink => null()
        class(ZodiComponent), pointer :: prevLink => null()

        ! Shared component variables
        real(dp)                :: emissivity
        real(dp)                :: x0, y0, z0
        real(dp)                :: Incl, Omega
        real(dp), allocatable   :: sinOmega, cosOmega, sinIncl, cosIncl

        contains
            ! Shared component procedures
            procedure(init),     deferred :: initialize
            procedure(getDens), deferred :: getDensity

            ! Linked list procedures
            procedure :: next
            procedure :: add
    end type ZodiComponent

    abstract interface
        subroutine init(self)
            ! Routine which initializes and precomputes frequently used values
            ! for the a ZodiComponent.
            import dp, ZodiComponent
            class(ZodiComponent)  :: self
        end subroutine init

        subroutine getDens(self, x, y, z, density, lon)
            ! Routine which computes the density of a ZodiComponent at a
            ! given x, y, z coordinate.
            import i4b, dp, ZodiComponent
            class(ZodiComponent)                :: self
            real(dp), intent(in),  dimension(:) :: x, y, z
            real(dp), intent(out), dimension(:) :: density
            real(dp), intent(in),  optional     :: lon
            real(dp)                            :: xprime, yprime, zprime
            real(dp)                            :: R, Z_c
        end subroutine getDens
    end interface

    ! Sub components
    ! -------------------------------------------------------------------------
    type, extends(ZodiComponent) :: Cloud
        real(dp)  :: n0, alpha, beta, gamma, mu

        contains
            procedure :: initialize => initializeCloud
            procedure :: getDensity => getDensityCloud
    end type Cloud

    type, extends(ZodiComponent) :: Band
        real(dp)                :: n0, Dz, Dr, R0, Vi, Vr, P_i, P_r
        real(dp), allocatable   :: ViInv, DrInv, DzRinv

        contains
            procedure :: initialize => initializeBand
            procedure :: getDensity => getDensityBand
    end type Band

    type, extends(ZodiComponent) :: Ring
        real(dp)                :: nsr, Rsr, sigmaRsr, sigmaZsr
        real(dp), allocatable   :: sigmaRsr2Inv, sigmaZsrInv
```

```

        contains
            procedure :: initialize => initializeRing
            procedure :: getDensity => getDensityRing
    end type Ring

    type, extends(ZodiComponent) :: Feature
        real(dp)                :: ntf, Rtf, sigmaRtf, sigmaZtf, thetatf, &
                                   sigmaThetatf
        real(dp), allocatable   :: thetatfR,  sigmaRtfInv, sigmaZtfInv, &
                                   sigmaThetatfRinv
        contains
            procedure :: initialize => initializeFeature
            procedure :: getDensity => getDensityFeature
    end type Feature

    ! Initializing global ZodiComponent list and objects
    class(ZodiComponent), pointer :: comp_list => null()
    type(Cloud),          target  :: cloud_comp
    type(Band),           target  :: band1_comp, band2_comp, band3_comp
    type(Ring),           target  :: ring_comp
    type(Feature),        target  :: feature_comp

    ! Derived type which stores dynamically sized pixel coordinate maps
    ! ------------------------------------------------------------------------
    type Vector3D
        real(dp), dimension(:,:), allocatable :: elements
    end type Vector3D

    type RaggedArray
        type(Vector3D), dimension(:), allocatable :: vectors
    end type RaggedArray
    type(RaggedArray) :: coord_maps

contains
    ! ========================================================================
    !                          Main zodi_mod Routines
    ! ========================================================================
    subroutine initialize_zodi_mod(cpar)
        !   """
        !   Routine which initializes the zodi_mod. Galactic to ecliptic
        !   x,y,z coordinates are precomputed to reduce computation at later
        !   stages.
        !
        !   Arguments:
        !   ----------
        !   cpar: derived type
        !       Object containing parameters from the parameterfile.
        !
        !   """
        implicit none

        type(comm_params), intent(in)  :: cpar
        class(ZodiComponent), pointer  :: comp

        integer(i4b) :: i, j, npix, nside
        real(dp)     :: emissivity
        logical(lgt) :: use_cloud, use_band1, use_band2, use_band3, &
                        use_ring, use_feature, use_unit_emissivity
        real(dp), dimension(3)                  :: vec
        real(dp), dimension(3,3)                :: gal2ecl_matrix
        integer(i4b), dimension(:), allocatable :: ds_nside_unique, nside_unique
```

```
real(dp), dimension(:,:), allocatable   :: ecliptic_vec
real(dp), dimension(6) :: emissivity100, emissivity143, emissivity217, &
                          emissivity353, emissivity545, emissivity857

! Model parameters
! --------------------------------------------------------------------
! Temperature parameters
T0 = 286.d0
T0_inv = 1.d0/T0
delta = 0.46686260d0
delta2 = delta/2.d0

! Line-of-sight integration parameters
R_max = 5.2d0   ! max distance from the Sun [AU]
n_LOS = 100     ! integration steps

! Zodi component selection
use_cloud = .true.
use_band1 = .false.
use_band2 = .false.
use_band3 = .false.
use_ring = .false.
use_feature = .false.

use_unit_emissivity = .true.

! Emissivities  (cloud, band1, band2, band3, ring, feature)
! (working on a smarter fix for emissivity selection)
emissivity857 = (/0.256,  2.06 , 0.85, 3.37, 0.0, 0.0/)
emissivity545 = (/0.167, 1.74, 0.54 , 2.54, 0.0, 0.0/)
emissivity353 = (/0.106,  1.58, 0.39, 1.88, 0.0, 0.0/)
emissivity217 = (/0.051, 1.30, 0.15, 1.27, 0.0, 0.0/)
emissivity143 = (/0.022, 1.23,  0.15, 1.16, 0.0, 0.0/)
emissivity100 = (/0.012, 1.02, 0.08, 0.72, 0.0, 0.0/)

if (use_unit_emissivity == .true.) then
    emissivity = 1.d0
end if

! Initializing zodi components
! ------------------------------------
if (use_cloud == .true.) then
    if (use_unit_emissivity == .false.) then
        emissivity = emissivity100(1)
    end if
    cloud_comp = Cloud(emissivity=emissivity, x0=0.011887801d0, &
                       y0=0.0054765065d0, z0=-0.0021530908d0, &
                       Incl=2.0335188d0, Omega=77.657956d0, &
                       n0=1.1344374d-7, alpha=1.3370697d0, &
                       beta=4.1415004d0, gamma=0.94206179d0, &
                       mu=0.18873176d0)
    comp => cloud_comp
    call add2Complist(comp)
end if

if (use_band1 == .true.) then
    if (use_unit_emissivity == .false.) then
        emissivity = emissivity100(2)
    end if
    band1_comp = Band(emissivity=emissivity, x0=0.d0, y0=0.d0, z0=0.d0,&
                      Incl=0.56438265, Omega=80d0, n0=5.5890290d-10, &
                      Dz=8.7850534, Dr=1.5, R0=3.d0, Vi=0.1, Vr=0.05, &
```

```
                              P_i=4.d0, P_r=1.d0)
            comp => band1_comp
            call add2Complist(comp)
        end if

        if (use_band2 == .true.) then
            if (use_unit_emissivity == .false.) then
                emissivity = emissivity100(3)
            end if
            band2_comp = Band(emissivity=emissivity, x0=0.d0, y0=0.d0, z0=0.d0,&
                              Incl=1.2, Omega=30.347476, n0=1.9877609d-09, &
                              Dz=1.9917032, Dr=0.94121881, R0=3.d0, &
                              Vi=0.89999998, Vr=0.15, P_i=4.d0, P_r=1.d0)
            comp => band2_comp
            call add2Complist(comp)
        end if

        if (use_band3 == .true.) then
            if (use_unit_emissivity == .false.) then
                emissivity = emissivity100(4)
            end if
            band3_comp = Band(emissivity=emissivity, x0=0.d0, y0=0.d0, z0=0.d0,&
                              Incl=0.8, Omega=80.0, n0=1.4369827d-10,      &
                              Dz=15.0, Dr=1.5, R0=3.d0, Vi=0.05, Vr=-1.0, &
                              P_i=4.d0, P_r=1.d0)
            comp => band3_comp
            call add2Complist(comp)
        end if

        if (use_ring == .true.) then
            if (use_unit_emissivity == .false.) then
                emissivity = emissivity100(5)
            end if
            ring_comp = Ring(emissivity=emissivity, x0=0.d0, y0=0.d0, z0=0.d0, &
                             Incl=0.48707166d0, Omega=22.27898d0, &
                             nsr=1.8260528d-8, Rsr=1.0281924d0, &
                             sigmaRsr=0.025d0, sigmaZsr=0.054068037d0)
            comp => ring_comp
            call add2Complist(comp)
        end if

        if (use_feature == .true.) then
            if (use_unit_emissivity == .false.) then
                emissivity = emissivity100(6)
            end if
            feature_comp = Feature(emissivity=emissivity, x0=0.d0, y0=0.d0, &
                                   z0=0.d0, Incl=0.48707166d0, &
                                   Omega=22.27898d0, ntf=2.0094267d-8, &
                                   Rtf=1.0579183d0, sigmaRtf=0.10287315d0, &
                                   sigmaZtf=0.091442964d0, thetatf=-10.d0, &
                                   sigmaThetatf=12.115211d0)
            comp => feature_comp
            call add2Complist(comp)
        end if

        ! Executes initialization routines for all activated components
        comp => comp_list
        do while (associated(comp))
            call comp%initialize()
            comp => comp%next()
        end do

```

```
        ! Allocating line-of-sight related arrays
        allocate(x(n_LOS+1))
        allocate(y(n_LOS+1))
        allocate(z(n_LOS+1))
        allocate(zodi_density(n_LOS+1))
        allocate(blackbody_emission(n_LOS+1))
        allocate(zodi_emission(n_LOS+1))

        ! Precomputing ecliptic to galactic coordinates per pixels for all
        ! relevant nsides
        ! -------------------------------------------------------------------

        ! Get all unique LFI nsides from cpar (This part should be updated when
        ! BeyondPlanck moves on to using HFI data)
        allocate(ds_nside_unique(cpar%numband))
        j = 0
        do i = 1, cpar%numband
            if (trim(cpar%ds_tod_type(i)) /= 'none') then
                if (any(ds_nside_unique /= cpar%ds_nside(i))) then
                    j = j + 1
                    ds_nside_unique(j) = cpar%ds_nside(i)
                end if
            end if
        end do

        allocate(coord_maps%vectors(j))
        allocate(nside_unique(j))
        do i = 1, j
            nside_unique(i) = ds_nside_unique(i)
        end do
        deallocate(ds_nside_unique)

        ! Getting pixel coordinates through HEALPix pix2vec_ring for each
        ! relevant nside
        call getEcl2GalMatrix(gal2ecl_matrix)
        do i = 1, size(nside_unique)
            nside = nside_unique(i)
            npix = nside2npix(nside)
            allocate(tabulated_emission(npix))
            allocate(coord_maps%vectors(i)%elements(npix,3))
            allocate(ecliptic_vec(npix,3))

            do j = 0, npix-1
                call pix2vec_ring(nside, j, vec)
                ecliptic_vec(j+1,1) = vec(1)
                ecliptic_vec(j+1,2) = vec(2)
                ecliptic_vec(j+1,3) = vec(3)
            end do

            ! Transforming to ecliptic coordinates
            coord_maps%vectors(i)%elements = matmul(ecliptic_vec,gal2ecl_matrix)
            deallocate(ecliptic_vec)
        end do

    end subroutine initialize_zodi_mod

    subroutine compute_zodi_template(nside, pix, sat_pos, nu, s_zodi)
        !   """
        !   Routine which computes the Zodiacal Light Emission at a given nside
        !   resolution for a chunk of time-ordered data.
        !
        !   Arguments:
```

```
        !   ----------
        !   nside: int
        !       Map grid resolution.
        !   pix: array
        !       Pixel array containing the pixels from which to compute the
        !       zodi signal with dimensions (n_tod, n_det)
        !   sat_pos: real
        !       Satellite longitude and latitude for given time-order data chunk
        !   nu: array
        !       Array containing the all detectors with dimension (n_det)
        !
        !   Returns:
        !   --------
        !   s_zodi: array
        !       Zodiacal emission for current time-ordered data chunk
        !       with dimensions (n_tod, n_det)
        !
        !   """
        implicit none

        class(ZodiComponent), pointer :: comp

        integer(i4b),                        intent(in)  :: nside
        integer(i4b), dimension(1:,1:), intent(in)  :: pix
        real(dp),     dimension(3),     intent(in)  :: sat_pos
        real(dp),     dimension(1:),    intent(in)  :: nu
        real(sp),     dimension(1:,1:), intent(out) :: s_zodi

        integer(i4b) :: i, j, k, n_det, n_tod, pixnum
        real(dp)     :: x0, y0, z0, x1, y1, z1, dx, dy, dz
        real(dp)     :: longitude_sat, latitude_sat
        real(dp)     :: u_x, u_y, u_z
        real(dp)     :: s, ds
        real(dp)     :: R_squared, R_cos_theta, R_LOS
        real(dp)     :: integral
        real(dp), dimension(:,:), allocatable :: coord_map

        ! Resetting quantities for each new TOD chunck
        s_zodi = 0.d0
        zodi_density = 0.d0
        blackbody_emission = 0.d0
        zodi_emission = 0.d0

        ! Extracting n time-orderd data and n detectors for current chunk
        n_tod = size(pix,1)
        n_det = size(pix,2)

        ! Selecting coordinate map containing heliocentric pixel unit vectors
        coord_map = getCoordMap(nside)

        ! Observer position information
        x0 = sat_pos(1)
        y0 = sat_pos(2)
        z0 = sat_pos(3)
        longitude_sat = atan2(y0,x0)

        ! Computing the zodiacal emission for current time-ordered data chunk
        do j = 1, n_det
            ! Computing terms in Planck's law for blackbody emission
            const1 = (2.d0*h*nu(j)**3)/(c**2)
            const2 = (h*nu(j))/k_B

```

```fortran
! Initializing tabulated zodi values
tabulated_emission = 0.d0

do i = 1, n_tod
    ! Current pixel
    pixnum = pix(i,j)

    if (tabulated_emission(pixnum) == 0.d0) then
        ! The first time a pixel is hit in the TOD chunk we compute
        ! the ZLE and tabulate for future hits in the same chunk

        ! Looking up heliocentric unit vectors
        u_x = coord_map(pixnum,1)
        u_y = coord_map(pixnum,2)
        u_z = coord_map(pixnum,3)

        ! Finding the coordinates (x1, y1, z1) at the end of the
        ! line-of-sight
        R_squared = x0**2 + y0**2 + z0**2
        R_cos_theta = x0*u_x + y0*u_y + z0*u_z
        R_LOS = -R_cos_theta+sqrt(R_cos_theta**2-R_squared+R_max**2)

        x1 = x0 + R_LOS*u_x
        y1 = y0 + R_LOS*u_y
        z1 = z0 + R_LOS*u_z

        ! Constructing line-of-sight array
        dx = (x1-x0)/(n_LOS-1)
        dy = (y1-y0)/(n_LOS-1)
        dz = (z1-z0)/(n_LOS-1)
        ds = sqrt(dx**2 + dy**2 + dz**2)

        do k = 1, n_LOS+1
            x(k) = x0 + (k-1)*dx
            y(k) = y0 + (k-1)*dy
            z(k) = z0 + (k-1)*dz

            ! Radial distance from the Sun
            s = x(k)**2 + y(k)**2 + z(k)**2

            ! Blackbody emission at a distance s from the Sun
            blackbody_emission(k) = &
                    const1/(exp(const2*(s**delta2)*T0_inv) - 1.d0)
        end do

        comp => comp_list
        do while (associated(comp))

            ! Compute density of component at celestial coordinate
            call comp%getDensity(x,y,z, zodi_density, longitude_sat)
            zodi_emission = zodi_density*blackbody_emission

            ! Integrate emission along the line-of-sight
            call simpsons(zodi_emission, ds, n_LOS, integral)

            s_zodi(i,j) = s_zodi(i,j) + integral*comp%emissivity

            comp => comp%next()
        end do

        ! Saving emission and storing for future reference
        tabulated_emission(pixnum) = s_zodi(i,j)
```

```

                else
                    ! Looking up tabulated emission
                    s_zodi(i,j) = s_zodi(i,j) + tabulated_emission(pixnum)
                end if

            end do
        end do
    end subroutine compute_zodi_template

    ! =========================================================================
    !                         Functions and subroutines
    ! =========================================================================
    subroutine getEcl2GalMatrix(matrix)
        ! Ecliptic to galactic rotation matrix
        implicit none
        real(dp), dimension(3,3) :: matrix

        matrix(1,1) =  -0.054882486d0
        matrix(1,2) =  -0.993821033d0
        matrix(1,3) =  -0.096476249d0
        matrix(2,1) =   0.494116468d0
        matrix(2,2) =  -0.110993846d0
        matrix(2,3) =   0.862281440d0
        matrix(3,1) =  -0.867661702d0
        matrix(3,2) =  -0.000346354d0
        matrix(3,3) =   0.497154957d0
    end subroutine getEcl2GalMatrix

    function getCoordMap(nside) result(coord_map)
        ! Routine which selects coordinate transformation map based on resolution
        implicit none

        integer(i4b), intent(in) :: nside

        integer(i4b)                           :: i, j, npix
        real(dp), dimension(:,:), allocatable  :: coord_map

        npix = nside2npix(nside)
        do i = 1, size(coord_maps%vectors)
            if (size(coord_maps%vectors(i)%elements(:,1)) == npix) then
                coord_map = coord_maps%vectors(i)%elements
                j = 1
            end if
        end do

        if (j /= 1) then
            print *, "ERROR: Could not get coordinate map for nside:", &
                  nside ,"(comm_zodi_mod)"
            print *, "Exiting run."
            call exit(0)
        end if
    end function getCoordMap

    subroutine trapezoidal(f, ds, n, result)
        ! Trapezoidal integration method
        implicit none

        real(dp), dimension(:), intent(in) :: f
        integer(i4b), intent(in)           :: n
        real(dp), intent(in)               :: ds
```

```fortran
        real(dp), intent(out)              :: result

        result = 0.5*f(1) + 0.5*f(n+1)
        result = result + sum(f(2:n))
        result = result*ds
    end subroutine trapezoidal

    subroutine simpsons(f, ds, n, result)
        ! Simpsons integration rule
        implicit none

        real(dp), dimension(:), intent(in) :: f
        integer(i4b), intent(in)           :: n
        real(dp), intent(in)               :: ds
        real(dp), intent(out)              :: result
        integer(i4b)                       :: i
        result = f(1) + f(n+1)
        do i = 2, n-2, 2
            result = result + 4.d0*f(i) + 2.d0*f(i+1)
        end do
        result = (result + 4.d0*f(n))*(ds/3.d0)
    end subroutine simpsons

    ! =========================================================================
    !                         Zodi Components Routines
    ! =========================================================================
    subroutine initializeCloud(self)
        implicit none
        class(Cloud) :: self

        self%sinOmega = sin(self%Omega * deg2rad)
        self%cosOmega = cos(self%Omega * deg2rad)
        self%sinIncl = sin(self%Incl * deg2rad)
        self%cosIncl = cos(self%Incl * deg2rad)
    end subroutine initializeCloud

    subroutine getDensityCloud(self, x, y, z, density, lon)
        implicit none

        class(Cloud) :: self
        real(dp), dimension(:), intent(in)  :: x, y, z
        real(dp), dimension(:), intent(out) :: density
        real(dp), intent(in), optional      :: lon

        integer(i4b) :: i
        real(dp)     :: R, Z_c, zeta, g
        real(dp)     :: xprime, yprime, zprime

        do i = 1, n_LOS
            xprime = x(i) - self%x0
            yprime = y(i) - self%y0
            zprime = z(i) - self%z0

            R = sqrt(xprime**2 + yprime**2 + zprime**2)
            Z_c = (xprime*self%sinOmega - yprime*self%cosOmega)*self%sinIncl &
                + zprime*self%cosIncl

            zeta = abs(Z_c)/R
            if (zeta < self%mu) then
                g = (zeta**2)/(2.d0*self%mu)
            else
                g = zeta - (0.5 * self%mu)
```

```
            end if

            density(i) = self%n0 * R**(-self%alpha) * exp(-self%beta &
                    * g**self%gamma)
        end do
    end subroutine getDensityCloud

    subroutine initializeBand(self)
        implicit none
        class(Band) :: self

        self%ViInv = 1.d0/self%Vi
        self%DrInv = 1.d0/self%Dr
        self%DzRInv = 1.d0/(self%Dz * deg2rad)
        self%sinOmega = sin(self%Omega * deg2rad)
        self%cosOmega = cos(self%Omega * deg2rad)
        self%sinIncl = sin(self%Incl * deg2rad)
        self%cosIncl = cos(self%Incl * deg2rad)
    end subroutine initializeBand

    subroutine getDensityBand(self, x, y, z, density, lon)
        implicit none

        class(Band) :: self
        real(dp), dimension(:), intent(in)  :: x, y, z
        real(dp), dimension(:), intent(out) :: density
        real(dp), intent(in), optional      :: lon

        integer(i4b) :: i
        real(dp) :: xprime, yprime, zprime
        real(dp) :: R, Z_c
        real(dp) :: zeta, ZDz, ZDz2, ZDz4, ZDz6, ViTerm, WtTerm

        do i = 1, n_LOS
            xprime = x(i) - self%x0
            yprime = y(i) - self%y0
            zprime = z(i) - self%z0

            R = sqrt(xprime*xprime + yprime*yprime + zprime*zprime)
            Z_c = (xprime*self%sinOmega - yprime*self%cosOmega)*self%sinIncl &
                + zprime*self%cosIncl
            zeta = abs(Z_c)/R
            ZDz = zeta * self%DzRInv
            ZDz2 = ZDz * ZDz
            ZDz4 = ZDz2 * ZDz2
            ZDz6 = ZDz4 * ZDz2
            ViTerm = 1.d0 + ZDz4 * self%ViInv
            WtTerm = 1.d0 - exp(-(R*self%DrInv)**20)

            density(i) = self%n0 * exp(-ZDz6) * ViTerm * WtTerm * self%R0/R
        end do
    end subroutine getDensityBand

    subroutine initializeRing(self)
        implicit none
        class(Ring) :: self

        self%sigmaRsr2Inv = 1.d0 / (self%sigmaRsr * self%sigmaRsr)
        self%sigmaZsrInv = 1.d0 / self%sigmaZsr
        self%sinOmega = sin(self%Omega * deg2rad)
        self%cosOmega = cos(self%Omega * deg2rad)
        self%sinIncl = sin(self%Incl * deg2rad)
```

```fortran
        self%cosIncl = cos(self%Incl * deg2rad)
    end subroutine initializeRing

    subroutine getDensityRing(self, x, y, z, density, lon)
        implicit none

        class(Ring) :: self
        real(dp), dimension(:), intent(in)  :: x, y, z
        real(dp), dimension(:), intent(out) :: density
        real(dp), intent(in), optional      :: lon

        integer(i4b) :: i
        real(dp) :: xprime, yprime, zprime
        real(dp) :: R, Z_c

        do i = 1, n_LOS
            xprime = x(i) - self%x0
            yprime = y(i) - self%y0
            zprime = z(i) - self%z0

            R = sqrt(xprime*xprime + yprime*yprime + zprime*zprime)

            if (R > 1.5d0) then
                density(i) = 0.d0
            else
                Z_c = (xprime*self%sinOmega -
    yprime*self%cosOmega)*self%sinIncl &
                    + zprime*self%cosIncl

                density(i) = self%nsr * exp(-(R-self%Rsr)**2 *
    self%sigmaRsr2Inv &
                        - abs(Z_c)*self%sigmaZsrInv)
            end if
        end do
    end subroutine getDensityRing

    subroutine initializeFeature(self)
        implicit none
        class(Feature) :: self

        self%thetatfR = self%thetatf * deg2rad
        self%sigmaRtfInv = 1.d0 / self%sigmaRtf
        self%sigmaZtfInv = 1.d0 / self%sigmaZtf
        self%sigmaThetatfRinv = 1.d0  /(self%sigmaThetatf * deg2rad)
        self%sinOmega = sin(self%Omega * deg2rad)
        self%cosOmega = cos(self%Omega * deg2rad)
        self%sinIncl = sin(self%Incl * deg2rad)
        self%cosIncl = cos(self%Incl * deg2rad)
    end subroutine initializeFeature

    subroutine getDensityFeature(self, x, y, z, density, lon)
        implicit none

        class(Feature) :: self
        real(dp), dimension(:), intent(in)  :: x, y, z
        real(dp), dimension(:), intent(out) :: density
        real(dp), intent(in), optional      :: lon

        integer(i4b) :: i
        real(dp) :: xprime, yprime, zprime
        real(dp) :: R, Z_c
        real(dp) :: theta
```

```

        do i = 1, n_LOS
            xprime = x(i) - self%x0
            yprime = y(i) - self%y0
            zprime = z(i) - self%z0
            R = sqrt(xprime*xprime + yprime*yprime + zprime*zprime)

            if (R > 1.5d0) then
                density(i) = 0.d0
            else
                theta = atan2(y(i), x(i)) - (lon + self%thetatfR)
                ! theta = atan2(y(i), x(i)) - (lon + self%thetatfR)

                ! Constraining the angle to the limit [-pi, pi]
                do while (theta < -pi)
                    theta = theta + 2*pi
                end do
                do while (theta > pi)
                    theta = theta - 2*pi
                end do

                Z_c = (xprime*self%sinOmega -
    yprime*self%cosOmega)*self%sinIncl &
                    + zprime*self%cosIncl

                density(i) = self%ntf * exp(-((R-self%Rtf)*self%sigmaRtfInv)**2
    &
                        - abs(Z_c)*self%sigmaZtfInv &
                        - (theta*self%sigmaThetatfRinv)**2)
            end if
        end do
    end subroutine getDensityFeature

    ! ========================================================================
    !                   Linked list routines (ZodiComponent)
    ! ========================================================================
    function next(self)
        ! Routine which selects the next link in the linked list
        class(ZodiComponent) :: self
        class(ZodiComponent), pointer :: next
        next => self%nextLink
    end function next

    subroutine add(self,link)
        ! Routine which add a new object and link to the linked list
        class(ZodiComponent), target  :: self
        class(ZodiComponent), pointer :: link
        class(ZodiComponent), pointer :: comp

        comp => self
        do while (associated(comp%nextLink))
            comp => comp%nextLink
        end do
        link%prevLink => comp
        comp%nextLink    => link
    end subroutine add

    subroutine add2Complist(comp)
        implicit none
        class(ZodiComponent), pointer :: comp

        if (.not. associated(comp_list)) then
```

Listing A.1: The fortran implementaion of the Zodiacal Emission module in `Commander`

Bibliography

[1] I. Newton. *The Principia : mathematical principles of natural philosophy.* 1999.

[2] G. Galilei. *Sidereus nuncius.* 1987.

[3] D. Wands. *Edwin Powell Hubble, Biography.* 1997. URL: `http://www-groups.dcs.st-and.ac.uk/~history/Biographies/Hubble.html` (visited on 01/10/2019).

[4] E. Hubble. 'A Relation between Distance and Radial Velocity among xtra-Galactic Nebulae'. In: *Proceedings of the National Academy of Science* 15.3 (Mar. 1929), pp. 168–173. DOI: `10.1073/pnas.15.3.168`.

[5] A. Einstein. 'Die Grundlage der allgemeinen Relativitätstheorie'. In: *Annalen der Physik* 354.7 (Jan. 1916), pp. 769–822. DOI: `10.1002/andp.19163540702`.

[6] A. Friedmann. 'On the curvature of space'. In: (1922). URL: `http://www.lorentz.leidenuniv.nl/Friedmann/` (visited on 22/05/2020).

[7] S. Singh. *Even Einstein Had His Off Days.* 2005. URL: `https://www.nytimes.com/2005/01/02/opinion/even-einstein-had-his-off-days.html` (visited on 25/03/2020).

[8] H. Bondi and T. Gold. 'The Steady-State Theory of the Expanding Universe'. In: *mnras* 108 (Jan. 1948), p. 252. DOI: `10.1093/mnras/108.3.252`.

[9] R. A. Alpher and R. C. Herman. 'Remarks on the Evolution of the Expanding Universe'. In: *Physical Review* 75.7 (Apr. 1949), pp. 1089–1095. DOI: `10.1103/PhysRev.75.1089`.

[10] R. H. Dicke et al. 'Cosmic Black-Body Radiation.' In: *The Astrophysical Journal* 142.142 (1965), p. 414. ISSN: 0004-637X. DOI: `10.1086/148306`.

[11] M. V. Gorenstein, G. F. Smoot and R. A. Muller. 'Anisotropy of the cosmic microwave background radiation.' In: 9 (June 1977), p. 431.

[12] P. J. E. Peebles and J. T. Yu. 'Primeval Adiabatic Perturbation in an Expanding Universe'. In: *apj* 162 (Dec. 1970), p. 815. DOI: `10.1086/150713`.

[13] R. A. Sunyaev. 'Fluctuations of the Microwave Background Radiation'. In: *Large Scale Structures in the Universe.* Ed. by M. S. Longair and J. Einasto. Vol. 79. IAU Symposium. Jan. 1978, p. 393.

[14] E. L. Wright et al. 'Angular Power Spectrum of the Cosmic Microwave Background Anisotropy seen by the COBE DMR'. In: 464 (June 1996), p. L21. DOI: `10.1086/310073`.

[15] D. J. Fixsen et al. 'The Cosmic Microwave Background Spectrum from the Full COBE FIRAS Data Set'. In: 473 (Dec. 1996), p. 576. DOI: `10.1086/178173`.

[16] G. Hinshaw et al. 'Nine-year Wilkinson Microwave Anisotropy Probe (WMAP) Observations: Cosmological Parameter Results'. In: 208.2 (Oct. 2013), p. 19. DOI: `10.1088/0067-0049/208/2/19`.

[17] NASA/JPL-Caltech/ESA. *Comparison of CMB results from COBE, WMAP and Planck.* 23rd Mar. 2013. URL: `https://photojournal.jpl.nasa.gov/jpeg/PIA16874.jpg` (visited on 25/11/2019).

[18] Planck Collaboration et al. 'Planck 2015 results. XIII. Cosmological parameters'. In: *aap* 594, A13 (Sept. 2016), A13. DOI: `10.1051/0004-6361/201525830`. arXiv: `1502.01589 [astro-ph.CO]`.

[19] BICEP2 Collaboration et al. 'Detection of B-Mode Polarization at Degree Angular Scales by BICEP2'. In: *prl* 112.24, 241101 (June 2014), p. 241101. DOI: `10.1103/PhysRevLett.112.241101`. arXiv: `1403.3985 [astro-ph.CO]`.

[20] D. Baumann et al. 'Probing Inflation with CMB Polarization'. In: *American Institute of Physics Conference Series.* Ed. by S. Dodelson et al. Vol. 1141. American Institute of Physics Conference Series. June 2009, pp. 10–120. DOI: `10.1063/1.3160885`. arXiv: `0811.3919 [astro-ph]`.

[21] M. Hazumi et al. 'LiteBIRD: A Satellite for the Studies of B-Mode Polarization and Inflation from Cosmic Background Radiation Detection'. In: *Journal of Low Temperature Physics* 194.5 (2019), pp. 443–452. ISSN: 1573-7357. DOI: `10.1007/s10909-019-02150-5`. URL: `https://doi.org/10.1007/s10909-019-02150-5`.

[22] K. Abazajian et al. 'CMB-S4 Science Case, Reference Design, and Project Plan'. In: *arXiv e-prints*, arXiv:1907.04473 (July 2019), arXiv:1907.04473. arXiv: `1907.04473 [astro-ph.IM]`.

[23] BeyondPlanck Collaboration. 'Global Bayesian analysis of the Planck Low Frequency Instrument data (A&A, in preparation 2020'. In: ().

[24] B. May. *A Survey of Radial Velocities in the Zodiacal Dust Cloud.* Jan. 2008. DOI: `10.1007/978-0-387-77706-1`.

[25] Y. Beletsky. *Zodiacal light over La Silla.* 3rd Nov. 2014. URL: `https://www.eso.org/public/images/zodiacal_beletsky_potw/` (visited on 07/11/2019).

[26] A. K. Bartlett. 'The zodiacal light'. In: *Popular Astronomy* 10 (Apr. 1902), pp. 179–184.

[27] G. D. Cassini. *Découverte de la lumière celeste qui paroist dans le zodiaque.* 1685. DOI: `10.3931/e-rara-7552`.

[28] M. Hauser et al. 'IRAS observations of the diffuse infrared background'. In: *The Astrophysical Journal* 278 (Mar. 1984). DOI: `10.1086/184212`.

[29] F. J. Low et al. 'Infrared cirrus: new components of the extended infrared emission.' In: 278 (Mar. 1984), pp. L19–L22. DOI: `10.1086/184213`.

[30] S. Dermott et al. 'IRAS observations show that the Earth is embedded in a solar ring of asteroidal dust particles in resonant lock with the planet'. In: (Mar. 1994).

[31] T. Gold. 'Resonant orbits of grains and the formation of satellites'. In: *Icarus* 25 (Mar. 1975), pp. 489–491. DOI: `10.1016/0019-1035(75)90016-0`.

[32] W. T. Reach et al. 'Observational confirmation of a circumsolar dust ring by the COBE satellite'. In: *Nature* 374.6522 (Mar. 1995), pp. 521–523. ISSN: 00280836. DOI: `10.1038/374521a0`.

[33] W. T. Reach et al. 'The mid-infrared spectrum of the zodiacal and exozodiacal light'. In: 164.2 (Aug. 2003), pp. 384–403. DOI: `10.1016/S0019-1035(03)00133-7`.

[34] R. H. Giese. 'Light Scattering by Small Particles and Models of Interplanetary Matter Derived from the Zodiacal Light'. In: (1963).

[35] ESA. *Planck, all-sky images.* 2019. URL: `http://planck.cf.ac.uk/all-sky-images` (visited on 01/10/2019).

[36] T. L. Svalheim. *Spectrum.* 2019. URL: `https://github.com/trygvels/spectrum/blob/master/spectrum.py` (visited on 26/05/2020).

[37] P. Collaboration et al. *Planck 2018 results. IV. Diffuse component separation.* 2018. arXiv: `1807.06208 [astro-ph.CO]`.

[38] A. Kogut. 'Synchrotron Spectral Curvature from 22 MHz to 23 GHz'. In: 753.2 (July 2012), p. 110. DOI: `10.1088/0004-637X/753/2/110`.

[39] Planck Collaboration et al. 'Planck 2015 results. X. Diffuse component separation: Foreground maps'. In: *aap* 594, A10 (Sept. 2016), A10. DOI: `10.1051/0004-6361/201525967`. arXiv: `1502.01588 [astro-ph.CO]`.

[40] E. M. Leitch et al. 'An Anomalous Component of Galactic Emission'. In: *apjl* 486.1 (Sept. 1997), pp. L23–L26. DOI: `10.1086/310823`. arXiv: `astro-ph/9705241 [astro-ph]`.

[41] B. T. Draine and A. Lazarian. *Diffuse Galactic Emission from Spinning Dust Grains.* Tech. rep.

[42] Planck Collaboration et al. 'Planck early results. XX. New light on anomalous microwave emission from spinning dust grains'. In: (Jan. 2011). DOI: `10.1051/0004-6361/201116470`. URL: `http://arxiv.org/abs/1101.2031%20http://dx.doi.org/10.1051/0004-6361/201116470`.

[43] C. L. Bennett et al. 'Nine-year Wilkinson Microwave Anisotropy Probe (WMAP) Observations: Final Maps and Results'. In: *apjs* 208.2, 20 (Oct. 2013), p. 20. DOI: `10.1088/0067-0049/208/2/20`. arXiv: `1212.5225 [astro-ph.CO]`.

[44] T. Kelsall et al. ' The COBE Diffuse Infrared Background Experiment Search for the Cosmic Infrared Background. II. Model of the Interplanetary Dust Cloud '. In: *The Astrophysical Journal* (1998). ISSN: 0004-637X. DOI: `10.1086/306380`.

[45] Planck Collaboration et al. 'Planck 2013 results. XIV. Zodiacal emission'. In: *aap* 571, A14 (Nov. 2014), A14. DOI: `10.1051/0004-6361/201321562`. arXiv: `1303.5074 [astro-ph.CO]`.

[46] K. M. Górski et al. 'HEALPix: A Framework for High-Resolution Discretization and Fast Analysis of Data Distributed on the Sphere'. In: 622.2 (Apr. 2005), pp. 759–771. DOI: `10.1086/427976`.

[47] H. K. Eriksen et al. 'Joint Bayesian Component Separation and CMB Power Spectrum Estimation'. In: 676.1 (Mar. 2008), pp. 10–32. DOI: `10.1086/525277`.

[48] D. S. Seljebotn et al. 'A Multi-level Solver for Gaussian Constrained Cosmic Microwave Background Realizations'. In: 210.2 (Feb. 2014), p. 24. DOI: `10.1088/0067-0049/210/2/24`.

[49] H. K. Eriksen. *Commander*. 2020. URL: `https://github.com/hke/Commander` (visited on 10/02/2020).

[50] S. Geman and D. Geman. 'Stochastic Relaxation, Gibbs Distributions, and the Bayesian Restoration of Images'. In: *IEEE Transactions on Pattern Analysis and Machine Intelligence* PAMI-6.6 (1984), pp. 721–741.

[51] P. R. Bevington. *Data reduction and error analysis for the physical sciences*. 1969.

[52] K. Ganga. *COBEZodiModelTemplates*. 2013. URL: `https://wiki.cosmos.esa.int/planckpla/index.php/COBEZodiModelTemplates` (visited on 21/05/2020).

[53] Planck Collaboration et al. 'Planck 2015 results. VIII. High Frequency Instrument data processing: Calibration and maps'. In: *aap* 594, A8 (Sept. 2016), A8. DOI: `10.1051/0004-6361/201525820`. arXiv: `1502.01587 [astro-ph.CO]`.

[54] N. JPL. *HORIZONS Web-Interface*. URL: `https://ssd.jpl.nasa.gov/horizons.cgi` (visited on 06/06/2020).

[55] K. Kordylewski. 'Photographische Untersuchungen des Librationspunktes L_5 im System Erde-Mond'. In: *actaa* 11 (Jan. 1961), p. 165.

[56] J. Slíz-Balogh, A. Barta and G. Horváth. 'Celestial mechanics and polarization optics of the Kordylewski dust cloud in the Earth-Moon Lagrange point L5 - I. Three-dimensional celestial mechanical modelling of dust cloud formation'. In: *mnras* 480.4 (Nov. 2018), pp. 5550–5559. DOI: `10.1093/mnras/sty2049`. arXiv: `1910.07466 [astro-ph.EP]`.

[57] N. JPL. *NASA's WISE Finds Earth's First Trojan Asteroid*. URL: `https://www.jpl.nasa.gov/news/news.php?feature=3080` (visited on 10/06/2020).